LIETUVOS ENERGETIKOS INSTITUTAS

Vilnius University Institute of Theoretical Physics and Astronomy

Annual Report of the Association EURATOM / LEI

2011

ISSN 2029-1612 (print)

ISSN 2351-6976 (online)

© Lithuanian Energy Institute, 2012

Content

Executive summary 5

General information 7

1 Assessment of Plasma Vessel venting system capacity 8

1.1 Description of W7-X Plasma Vessel venting system 8
1.2 Description of the model for COCOSYS 8
1.3 Results of analysis 10
1.3.1 The base case scenario 11
1.3.2 Comparison with RELAP5 results 13
1.3.3 Failure of opening of burst disk at 1.1 bar 16
1.3.4 Temperature of outside environment 0 °C 17
1.3.5 Influence of pressure losses inside venting system pipes 18

1.4 Conclusions 21

2 Limit Analysis of the Port Welds between the Plasma Vessel and the Ports in the W7-X Cryostat System 22

2.1 Geometrical and finite element models of the ports welds 22
2.2 Elements used for models 22
2.3 Material properties 24
2.4 Allowable stresses 24
2.5 Boundary conditions 25
2.6 Loading for analysis load case 5, SF1.0 26
2.7 Results of analyses 27
2.7.1 Results of stress analysis 27
2.7.2 Results of limit analysis 34

2.8 Conclusions of structural integrity analysis 43

3 W7-X probabilistic risk analysis 44

3.1 Estimation of Divertor cooling circuit ACK10 availability 44
3.1.1 Fault Tree analysis 45
3.1.2 Failure Modes and Effects Analysis (FMEA) 51
3.1.3 Development of unavailability models 51
3.1.4 Model calculation 53
3.1.5 Conclusions on ACK10 availability 56

3.2 Evaluation of ACK10 availability increase measures 56
3.2.1 Evaluation method 56
3.2.2 Evaluation of possible alternatives 56
3.2.3 Summary on ACK10 availability increase measures 62

4 Theoretical studies of the spectroscopic characteristics of highly charged tungsten atoms having open d and f-shells accounting for relativistic and correlation effects 63

4.1 Developing of methods and packaging for including the QED effects in the quasi-relativistic energy spectra calculations 63
4.2 Investigation of the configuration interaction regularities in the ground and excited configurations of tungsten ions using the average characteristics of CI 64
4.3 Theoretical studies of electronic transitions of higher multipolarities in tungsten ions having open f-shell 66
4.3.1 Large scale calculations 67
4.3.2 Error estimates and conclusions 69
4.4 References 70

5 Mobility program 2011 71

6 Other activities in magnetic confinement fusion 72

7 Public information 73

8 Publications 74

9 Implementation of QA system 75

EXECUTIVE SUMMARY

Lithuanian Energy Institute (LEI) signed a contract on joining the European Fusion Development Agreement (EFDA), and starting from the 1st of January, 2007, Lithuania officially became an EFDA member. In 2011 EURATOM/LEI association successfully continued activities in research related to European Fusion Development Agreement activities. Our activities concentrate around two issues: 1) Fusion safety issues and 2) Plasma diagnostics.

The largest part of our activities is related to Wendelstein 7-X programme implemented by Max-Planck-Institut für Plasmaphysik (IPP) in Germany. In 2011 our association performed an assessment of the W7-X Plasma Vessel venting system capacity, a structural integrity analysis of the port welds, and an assessment of Divertor cooling circuit availability as a part of probabilistic risk analysis.

Assessment of W7-X Plasma Vessel venting system capacity was performed using computer codes RELAP5 and COCOSYS. RELAP5 was used to determine the mass and energy flow rates through the ruptured pipe and gas flows through the venting system. A detailed thermal-hydraulic model was developed to represent the complicated cooling system of W7-X. COCOSYS code was used for a detailed analysis of Plasma Vessel venting system. Different scenarios were investigated to estimate the acceptance of the design of the venting system. When the results of RELAP5 and COCOSYS calculations were compared, a significant difference in timing of safety valve opening was observed and an investigation was performed to identify the reasons for such difference. The performed analysis showed that the current design of Plasma Vessel venting system ensures pressures below design limits.

The port welds between the Plasma Vessel and the ports in W7-X cryostat system were investigated. The structural integrity analysis of the welding connections was performed for the following ports / port combinations:

- Welding connection between the port AEQ20 and the PV shell with a 1 mm gap.
- Welding connection between the port AEU30 and the PV shell with a 1 mm and 6 mm gap.
- Welding connection between the port AEK20 and the PV shell with a 1 mm gap.

These ports were modelled using the FEM technique as 3D bodies together with the regions of the PV shell around the ports and the welding seam. The main objective of the analysis was to calculate the load scaling factors for all considered ports. For the geometrical modelling, CAD program SolidWorks was applied. Structural analysis of the ports was performed using ABAQUS code.

According to stress analysis results, it was received that the stresses in port and vessel are below the yield strength. The stresses in welded zone of port and PV in nodes of some elements exceed the yield strength, but the mean value of stresses is below the yield strength. The influence of these elements to stress condition of the entire structure is minor. According to limit analysis results, the fact that displacement of the point where loads are applied starts to increase very rapidly was not detected. The limit analysis showed positive results of the welding between Plasma Vessel and ports, which means that the stability of the welding between Plasma Vessel and considered ports will be sustained at used loading for the analysis.

For the first time, the W7-X probabilistic risk analysis was performed to estimate the Divertor cooling circuit ACK10 availability and recommend measures to increase availability of this circuit. RiskSpectrum ® PSA Professional developed by Relcon Scandpower AB (Sweden) was used. The

performed analysis showed that unavailability of the ACK10 is 18.8 % of the operational campaign. The main impact to unavailability comes from the operation regime of the cooling pumps, which leads to high cyclic load and high failure probability to the secondary pump and its regulating valve. These components bring correspondingly 51 % and 35 % to the total unavailability. Four options for increasing ACK10 availability were analysed, and it was determined that changing pumps operation mode does not increase overall reliability of the system. Installation of the 3rd redundant pump and keeping a set of necessary spare parts are similar from the risk decrease perspective but from the cost effectiveness point of view, keeping spare parts could be a preferable option. Preventive maintenance of the pumps gives the least decrease of risk from the considered options.

Tungsten as a heat-resistant material is planned to be used at ITER. Using tungsten in some parts of the tokamak may solve the tritium retention problem. On the other hand, tungsten atoms can detach from the inner walls of the fusion reactor, penetrate into the plasma and be ionised to very high degrees. Various tungsten ions will irradiate strongly thus cooling the plasma. Our association performed theoretical studies of the spectroscopic characteristics of highly charged tungsten atoms having open d and f-shells accounting for relativistic and correlation effects. These results could contribute to the development of plasma diagnostic techniques in the future.

In 2011 the expenditure of the association EURATOM/LEI eligible for baseline support was 215,900 EUR, of which 36,361 EUR funded by EURATOM, and 10,565 EUR of fund for mobility actions. The major part of financing comes from Lithuanian budget support. The total research volume of the 2011 activities was ~7 professional man-years.

Details on all the performed activities are given in further sections of this report.

GENERAL INFORMATION

EURATOM/LEI Steering Committee

Mr. Ruggero Giannella, Scientific Officer RTD - K6 (Fusion Association Agreements)

Mr. Vito Marchese, Scientific Officer RTD - K6 (Fusion Association Agreements)

Mr. Marc Cosyns, Administrator RTD - K7 (Administration and Finances)

Mr. Zenonas Rokas Rudzikas, Vilnius University Institute of Theoretical Physics and Astronomy

Mr. Liudvikas Pranevičius, Vytautas Magnus University

Mr. Stanislovas Žurauskas, Ministry of Education and Science

EURATOM/LEI Head of Research Unit

Eugenijus Ušpuras
Lithuanian Energy Institute
Breslaujos g. 3, LT-44403 Kaunas, Lithuania
Phone: +370 37 401926
Fax: +370 37 351271
e-mail: uspuras@mail.lei.lt

Research Unit in Lithuania

Lithuanian Energy Institute

Breslaujos g. 3, LT-44403 Kaunas, Lithuania
Phone: +370 37 401801
Fax: +370 37 351271
e-mail: rastine@mail.lei.lt
URL: http://www.lei.lt

Vilnius University Institute of Theoretical Physics and Astronomy

A. Goštauto g. 12, LT-01108 Vilnius, Lithuania
Phone: +370 5 2193251
Fax: +370 5 2125361
e-mail: tfai@tfai.vu.lt
URL: http://www.tfai.vu.lt/

1 ASSESSMENT OF PLASMA VESSEL VENTING SYSTEM CAPACITY

To protect the Plasma Vessel from overpressure in case of loss of coolant accident the venting system is installed, which consists of two burst disks and associated piping to direct the released steam from Plasma Vessel to environment. The analysis was performed to investigate whether the piping and condensation of steam does not impose additional resistance, which could potentially lead to higher pressure in Plasma Vessel. For the analysis a 40 mm diameter pipe rupture inside the Plasma Vessel during "baking" mode was assumed.The report includes short description of the venting system, description of the developed model for COCOSYS code and results of the performed calculations. The COCOSYS code results are also compared to the results received using RELAP5 code, which was also used to calculate the water discharge from the ruptured pipe of the Plasma Vessel cooling circuit. At the end of the report, conclusions of the performed analysis are formulated.

1.1. Description of W7-X Plasma Vessel venting system

The layout of piping of W7-X Plasma Vessel venting system is shown in Figure 1.1. To protect the Plasma Vessel from overpressure two burst disks are installed: 1) one with the opening pressure of 1.1 bar and 2) one with the opening pressure of 1.2 bar. Diameter of both burst disks is 250 mm. Both burst disks are installed on the pipelines of 300 mm inner diameter that are connected to the main pipeline of 500 mm inner diameter. The exit of the main pipeline is outside the building above the roof level.

In case of a loss of coolant accident inside the plasma vessel, the opening pressure of the burst disk would be reached and after the disk opening, the steam would enter the piping of the venting system and would be directed outside the building. The steam would be condensing on the colder surfaces of the piping; therefore, the piping is designed with inclination, which ensures that water flows to the drainage outlet.

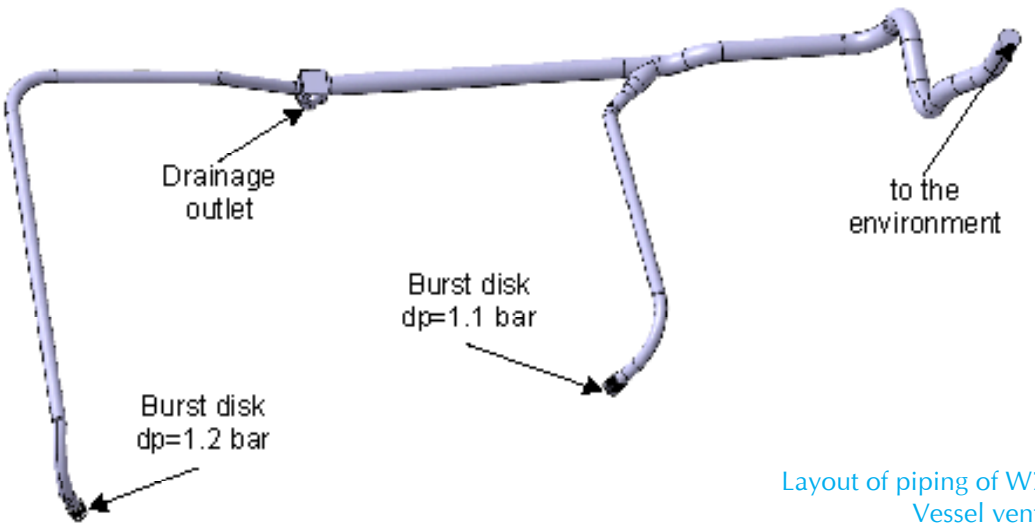

Figure 1.1
Layout of piping of W7-X Plasma Vessel venting system

1.2 Description of the model for COCOSYS

The nodalisation scheme of W7-X Plasma Vessel venting system is presented in Figure 1.2. The volume of each node and the associated areas of the structures connected to the nodes are presented as well. The red lines show junctions between the nodes for atmospheric flow, and the blue arrows indicate the flow of water, which appears due to steam condensation. Node LEIT1 represents the shorter line with the burst disk of 1.1 bar opening pressure. Node LEIT2 represents the longer line with the burst disk of the opening pressure of 1.2 bar. Also, this node includes a part of the main line with the drainage outlet. Both node LEIT1 and LEIT2 are connected to node GABEL, which represents the "fork" of the connected pipes. The rest part of the main pipeline inside the building is represented by the node HAUPT. In the model it is assumed that a certain part of the pipe would be located outside the building, and this part is represented by node CHIMNEY. The volume of the nodes was calculated from the drawings provided by W7-X team.

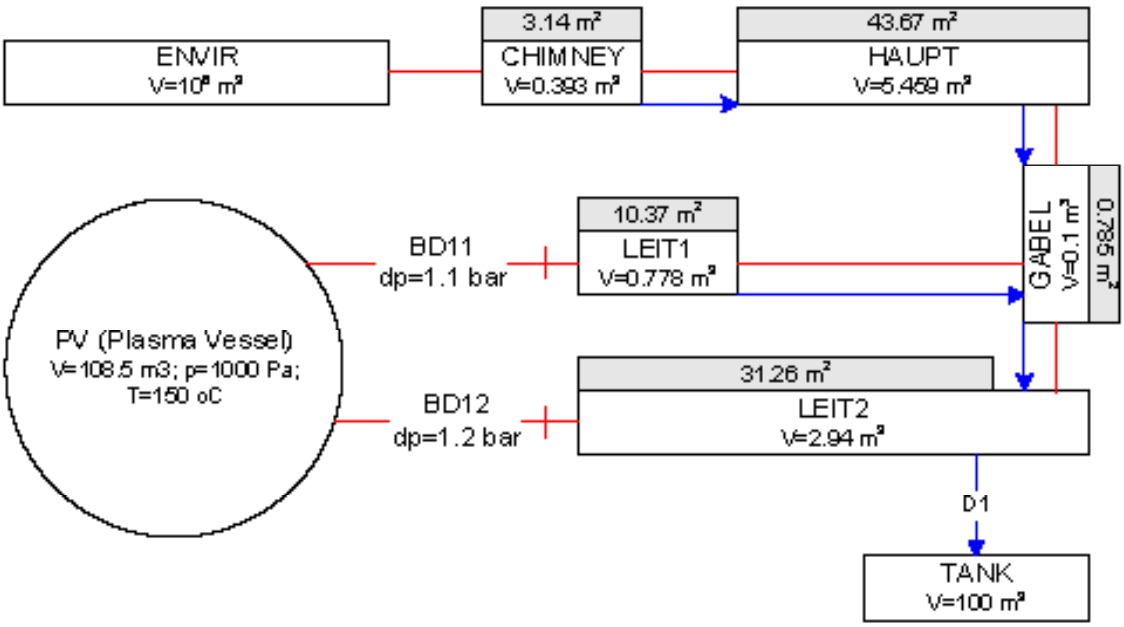

Figure 1.2
Nodalisation scheme of W7-X venting system for COCOSYS

The gas temperature inside the building was assumed 20 °C with the relative humidity of 60 %. The same temperature and humidity was assumed inside the piping of the venting system. The initial temperature (before the accident) inside the plasma vessel is 150 °C.

In COCOSYS code the atmospheric and water flows are simulated separately, therefore, separate junctions have to be defined. The rupture disks are simulated by a special junction type, which considers that after reaching a defined set point, the junction opens and stays open until the end of the analysis. The other atmospheric junctions are always open. The associated flow loss coefficients were estimated taking into account friction loss and local pressure losses due to changing flow

direction and diameter. In the model it is assumed that the water starts flowing from one node to another when the water film thickness on the inner surface of the pipe reaches 1 mm.

The piping is made of 1 mm thick stainless steel. The heat transfer area of the piping was calculated from the drawings provided by W7-X team. It is assumed that heat exchange on both surfaces could occur due to convection, condensation and wall to gas radiation.

The outer surface of structure associated with this node faces the outside environment, which could have temperature different from the temperature inside the building. For the base case analysis it was assumed that the temperature in the outside environment is also 20 °C.

The structures of the plasma vessel were assumed to be hot with temperature of 150 °C. Such temperature is constant during the entire calculation time. Since COCOSYS code cannot simulate deep vacuum conditions, it is assumed that the initial pressure inside plasma vessel is 1000 Pa, which is the lowest possible pressure allowed in the code.

The analysis of the venting system was performed for the loss of coolant accident scenario, which assumes 40 mm diameter pipe rupture in the operation mode "Baking". During this operation mode, the inner surfaces in the plasma vessel are cleaned from impurities and plasma vessel is prepared for plasma ignition. The coolant release rate and the specific enthalpy of the released coolant were calculated using RELAP5 code and are shown in Figure 1.3. After pipe rupture the maximal flow rate through the break into the plasma vessel reaches ~28 kg/s, but after this peak it gradually decreases. This decrease is related to closure of the automatic valves in the baking circuit. After 25 s the release rate to the plasma vessel is ~5 kg/s, and after 80 s it is < 2 kg/s. The specific enthalpy of the released coolant changes with the time – at first only water is released, but after ~75 s the superheated steam appears.

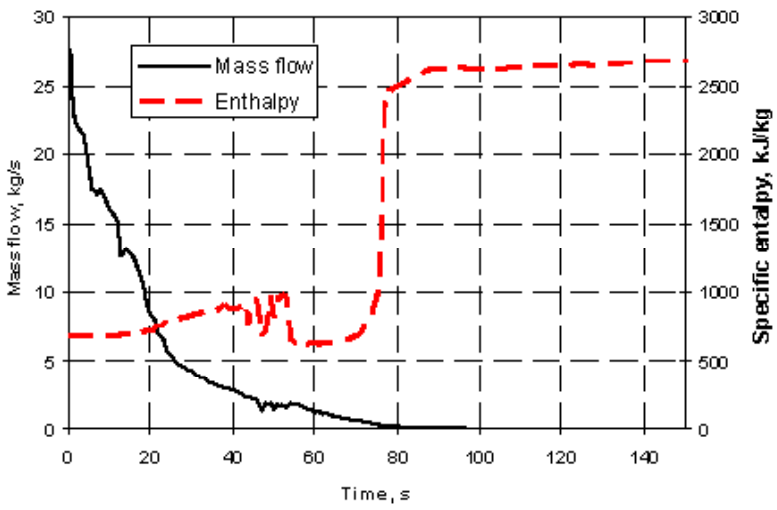

Figure 1.3
Coolant release rate and specific enthalpy to plasma vessel received from RELAP5 code analysis

1.3 Results of analysis

To investigate the piping of venting system in case of LOCA during "baking" mode, the following variants were investigated:

1. The base case scenario when the entire system operates as expected;
2. Base case comparison with RELAP5 results;
3. Failure of burst disk opening at 1.1 bar;

4. Temperature of outside environment 0 °C;
5. Influence of coolant release rate;
6. Influence of pressure losses inside venting system pipes.

Further, all of these investigated variants will be described in detail.

1.3.1 The base case scenario

This section presents the results of the base case scenario, which assumes normal operation of all the systems and equipment. Figure 1.4 presents how the pressure in the nodes changes during the accident. After the pipe rupture, the pressure in PV starts increasing and in 25 s reaches 1.1 bar, which is a set-point for the 1st burst disk opening. After burst disk opening, the steam is discharged to the piping of the venting system, and the pressure in PV starts decreasing. Nevertheless, the pressure in PV stays slightly above atmospheric due to vaporization of the water in PV, which appears due to contact between the water and hot structures. The maximal pressure peak is ~1.11 bar, which means that the diameter of the installed burst disk is sufficient to prevent further pressure increase.

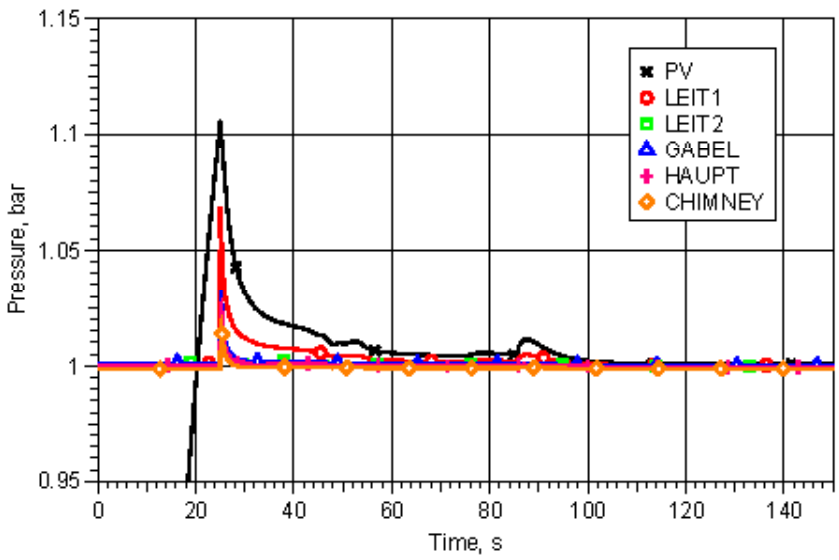

Figure 1.4
Base case scenario:
Pressure in the nodes

Small pressure peak after ~85 s appears due to increased enthalpy of the released coolant (see Figure 1.3), but since the coolant release rate further decreases, the peak is small and short-term. The influence of coolant enthalpy increase is clearly seen in Figure 1.5, which shows the gas temperature in the nodes. After the pipe rupture, the gas temperature in plasma vessel drops down to temperature, which corresponds to saturated steam conditions. The temperature in the piping stays constant until the burst disk opens. After that the temperature increases in the affected flow path. But the gas temperature in node LEIT2 does not change since the second burst disk remains intact and no steam enters this part of the venting system.

Figure 1.6 shows the water mass inside the plasma vessel. After the pipe rupture, the water is released to plasma vessel, and due to pressure drop partially evaporates. The generated steam contributes to pressure increase in plasma vessel. The water is collected in the lower part of the vessel, but due to contact with hot PV surfaces evaporates as well. The process of vaporization is clearly seen in this figure when after ~70 s the water mass in PV starts decreasing.

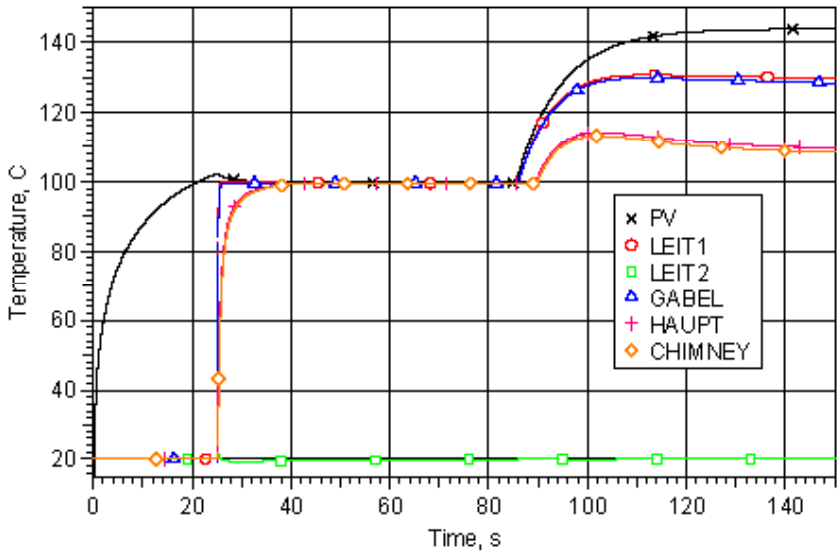

Figure 1.5
Base case scenario: Gas temperature in the nodes

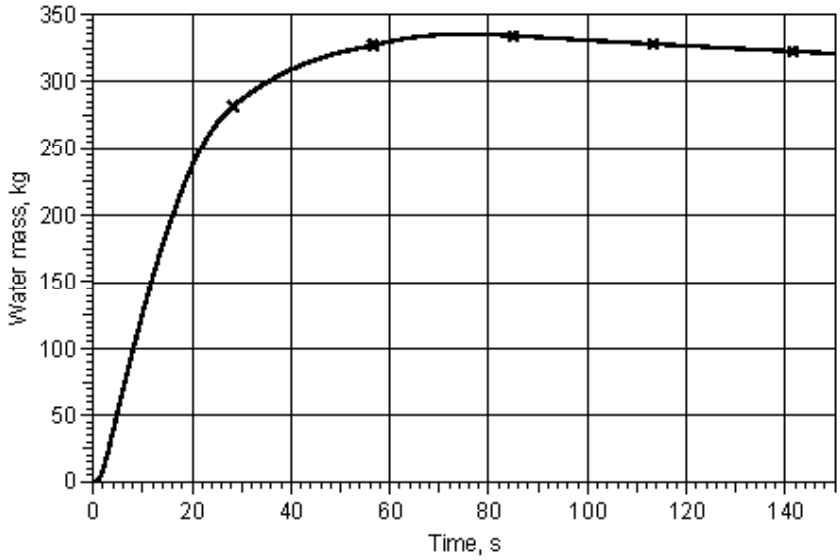

Figure 1.6
Base case scenario: Water mass in the plasma vessel

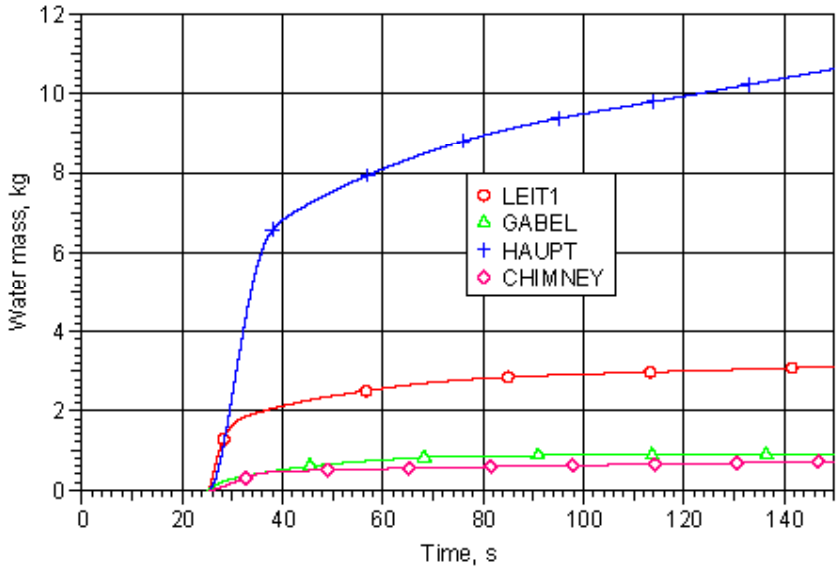

Figure 1.7
Base case scenario: Water mass in the nodes

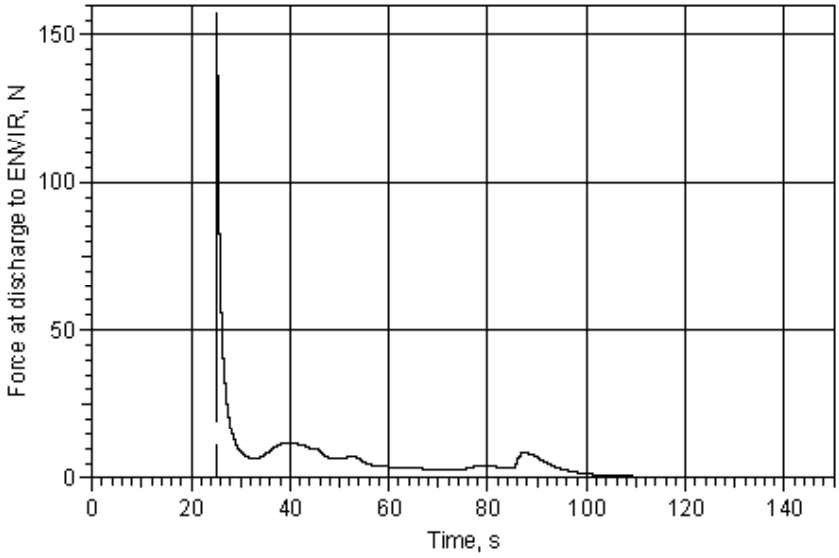

Figure 1.8
Base case scenario: Force acting at the exit from venting system to the environment

Figure 1.7 shows water where most of the steam condenses inside the piping. The largest water mass is observed in node HAUPT, which represents the main pipeline of 500 mm diameter, thus the largest heat transfer area. The other largest part of the condensed steam is located in node LEIT1, but no water is observed in LEIT2. This result shows that the thickness of the water film on the inner surface of pipes is <1 mm, and there is no overflow from one node to another.

To investigate what forces are expected at the exit from the venting system to the environment, some additional calculations are required. The force acting on the exit of the exhaust pipe could be expressed by $F = \dot{m}^2/(\rho \cdot A)$ (N), where $\dot{m}$ is the mass flow through the junction (kg/s), ρ is the gas density in CHIMNEY (kg/m^3) and *A* is the area of the junction (d = 500 mm) (m$^{2)}$. The results of the performed calculations using this formula are presented in Figure 1.8. The maximal force is observed right after the burst disk opening and it reaches ~155 N and immediately decreases down to negligible level.

1.3.2 Comparison with RELAP5 results

Analogous calculations are performed using RELAP5 code, which is a thermal-hydraulic code developed for heat and mass transport analysis in the piping systems. This code was used to calculate the coolant release to Plasma Vessel, and further, its model was enhanced to simulate the processes in Plasma Vessel and piping of the venting system. RELAP5 solves mass and energy balance equations for each phase (water and gas including steam) separately, i.e. water and steam could have different temperatures and thermal equilibrium between phases is not required.

One of the main assumptions in the lumped-parameter code COCOSYS is that the water cannot exist in the superheated gas phase. If the water is injected to superheated gas, then its temperature is set equal to saturation temperature at the actual total pressure. The excess energy is used to evaporate water until saturated steam conditions are reached in the gas phase. If the FLUID zone part is not created at that time, then the water remains in the atmosphere as fog and it is in thermal equilibrium with the gas. If the FLUID part is created, then the water droplets are deposited to this part of the node, i.e. to the sump. Thermal equilibrium between GAS and FLUID parts is not required. In COCOSYS code there are several options to define the coolant injection to the node: 1) injection to the gas phase and 2) injection to FLUID part. In case of injection to FLUID part, the injected energy at first is consumed to heat up the sump, and then the heat exchange between gas and water occurs via the water surface. The heat exchange with structures associated with GAS and FLUID zone parts is also taken into account.

Figure 1.9 presents comparison between RELAP5 and COCOSYS results using both injection options. Assuming injection to gas phase after pipe rupture the pressure in PV starts increasing and in 25 s reaches 1.1 bar, which is a set-point for the 1st burst disk opening. If the injection is assumed to occur to FLUID part, then pressure in PV reaches 1.1 bar in 34 s, and this result is close to RELAP5 results showing 32 s to burst disk opening. The reason for such difference is that the water through the ruptured pipe is assumed to be released to gas phase of PV, which is assumed to be at the initial pressure of 1000 Pa, i.e. at such pressure the saturation temperature is close to 0 °C. According to assumption in COCOSYS code, the water temperature is set to saturation temperature at given pressure, and the excess water is evaporated to reach saturated conditions in the gas phase. The water, which is not evaporated, is assumed to be homogeneously distributed in the gas phase. If the water is assumed to be injected to the FLUID part, then the evaporation of water occurs only due to heat exchange between water and gas via the water surface, i.e. much slower process than "flash" evaporation.

Figure 1.10 presents comparison of calculated steam flow through the ruptured burst disk. The largest steam flow is calculated with COCOSYS assuming injection to occur to the gas phase. The mass flow calculated with RELAP5 code is smallest (peak is ~2 kg/s) from three calculated variants and it shows more oscillations right after rupture of the burst disk.

Figure 1.11 presents comparison of calculated water mass in Plasma Vessel using RELAP5 and COCOSYS codes. RELAP5 results are in agreement with COCOSYS results assuming injection to FLUID part, and both of these calculations show more water accumulated in PV compared to the case with water injection to the GAS part of the node. This result clearly shows that the assumption of water injection option influences the received results significantly. The difference between RELAP5 and COCOSYS results assuming injection to GAS is ~50 kg of water in PV.

Figure 1.12 presents comparison of calculated force at discharge point from the venting system to the environment. The largest peak of force occurs in COCOSYS calculations assuming water injection to Plasma Vessel FLUID zone part, but it appears after 34 s, the second largest is from COCOSYS calculations assuming water injection to Plasma Vessel GAS zone part. The difference of calculated force at discharge point from the venting system between these variants is ~20 N. The smallest force is calculated with RELAP5 code, which gives only ~50 N at discharge point to environment. These results show that with RELAP5 a much better water deposition and steam condensation along the venting system pipes is calculated compared to COCOSYS.

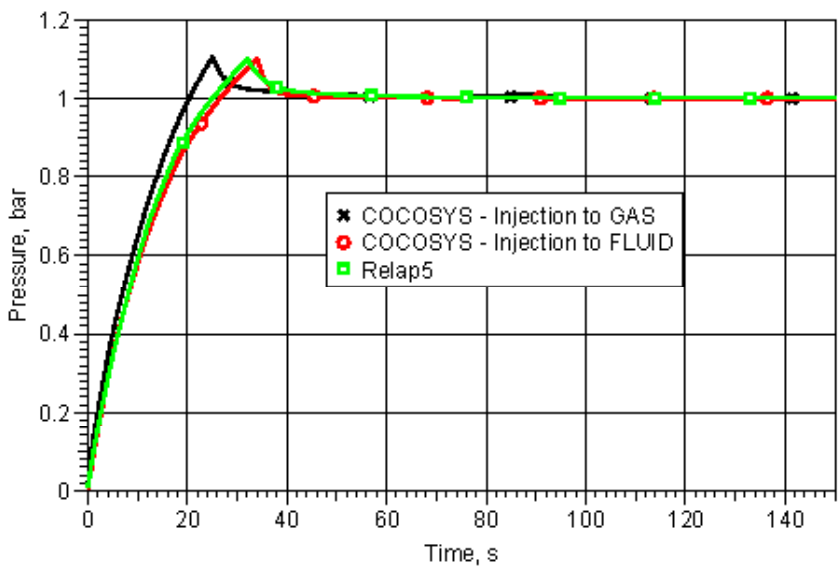

Figure 1.9
Comparison with RELAP5 results: Pressure in the nodes

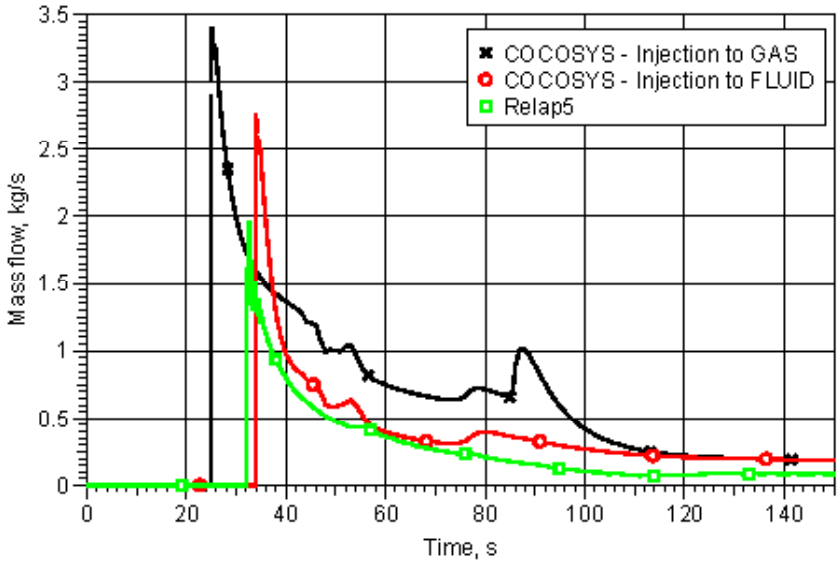

Figure 1.10
Comparison with RELAP5 results: Flow rate through the burst disk

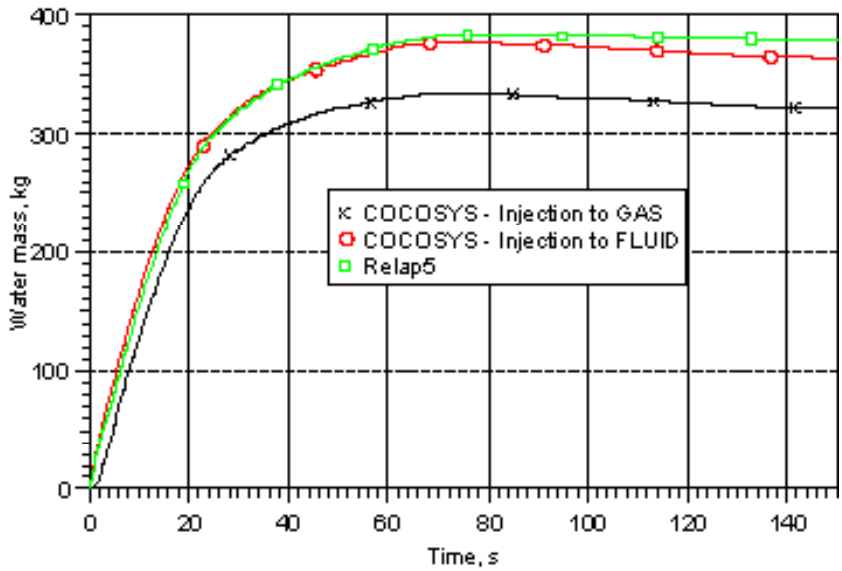

Figure 1.11
Comparison with RELAP5 results: Water mass in PV

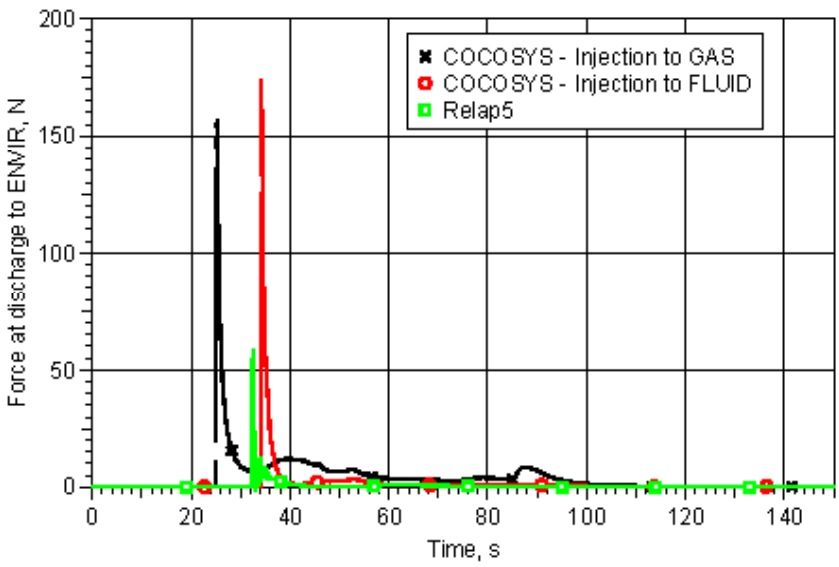

Figure 1.12
Comparison with RELAP5 results: Force acting at the exit from venting system to the environment

1.3.3 Failure of opening of burst disk at 1.1 bar

To investigate the reliability of the venting system, it was decided to perform the analysis assuming that the first burst disk with the opening set point 1.1 bar fails to open. The results of the performed analysis are presented in Figure 1.13 – Figure 1.15.

Figure 1.13 compares the base case scenario with the scenario (curves "Disk1.1_...") with one failed burst disk (curves "Disk1.2_..."). One could see that if the first burst disk fails, then the maximal pressure in PV increases to ~1.22 bar. After that the pressure in PV decreases, and after ~50 s the pressure behavior is the same as in the base case scenario. The maximal pressure in the last node of the venting system piping (node CHIMNEY) reaches 1.1 bar. The performed analysis shows that the diameter of the burst disk is enough to prevent the further rise of pressure in the plasma vessel.

Figure 1.14 presents the mass flow rate through the burst disks in case of both accident scenarios. One could see that in case of scenario with failed to open burst disk the first burst disk stays closed while the second opens later after ~32 s and the flow rate through this burst disk is higher. This

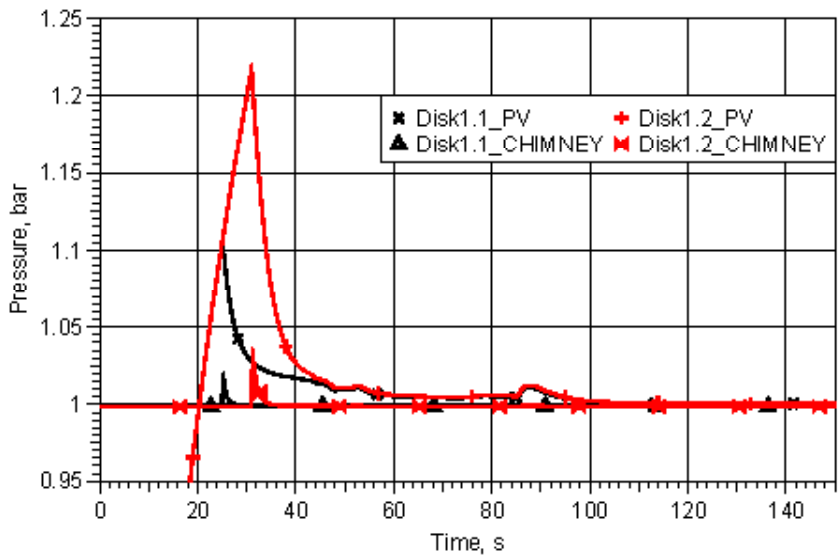

Figure 1.13
Failure of opening of burst disk at 1.1 bar: Pressure in the nodes

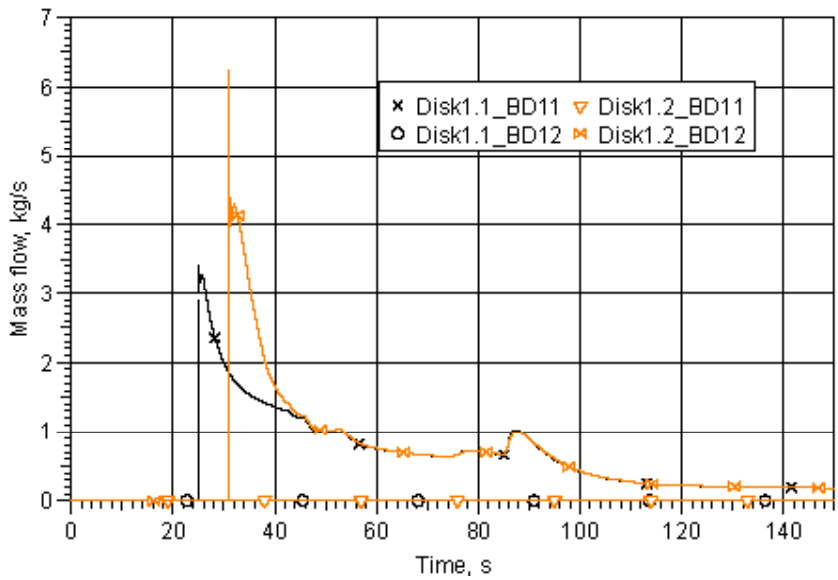

Figure 1.14
Failure of opening of burst disk at 1.1 bar: Flow rate through the burst disks

difference is caused by the larger pressure differences in the piping. After the peak of flow rate decreases, and after ~50 s it becomes the same as in the base case scenario.

Figure 1.15 presents the total amount of water in the piping of venting system. This parameter was received summing up the water mass in each node. It is clearly seen that in case of failed to open burst disk scenario, the steam starts condensing in the piping later, but more steam is condensed due to a larger heat transfer area (the longer branch of piping is opened). In base case scenario at the end of the analyzed accident period, the total mass of water in the piping is ~15.5 kg, while in case of failed to open burst disk scenario it is ~18 kg.

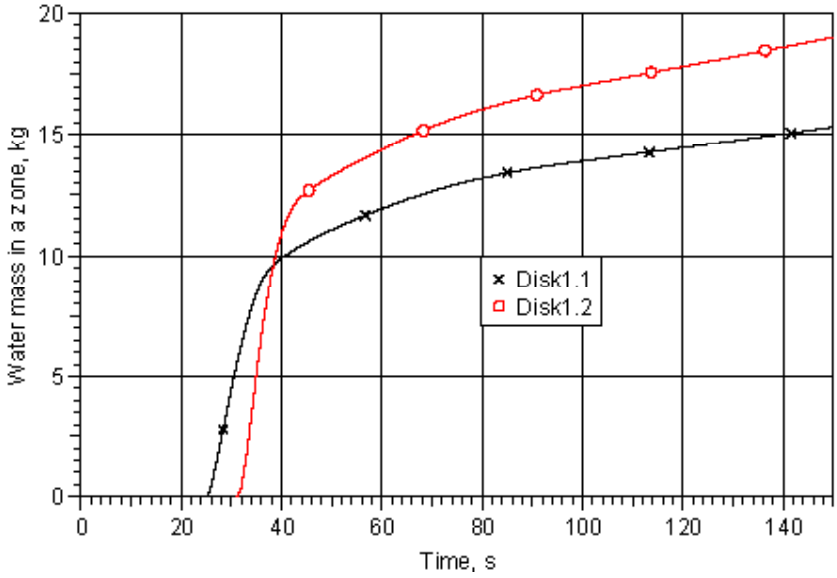

Figure 1.15
Failure of opening of burst disk at 1.1 bar: Total water mass in piping

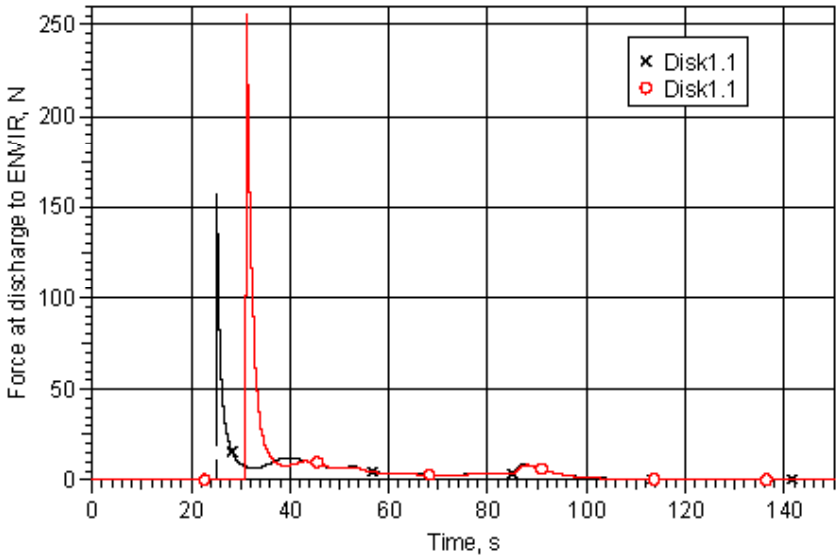

Figure 1.16
Failure of opening of burst disk at 1.1 bar: Force acting at the exit from venting system to the environment

1.3.4 Temperature of outside environment 0 °C

Taking into account that a certain part of the venting system piping is located outside the building, it was decided to perform an analysis assuming that the temperature in the environment is 0 °C, i.e. the accident happens in the colder period of the year. Figure 1.17 shows that no noticeable pressure difference is

observed compared with the base case scenario, i.e. the disk of 1.1 bar opening set point opens as designed. Figure 1.18 compares the total water mass in the piping. There is a slight difference – more steam is condensed assuming the colder temperature in the environment, but the difference is not significant due to small length of the pipe outside the building (assumed 2 m length in the environment).

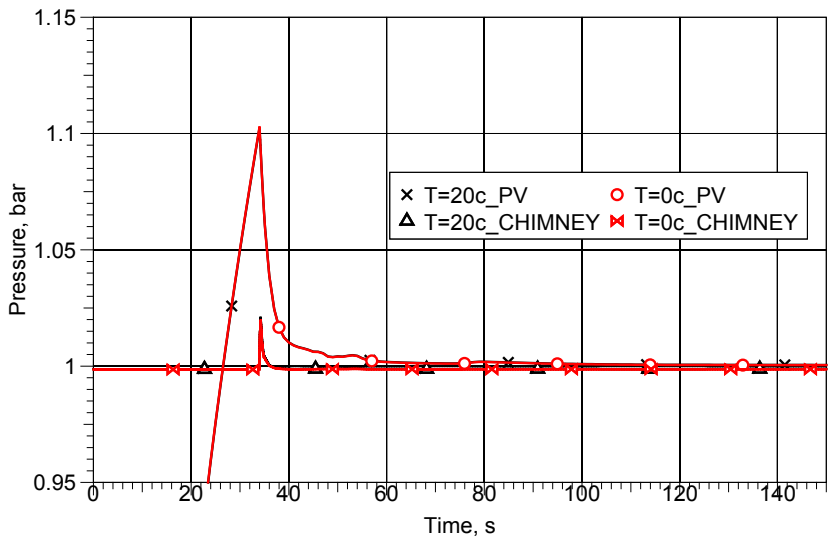

Figure 1.17
Temperature of the outside environment 0 °C: Pressure in the nodes

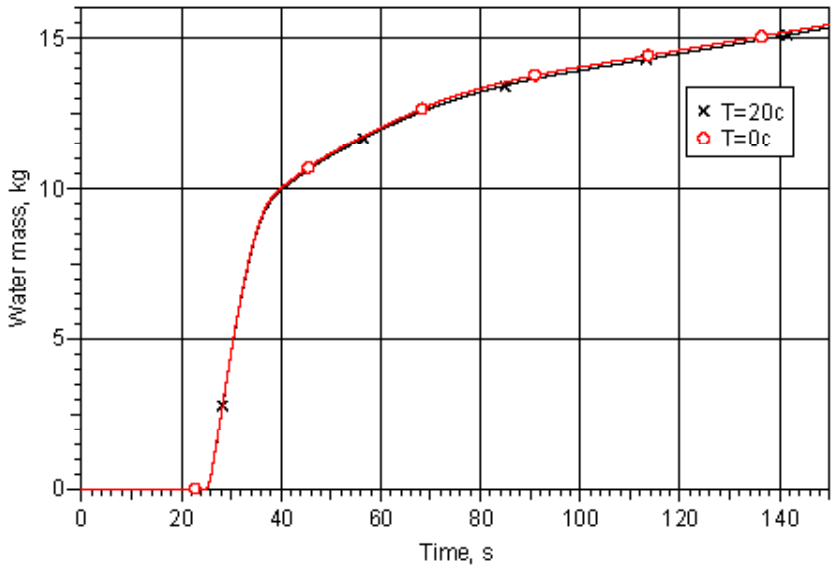

Figure 1.18
Temperature of the outside environment 0 °C: Total water mass in piping

1.3.5 Influence of pressure losses inside venting system pipes

The most uncertain parameter is the pressure losses in the piping of the venting system. These loses appear due to roughness of inner surface of the pipes and local losses on different pipe fittings, e.g. bends, branches, expansions, etc. There are a number of different fittings in the W7-X Plasma Vessel venting system, and they were taken into account to develop the base case model, nevertheless some uncertainty exists, and in the course of the accident, steam would be condensing on the inner surface of the piping, which could increase the resistance to flow as well. Therefore,

it was decided to investigate the influence of this parameter on the accident progression. Two additional runs of the code were performed: 1) assuming that all pressure loss coefficients for junctions between nodes are 2 times higher and; 2) assuming that all pressure loss coefficients for junctions between nodes are 5 times higher. The performed analysis is compared to the base case scenario. This analysis also covers impact of the condensed water film on the inner surface of piping, because the water film could enhance the friction losses.

Figure 1.19 shows that there is only minor influence of pressure loss coefficient on the maximal pressure peak in PV. The influence of the pressure losses is observed in pressure behavior in longer term after the first peak. One could see that the larger pressure losses, the slower pressure decrease is observed, but in all cases after 120 s, the pressure in PV is close to the atmospheric.

The difference is observed in mass flow through the ruptured disk as well (Figure 1.20). As it was expected, the larger pressure losses are assumed, the less maximal mass flow through the opened burst disk is observed. The slower change of the flow causes that during the periods of 40–70 s and 90–110 s the flow rate through the opened disk is even larger than in case of base case scenario.

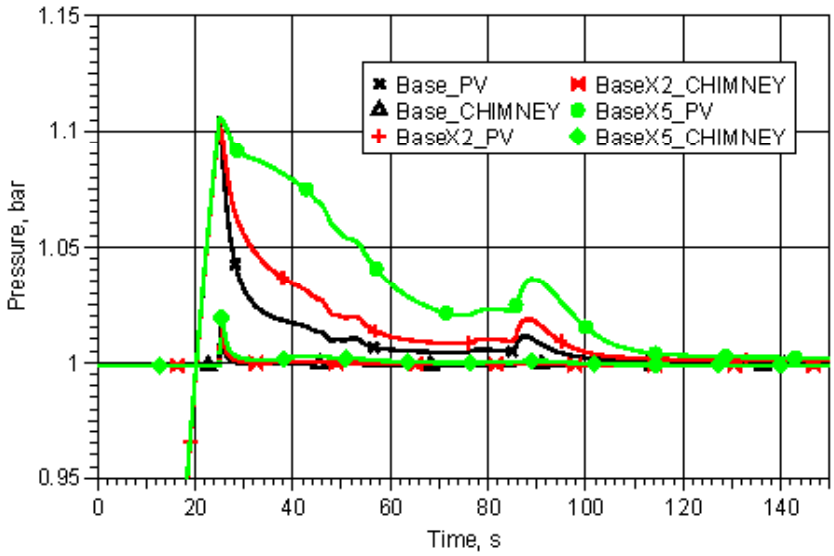

Figure 1.19
Pressure losses: Pressure in the nodes

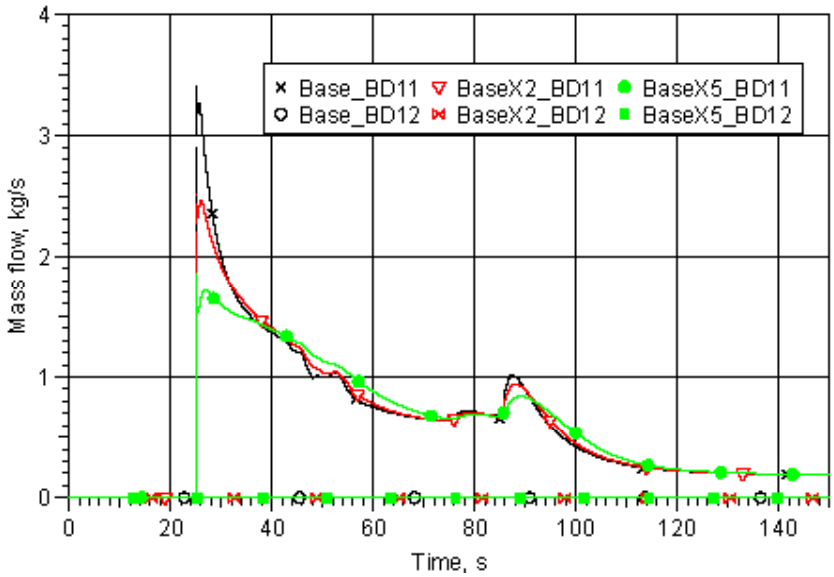

Figure 1.20
Pressure losses: Flow rate through the burst disk

Figure 1.21 shows that there is a smaller water mass in the piping when larger pressure losses are assumed. The reason is that less steam enters the piping and more stays in the plasma vessel, but the difference is not significant.

Figure 1.22 shows that the higher pressure losses are along the venting system the less force is acting on the pipe exit to the environment. The reason is that the mass flow through this junction is smaller, even though this is not observed on the condensed steam mass collected in the piping. Assuming pressure losses 5 times higher than the base case leads to 4 times less force acting on the pipe exit to the environment.

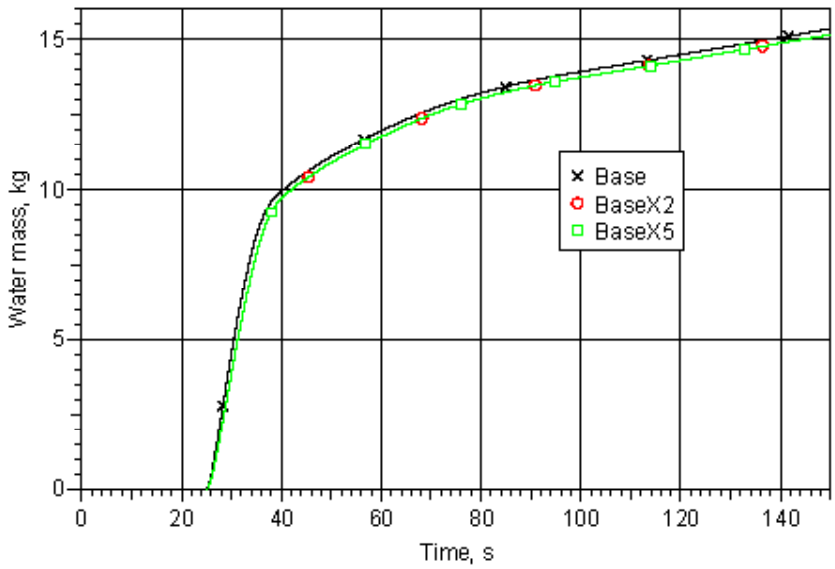

Figure1.21
Pressure losses: Total water mass in piping

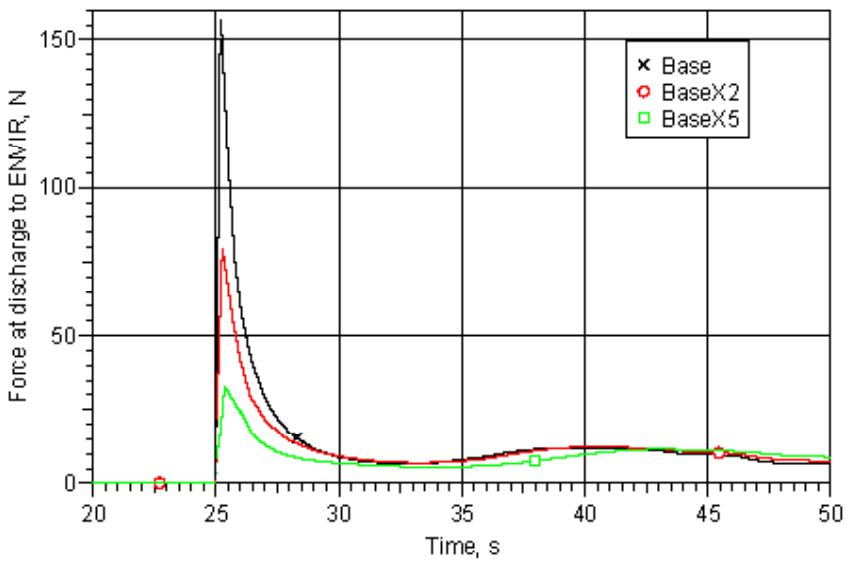

Figure 1.22
Pressure losses: Force acting at the exit from venting system to the environment

1.4 Conclusions

The analysis of 40 mm pipe rupture inside the Plasma Vessel was performed using COCOSYS code in order to estimate if the installed burst disks and venting system piping are capable to remove the accident-generated steam from Plasma Vessel during operation in “baking” mode.

The results of the performed analysis showed that:

- If the burst disks open as designed, the maximal pressure is 1.11 bar, thus the diameter of the installed burst disk and the piping of the venting system ensures prevention of further pressure rise.
- If the first burst disk fails to open, then the maximal pressure in PV is 1.22 bar, thus opening of the second burst disk prevents further pressure rise in pressure vessel.
- The temperature of the outside environment does not have a significant influence on the results.
- The pressure losses in the venting system pipes have only minor influence on maximal pressure in plasma vessel, but it influences depressurization rate, i.e. the larger pressure losses the slower change in pressure is observed.
- Comparison between COCOSYS and RELAP5 results showed influence of different assumptions in both codes regarding heat and mass exchange processes. RELAP5 gives much better water deposition and steam condensation along the piping of Plasma Vessel venting system, which leads to much smaller forces acting at the discharge point to the environment.

2 LIMIT ANALYSIS OF THE PORT WELDS BETWEEN THE PLASMA VESSEL AND THE PORTS IN THE W7-X CRYOSTAT SYSTEM

The port welds between the plasma vessel and the ports in W7-X cryostat system was investigated. The structural integrity analysis of the welding connections was analysed for the following ports / port combinations:

- Welding connection between the port AEQ20 and the PV shell with a 1 mm gap.
- Welding connection between the port AEU30 and the PV shell with a 1 mm and 6 mm gap.
- Welding connection between the port AEK20 and the PV shell with a 1 mm gap.

These ports were modelled using the FEM technique as 3D bodies together with the regions of the PV shell around the ports and the welding seam. The models were loaded with forces, moments, and pressure provided by IPP and subjected to the limit analysis.

The main objectives of this analysis are:

- Create 3D FE models of the welded connections for the selected ports that could be later reused for analysis under different loads, or with different criteria.
- Calculate load scaling factors for all the ports under analysis.

For the geometrical modelling CAD program SolidWorks was applied. Structural analysis of the ports was performed using ABAQUS code.

The limit analysis results of the welding connection between the port AEU30 and the PV shell with a 6 mm gap were presented as an example in this document.

2.1 Geometrical and finite element models of the ports welds

The modelling of the welding connection between the port AEU30 and the PV shell was performed in two steps. In the first the geometrical 3D models of these port welds were prepared using the software SolidWorks. The prepared model of the port AEU30 and the PV shell with a 6 mm gap is presented in the Figure 2.1. This model was transferred to FE software ABAQUS/Standard. The finite element models of the welding connection between the port AEU30 and the PV shell were prepared using this software. The prepared model is presented in the Figure 2.2 and Figure 2.3. Model of port connection consist of a shell modelled portion PV, a port, and a solid modelled central part (CP). Central part includes a portion of PV and a port and a full weld seam (see Figure 2.1b).

2.2 Elements used for models

Port AEU models: used linear four node shell elements with reduced integration S4R for shell parts of port and quadratic eight node shell elements with reduced integration S8R of the shell part of PV (see Figure 2.2a). Central part, part of plasma vessel and port (see Figure 2.2b) are modelled as solid, are meshed using a 20-node quadratic brick element with reduced integration C3D20R. Weld seam is meshed using a 20-node quadratic brick element integration C3D20 (see Figure 2.3).

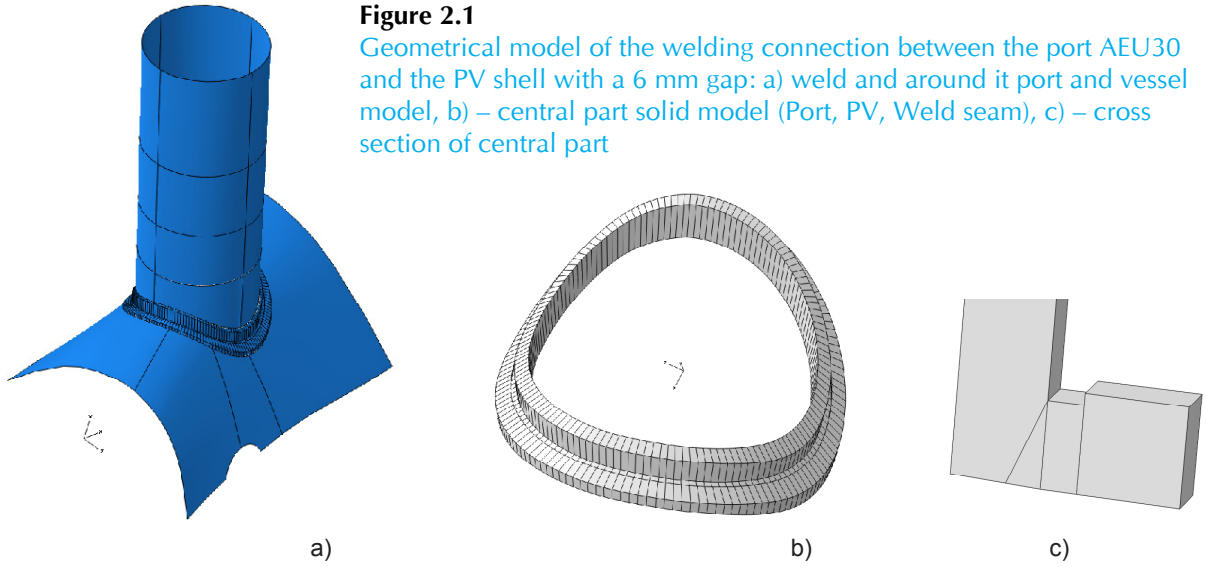

Figure 2.1
Geometrical model of the welding connection between the port AEU30 and the PV shell with a 6 mm gap: a) weld and around it port and vessel model, b) – central part solid model (Port, PV, Weld seam), c) – cross section of central part

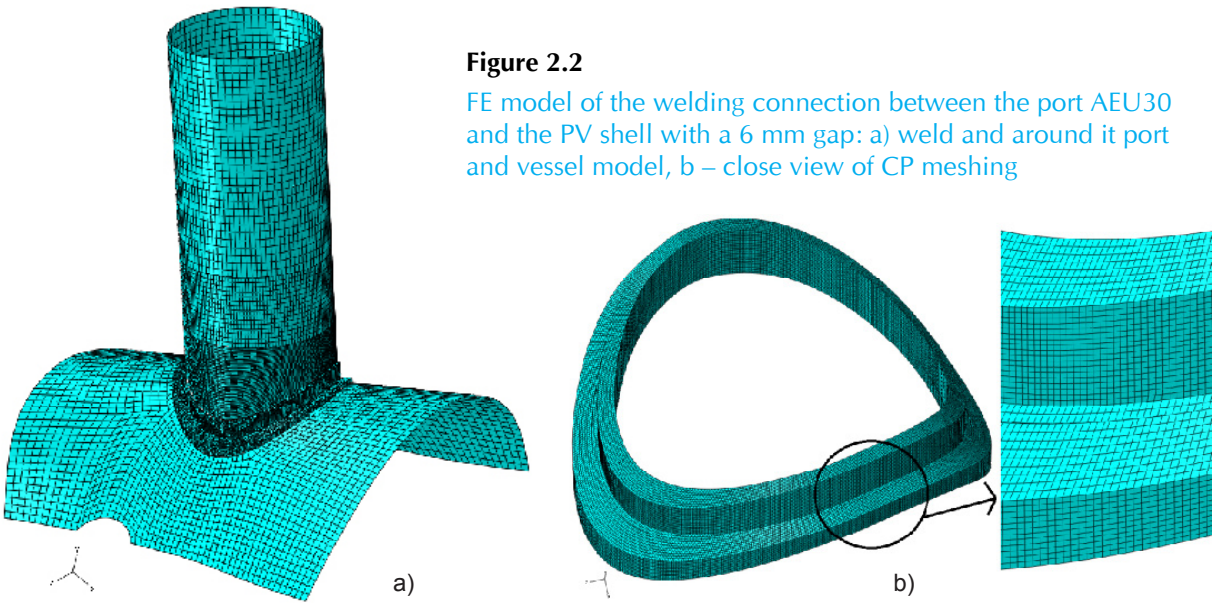

Figure 2.2
FE model of the welding connection between the port AEU30 and the PV shell with a 6 mm gap: a) weld and around it port and vessel model, b – close view of CP meshing

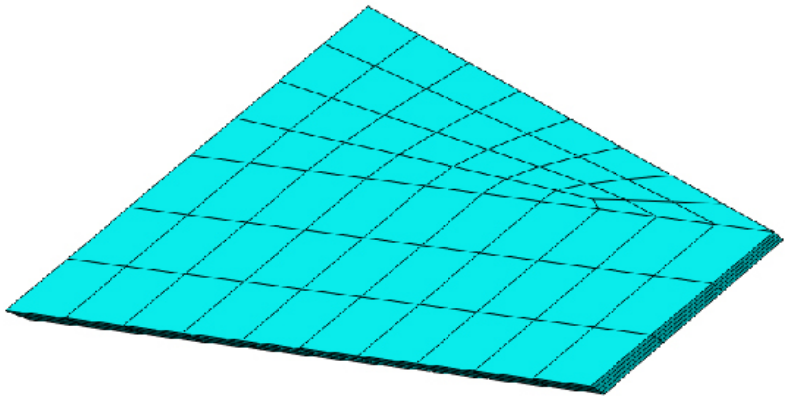

Figure 2.3
Cross sectional view of AEU30 a 6 mm gap SF1 weld seam meshing

2.3 Material properties

The PV shell and the ports are made of the material WS-Nr. 1.4429. The welding material is WS-Nr. 1.4455. The geometrical and material data of the welding connection between the port AEU30 and the PV shell are presented in Table 2.1. The names of the port welds parts used in Table 2.1 are presented in Figure 2.4.

Table 2.1 Material properties

Property	*T, °C*	*Shell-AEU-1*	*Shell-AEU-2*
Thickness, mm	–	16.05	14.05
Density, kg/mm^3	0–100	2.0511×10^{-05}	1.1513×10^{-05}
Young modulus,	0	1.98×10^{5}	
MPa	20	1.96×10^{5}	
	100	1.90×10^{5}	
Poisson's ratio	0–100	0.3	0.3
Coefficient of	0	1.60×10^{-5}	
thermal	20	1.61×10^{-5}	
expansion, K^{-1}	100	1.67×10^{-5}	

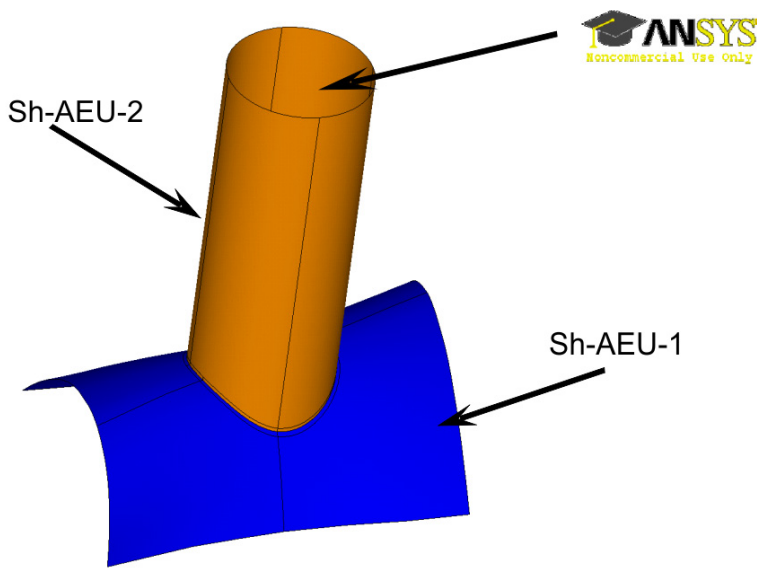

Figure 2.4
Port AEU30 and the PV shell around it

2.4 Allowable stresses

The magnitude of the allowable stress for evaluation of the analysis results is chosen based on the KTA code. The KTA code suggests mostly the same approach as the ITER design criteria, that is, the stress has to be categorized as primary or secondary, and membrane (general or local) or bending. Limit values of stress for different load cases are presented in Table 2.2. The limit values of stresses were used for evaluation of FE analysis results. The material properties at room temperature presented in Table 2.2 are used in calculation for welds.

Table 2.2 Allowable stresses

Material WS-Nr. 1.4429	*Limit Formulae*	*Limit Value, MPa*
At Room Temperature (RT):		
s_m = 2/3 $R_{p1,0}$; Tensile Strength: s_u = 580 MPa Yield Strength: s_y = 320 MPa		
$\mathbf{s_m}$ = 2/3*320 = **213** MPa		
(1) Primary General Membrane stress: $\mathbf{P_m}$	$\sigma < 1.0 \times s_m$	**213**
(2) Primary Local Membrane stress: $\mathbf{P_L}$	$\sigma < 1.5 \times s_m$	**320**
(3) Primary Membrane + Primary Bending stress: $\mathbf{P_L}$ (or $\mathbf{P_m}$) + $\mathbf{P_b}$	$\sigma < 1.5 \times s_m$	**320**
(4) Primary + Secondary stress: $\mathbf{P_L}$ (or $\mathbf{P_m}$) + $\mathbf{P_b}$ + **Q**	$\sigma < 3.0 \times s_m$	**640**
At temperature of 150°C:		
s_m = 2/3 $R_{p1,0}$; Tensile Strength: s_u = 490 MPa Yield Strength: s_y = 218 MPa		
$\mathbf{s_m}$ = 2/3*218 = **145** MPa		
(1) Primary General Membrane stress: $\mathbf{P_m}$	$\sigma < 1.0 \times s_m$	**145**
(2) Primary Local Membrane stress: $\mathbf{P_L}$	$\sigma < 1.5 \times s_m$	**218**
(3) Primary Membrane + Primary Bending stress: $\mathbf{P_L}$ (or $\mathbf{P_m}$) + $\mathbf{P_b}$	$\sigma < 1.5 \times s_m$	**218**
4) Primary + Secondary stress: $\mathbf{P_L}$ (or $\mathbf{P_m}$) + $\mathbf{P_b}$ + **Q**	$\sigma < 3.0 \times s_m$	**436**

2.5 Boundary conditions

In order to simulate the load case 5 (LC5), the outer boundaries of the PV (marked "Sh-AEU-1" in Figure 2.4) were constrained in the following way, the displacements of the edges were restricted in all directions, but rotations are allowed. Restrained edges of model shell are highlighted in Figure 2.5.

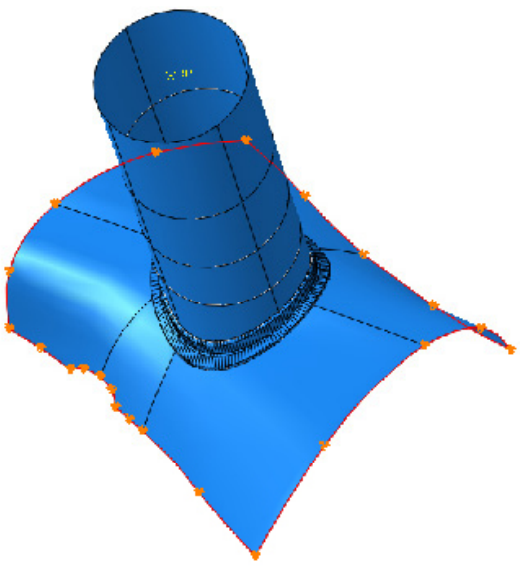

Figure 2.5
FE model boundary conditions of Port AEU

2.6 Loading for analysis load case 5, SF1.0

The loads were applied at the loading step that corresponds to the loading factor of 1.0 are listed in Table 2.3. "Outer pressure" means that the pressure is applied from the side where the port is attached to the PV shell. The loads are multiplied with the safety value of 1.2 in order to take possible imprecision of the modelling into account. Safety value of 1.2 is not applied to gravity.

Table 2.3 Loads on the sub-model for the LC 5

Load type	*Direction*	*Port AEU30*
Temperature, °C	–	20
Outer pressure, MPa	–	0.1013 × 1.2 = **0.1216**
Forces applied the end of the port (marked with thick green arrow in Figure 2.4	F_x, kN	26.034 × 1.2 = **31.241**
	F_y, kN	-16.458 × 1.2 = **-19.749**
	F_z, kN	3.515 × 1.2 = **4.218**
Moments applied the end of the port (marked with thick green arrow in Figure 2.4)	M_x, kN*mm	214.009 × 1.2 = **256.811**
	M_y, kN*mm	4163.394 × 1.2 = **4996.073**
	M_z, kN*mm	-26504 × 1.2 = **-31804**

Forces and moments are applied to force-moment addition point called shortly FM. FM point is connected to port end nodes (highlighted magenta) by MPC beam type constrain, showed in Figure 2.6.

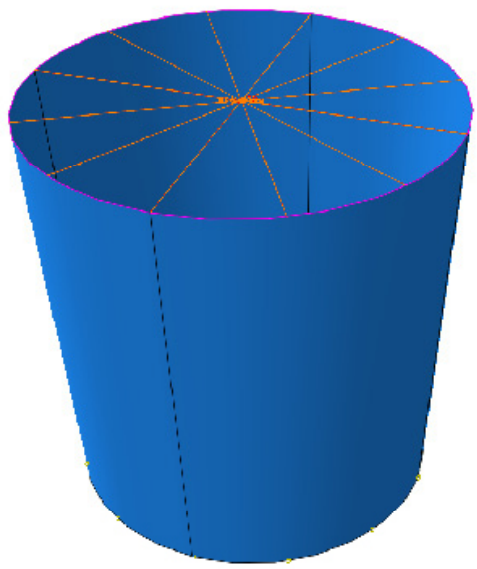

Figure 2.6
FM point coupling to port

Section of shell parts of port are connected to each other (highlighted red) by tie type constrain, showed in Figure 2.7. The shell parts of port and PV are connected to solid center part (highlighted magenta) by shell to solid coupling type constrain, showed in Figure 2.8.

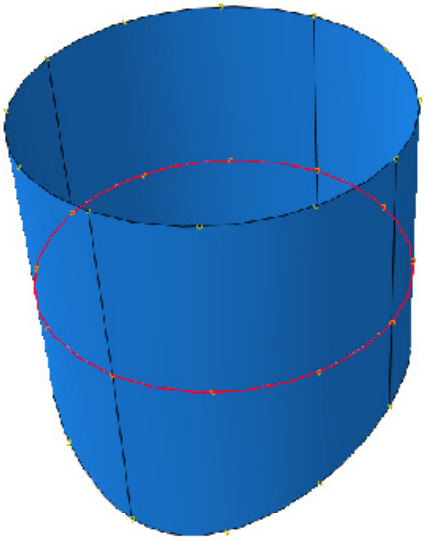

Figure 2.7
Shell-to-Shell coupling

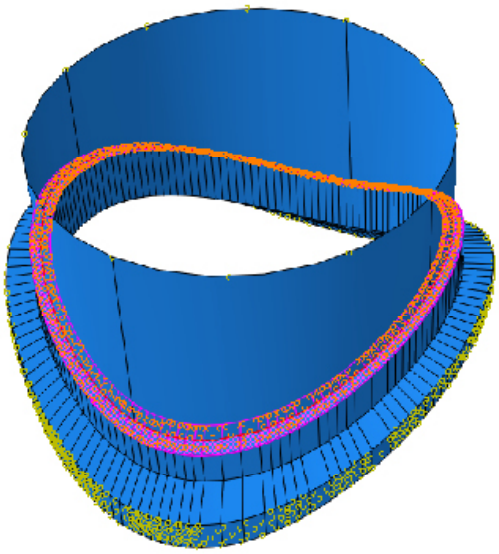

Figure 2.8
Shell-to-Solid coupling

2.7 Results of analyses

2.7.1 Results of stress analysis

The stress analysis of the welding connection between the port AEU30 and the PV shell was performed for Load case 5.

The given results are:

- Von Mises equivalent stress in full assembly;
- Von Mises equivalent stress in shell modelled Plasma Vessel;
- Von Mises equivalent stress in shell modelled Port;
- Von Mises equivalent stress in solid modelled Port-Weld-PV cross section;
- Von Mises equivalent stress in Weld seam;
- Von Mises equivalent stress in mostly loaded Element.

The weld material for this port was chosen as a material with ideal plastification at the level of $1.5*s_m*K_{weld}$. Here K_{weld} is a weld efficiency factor. For these welds the values K_{weld} = 0.7 and K_{weld} = 0.85 were taken. The analysis results for AEU30 port were presented at weld efficiency factor value K_{weld} = 0.7.

In this section, the stress analysis of the welding connection between the port AEU30 and the PV shell using the weld efficiency factor value 0.7 was presented. The history of the displacement of the point where loads are applied during the analysis is presented in Figure 2.9.

Displacement magnitude distributions in model AEU30 with a 6 mm gap are presented in Figure 2.10. Maximal displacement magnitude 1.584 mm is obtained on wall of port.

Stress distributions in model in the welding between Plasma Vessel and ports AEU30 with a 6 mm gap are presented in Figure 2.11.

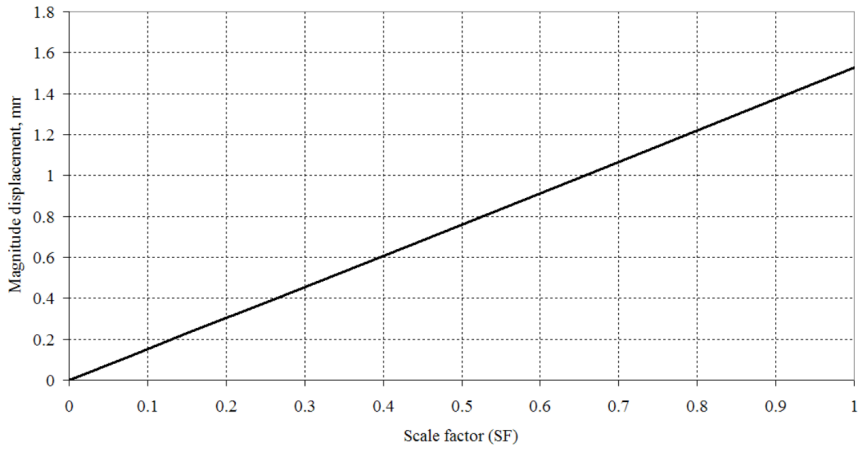

Figure 2.9
Displacement of force-moment addition point

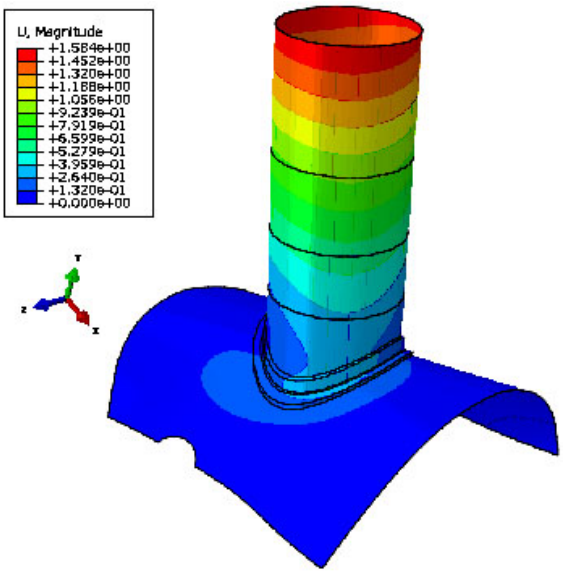

Figure 2.10
Displacement distribution in model

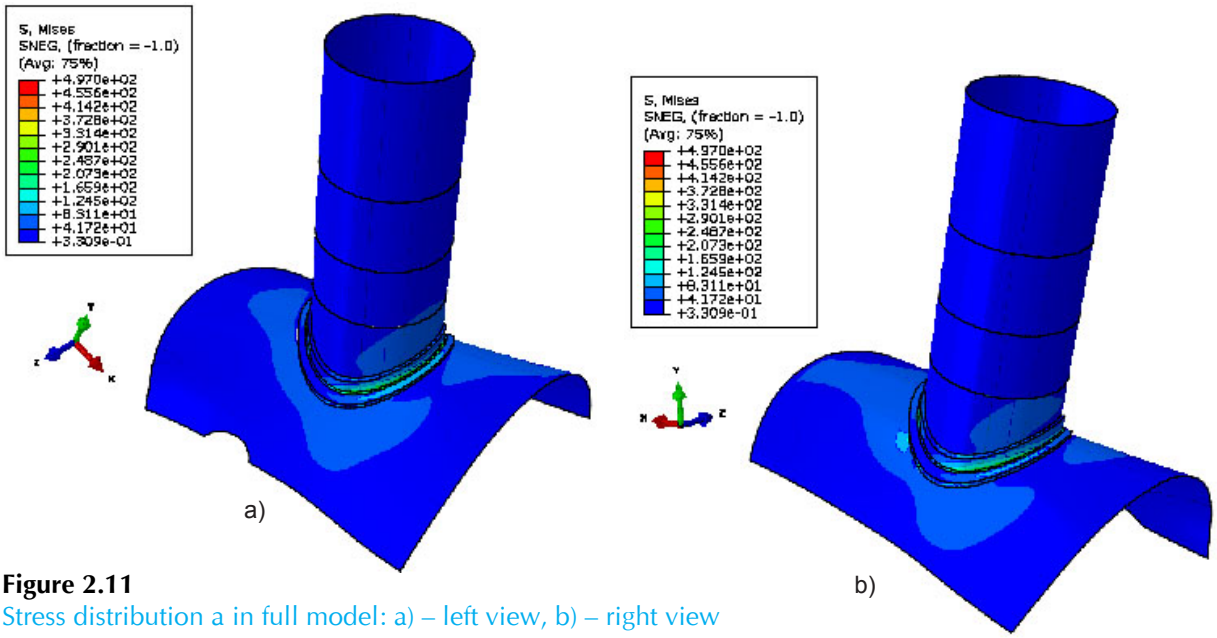

Figure 2.11
Stress distribution a in full model: a) – left view, b) – right view

In the shell part of plasma vessel maximal Von Misses stresses are 150 MPa (Figure 2.12). In the shell part of port maximal Von Misses stresses are 60 MPa (Figure 2.13).

Maximal stress level obtained in model is 497 MPa. These stresses are obtained on the boundary of port to weld region in the solid body of port (Figure 2.14, Figure 2.17). Stress distribution in

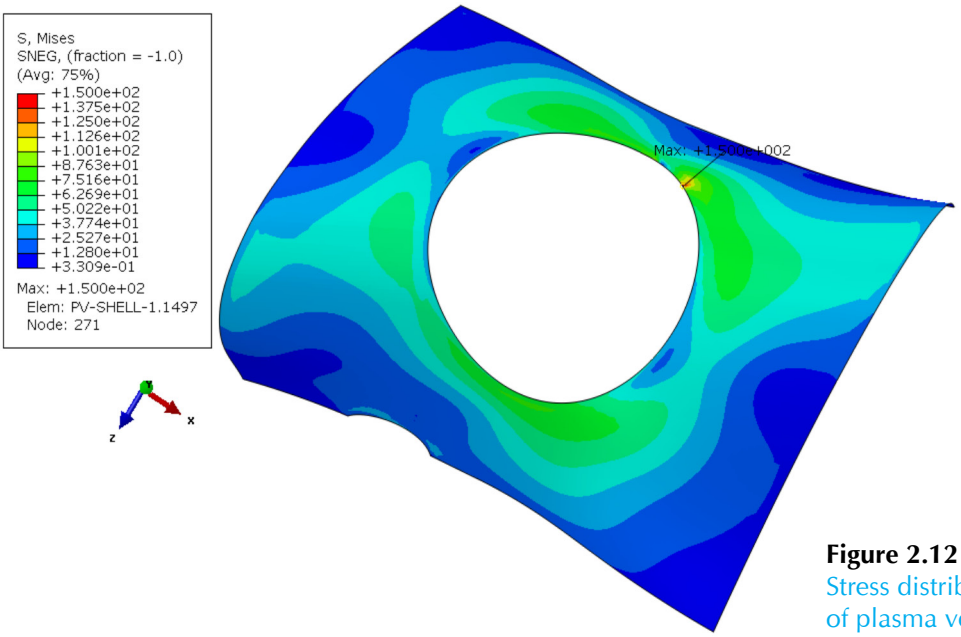

Figure 2.12
Stress distribution in a shell part of plasma vessel

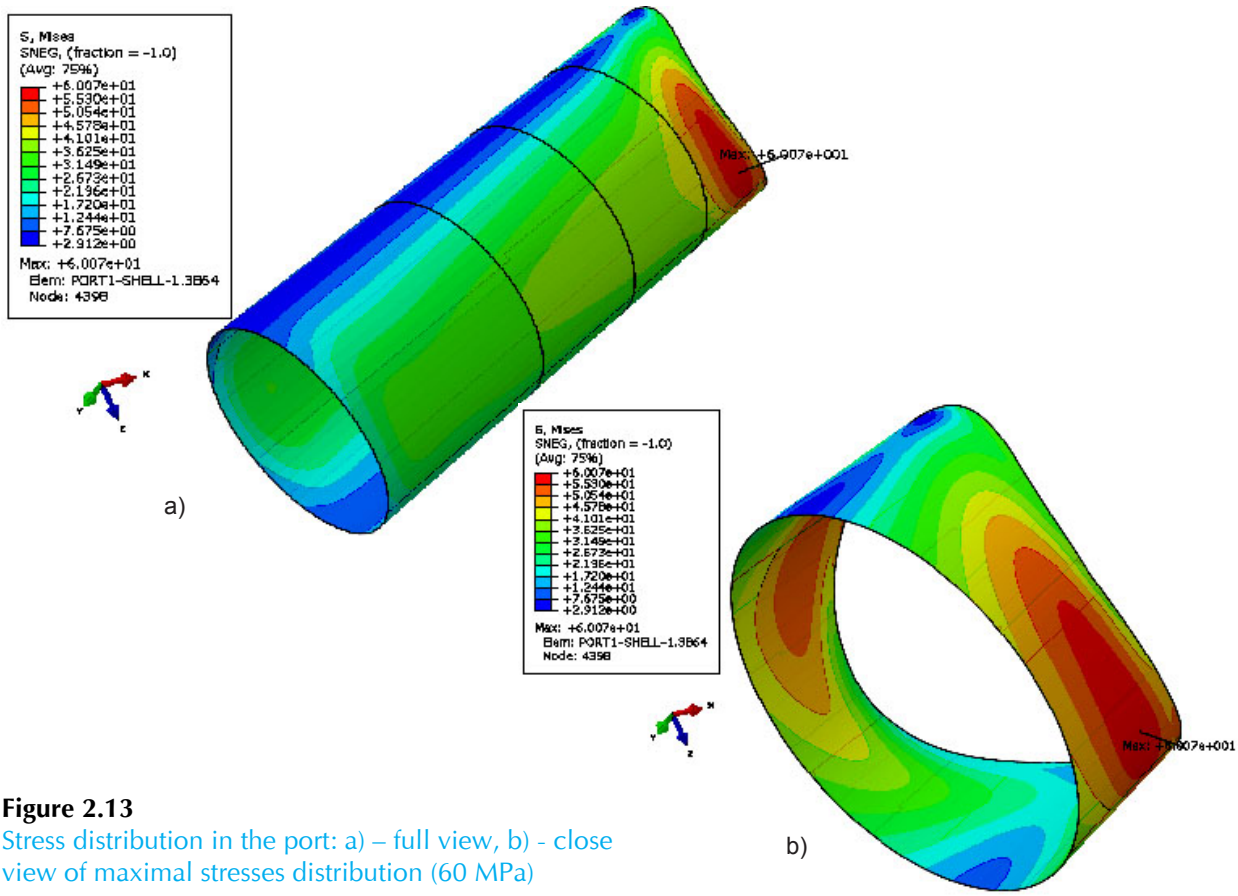

Figure 2.13
Stress distribution in the port: a) – full view, b) - close view of maximal stresses distribution (60 MPa)

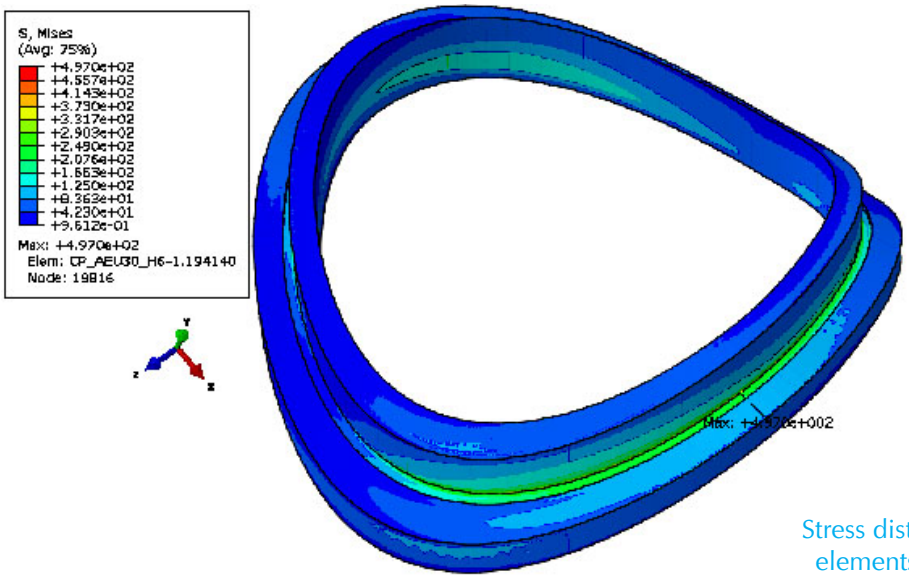

Figure 2.14
Stress distribution in solid modelled elements, maximal stress 497 MPa

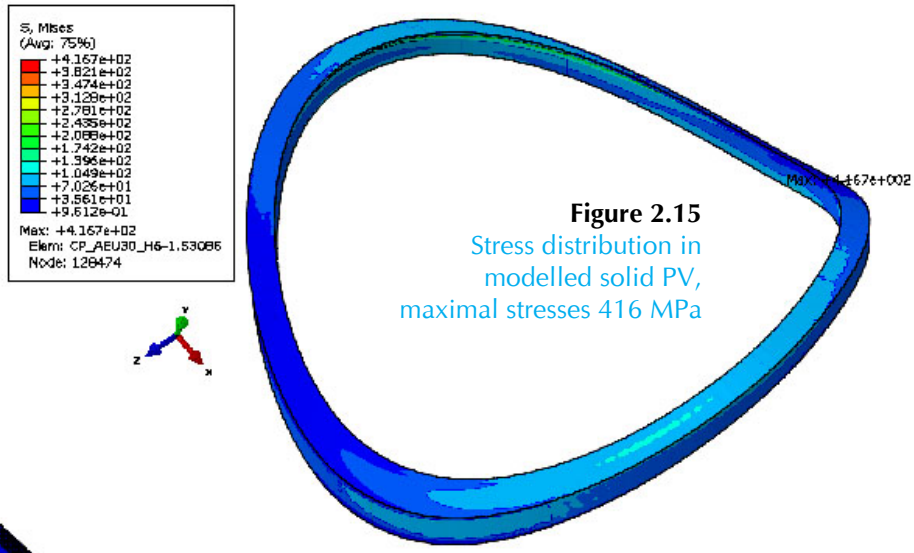

Figure 2.15
Stress distribution in modelled solid PV, maximal stresses 416 MPa

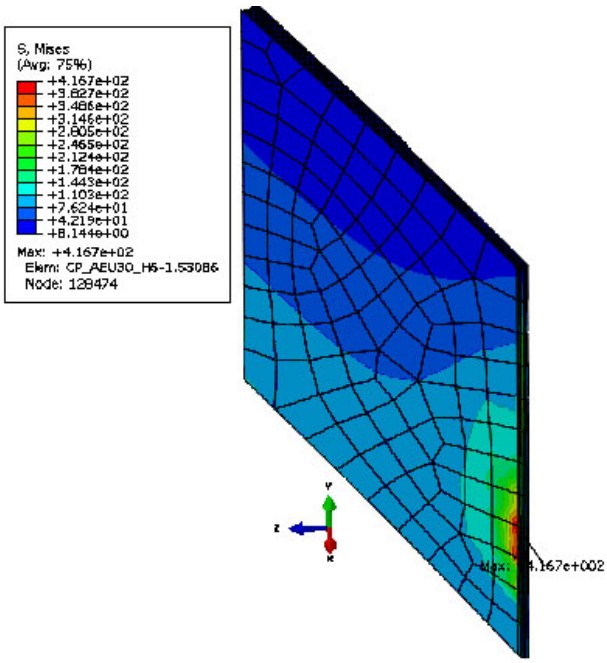

Figure 2.16
Stress distribution in the cross section of modelled solid PV through maximal stresses 416 MPa

cross section of port in area of maximal stress 497 MPa is presented in Figure 2.18. The region of high stress was received only in surface on the connection of port with weld. The stress level in the middle of this cross section reaches about 154 MPa.

Maximal obtained stress level is 416 MPa, on the wall of plasma vessel, close to the edge of weld tip (Figure 2.15). Stress distribution in cross section of weld in area of maximal stress 416 MPa is presented in Figure 2.16. The region of high stress was received only in surface on the connection of vessel with weld. The stress level in middle of this cross section reaches about 144 MPa.

The main interest is the welded zone of the port and PV, modelled as 3D solid. In weld maximal stress level is 301 MPa (Figure 2.19). Stress distribution in cross section of weld in area of maximal stress 3017 MPa is presented in Figure 2.20. In this cross section the line was drawn. The Misses stresses history along path of line of weld cross section is presented in Figure 2.21. The results show that the maximal value of stresses reaches 249.2 MPa. Mean value of stress along path of line of weld cross section is 110 MPa.

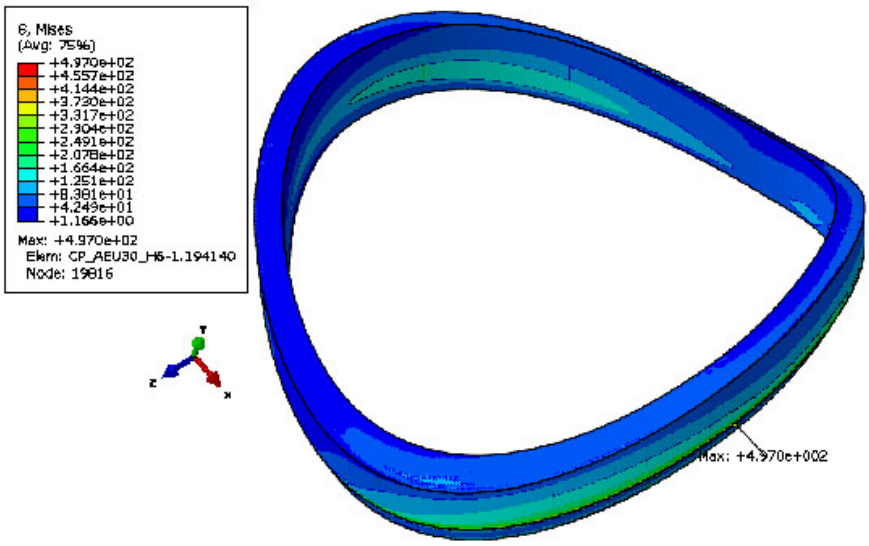

Figure 2.17
Stress distribution in a modelled solid port, maximal stresses 497 MPa

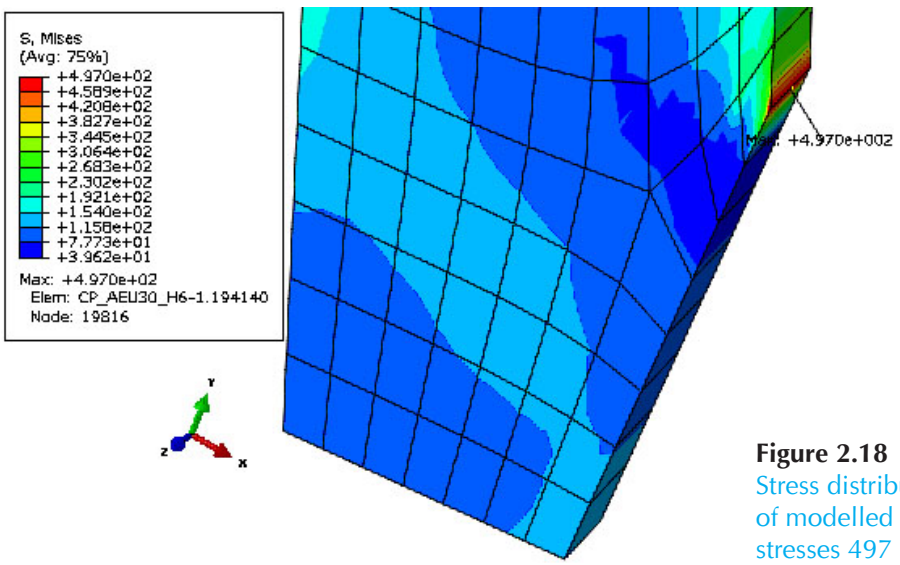

Figure 2.18
Stress distribution in the cross section of modelled solid port through maximal stresses 497 MPa

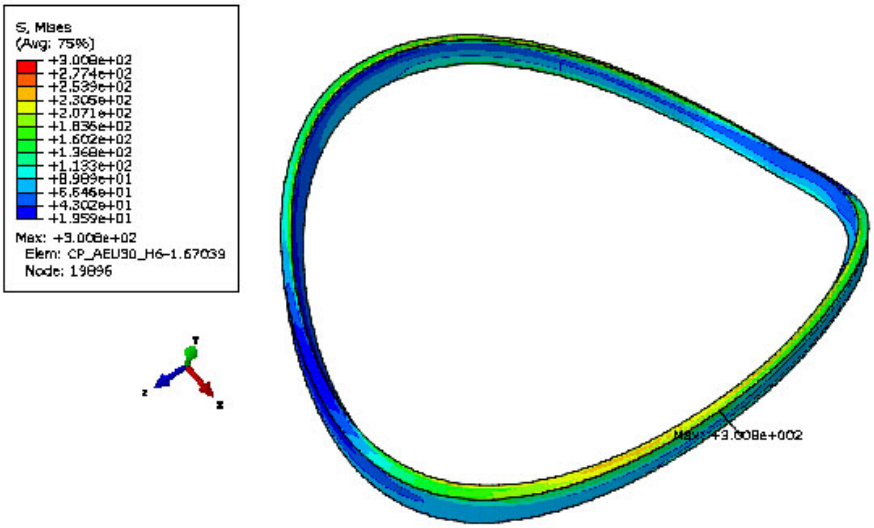

Figure 2.19
Stress distribution in modelled solid weld, maximal stresses 301 MPa

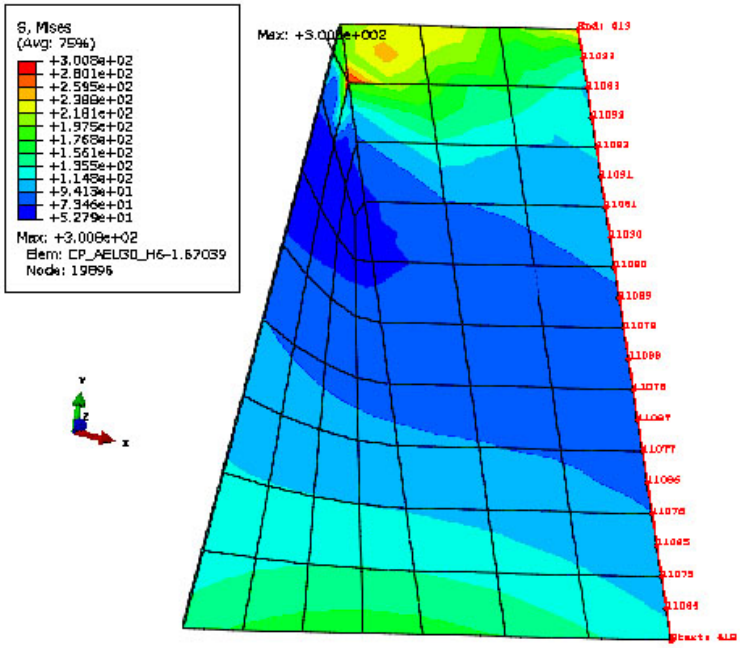

Figure 2.20
Weld seam cross section path of a line along the weld surface

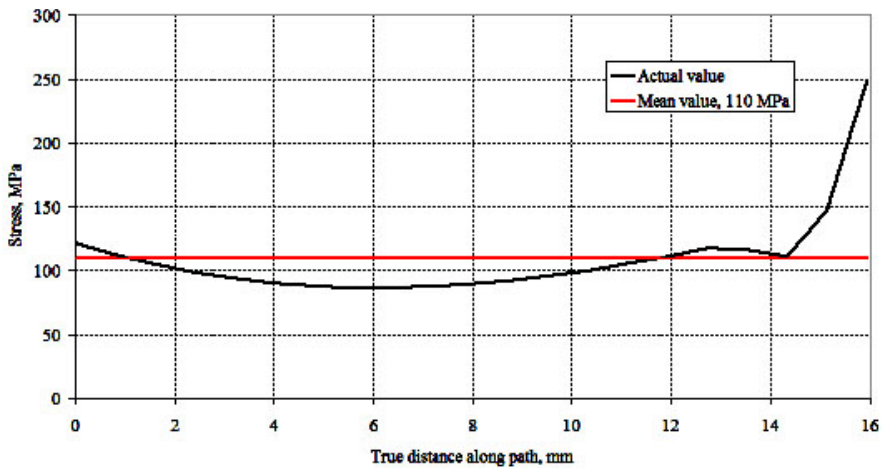

Figure 2.21
Total Misses stress history along the path of the middle line of the weld cross section

The distribution of equivalent plastic strain at port and weld are presented in Figure 2.22 – Figure 2.23. The plastic strain zones appeared in the port connected with the top of the weld (Figure 2.22) and at the top of the weld connected with the port (Figure 2.23), and these areas of this zone are small.

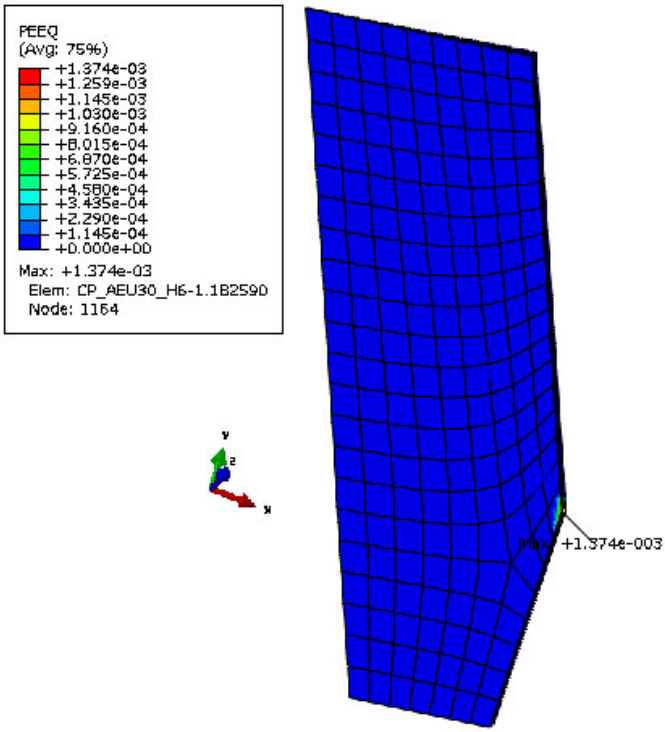

Figure 2.22
Close view of the equivalent plastic strain at integration points of a solid modelled port cross section at maximal value of equivalent plastic strain

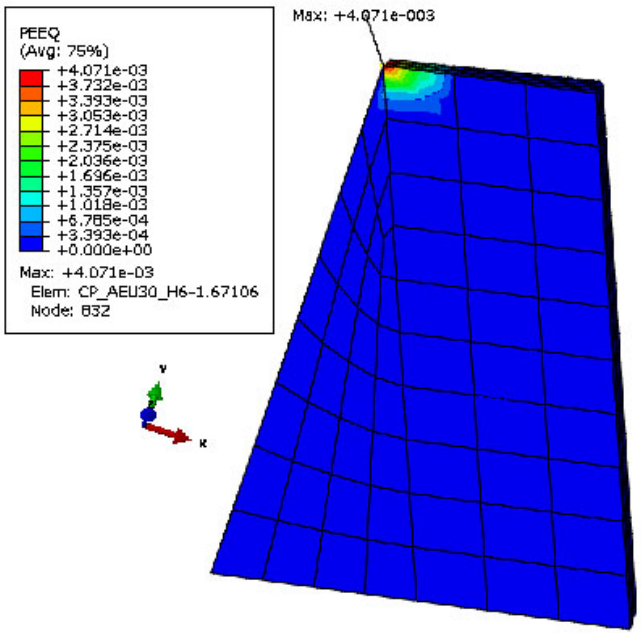

Figure 2.23
Close view of the equivalent plastic strain at integration points of the weld seam cross section at maximal value of equivalent plastic strain

2.72 Results of limit analysis

The limit analysis of the welding connection between the port AEU30 and the PV shell was performed for Load case 5 applying scaling factor 3. Scaling factor (SF) is applied to the dead weight, pressure, forces and moments. The earlier described same model (geometry, materials, boundary conditions, finite elements types) as for stress analysis was used for this limit analysis. Several attempts were done in limit analysis for determination of acceptable loading increments, i.e. that convergence will occur. It was estimated that loading increment 0.075 can be used in the first step of the analysis until scaling factor 0.15, after loading increment 0.1125 and 0.1625 can be used until scaling factor 0.431, and after loading increment 0.25 can be used until scaling factor 3. The convergence was never lost during the limit analysis and scaling factor safely reached the value SF = 3.0.

The limit analysis results of the welding connection between the port AEU30 and the PV shell using the weld efficiency factor value 0.7 were presented. The history of the displacement of the point where loads are applied during analysis is presented in Figure 2.24. Displacement magnitude distributions in this model are presented in Figure 2.25. Maximal displacement magnitude 6.094 mm is obtained on the wall of the port.

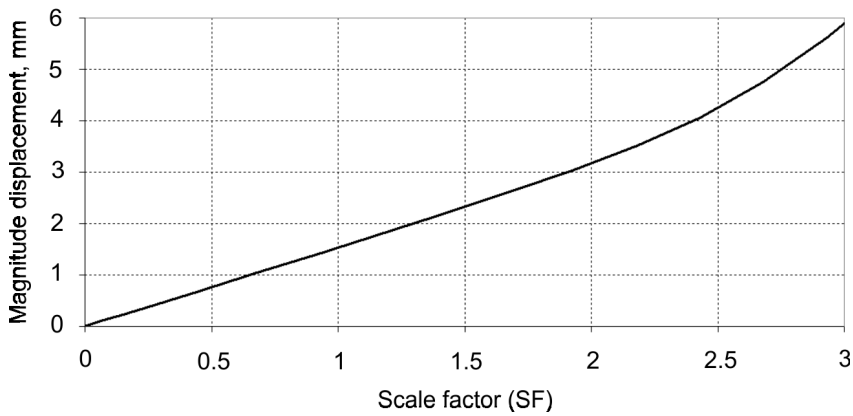

Figure 2.24
Displacement of a force-moment addition point

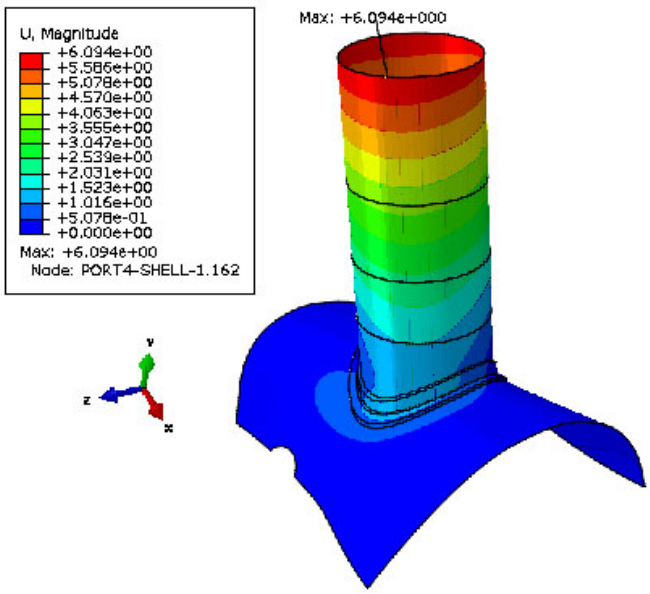

Figure 2.25
Displacement magnitude distribution in AEU30 model

According to the results of the analysis, the fact that displacement of the point where loads are applied starts to increase very rapidly was not detected, and the FE analysis could not converge any more. The convergence was never lost during the analysis, and limit analysis safely reached the SF = 3.0, and the displacements never started to increase very rapidly. Therefore, it is possible to conclude that the limit analysis yielded positive results.

Stress distributions at step of scaling factor 3 in full model of the welding between Plasma Vessel and ports AEU30 with a 6 mm gap are presented in pictures below (Figure 2.26, Figure 2.27). In the shell part of plasma vessel maximal Von Misses stresses are 355 MPa (Figure 2.28). In the shell part of port maximal Von Misses stresses are 209 MPa (Figure 2.29 and Figure 2.30).

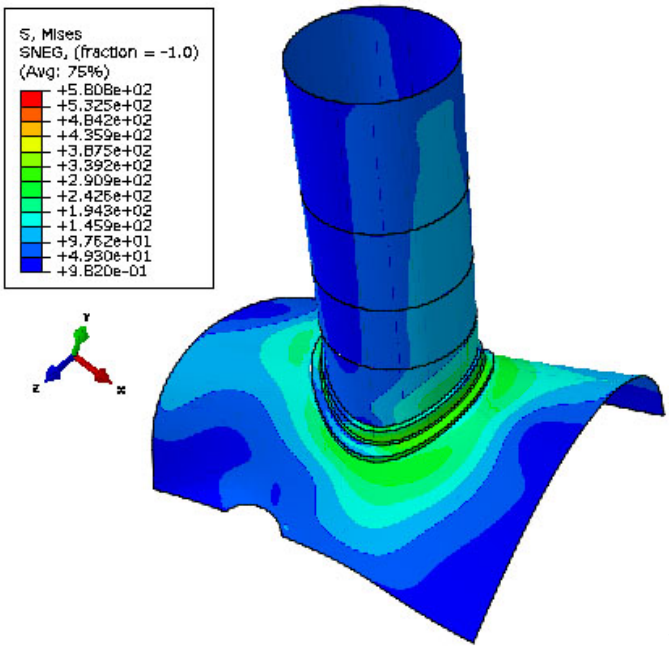

Figure 2.26
Stress distribution in a full model

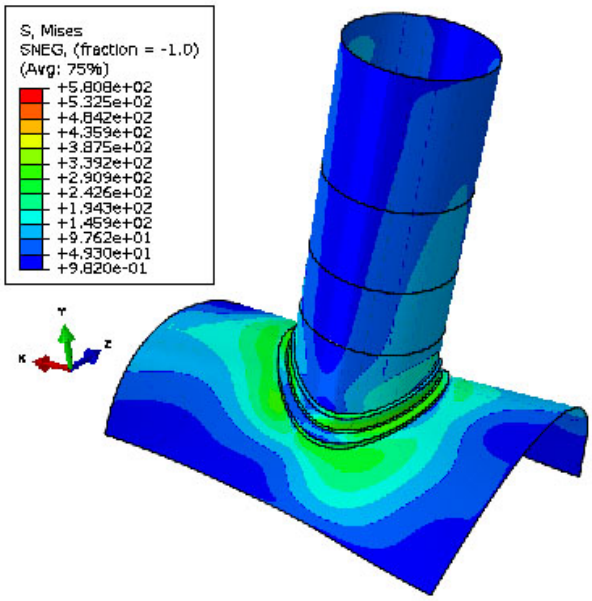

Figure 2.27
Stress distribution in a full model right view

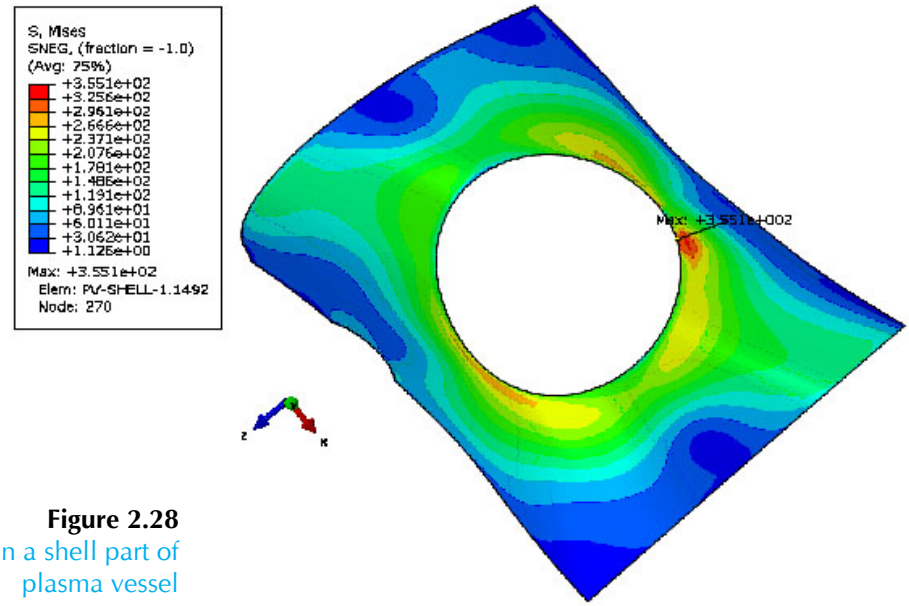

Figure 2.28
Stress distribution in a shell part of plasma vessel

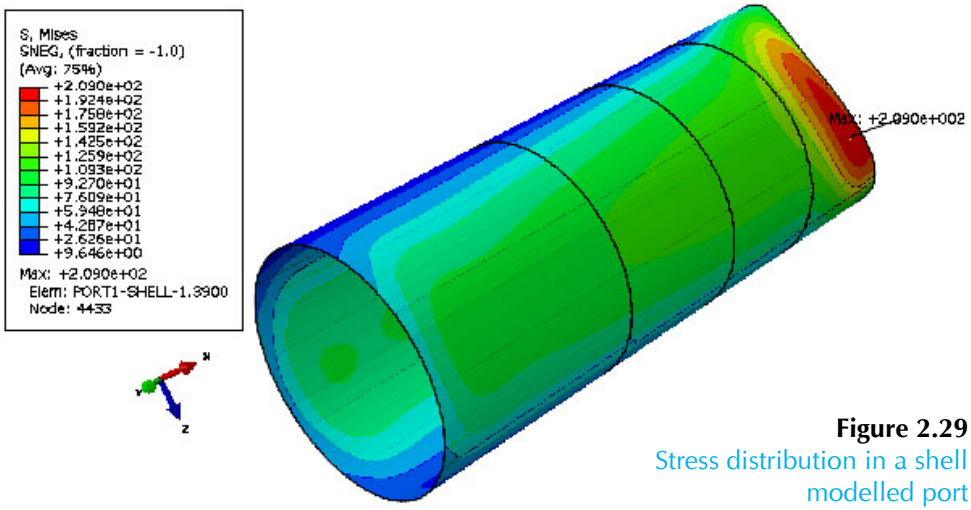

Figure 2.29
Stress distribution in a shell modelled port

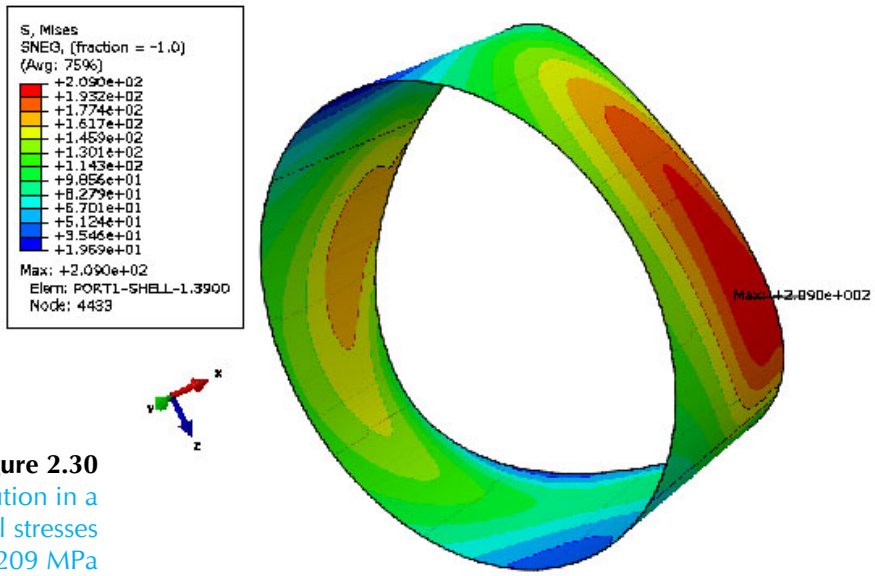

Figure 2.30
Close view of stress distribution in a shell modelled port, maximal stresses 209 MPa

Maximal stress level obtained in model is 581 MPa. These stresses are obtained on the boundary of the shell to solid coupling in the solid body of plasma vessel (Figure 2.31). Stress distribution in cross section of port in area of maximal stress 581 MPa is presented in Figure 2.32. The region of high stress was received only in surface on the boundary of shell to solid coupling in the solid body of plasma vessel. The stress level in the middle of this cross section reaches about 156 MPa.

Maximal obtained stress level in port is 495.9 MPa, on the boundary of the shell to solid coupling in the solid body of port (Figure 2.33). Stress distribution in cross section of port in area of maximal stress 495.9 MPa is presented in Figure 2.34. The obtained stress level is 445 MPa on the wall of port, close to the edge of weld tip (Figure 2.35). The region of high stress was received only in surface on the connection of port with weld. The stress level in the middle of this cross section reaches about 162 MPa.

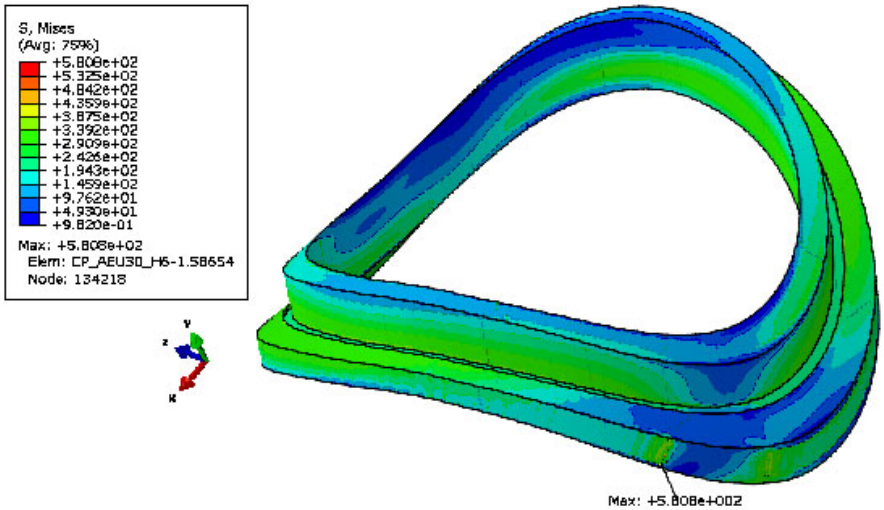

Figure 2.31
Stress distribution in central part with elements of maximal stress 580 MPa spot

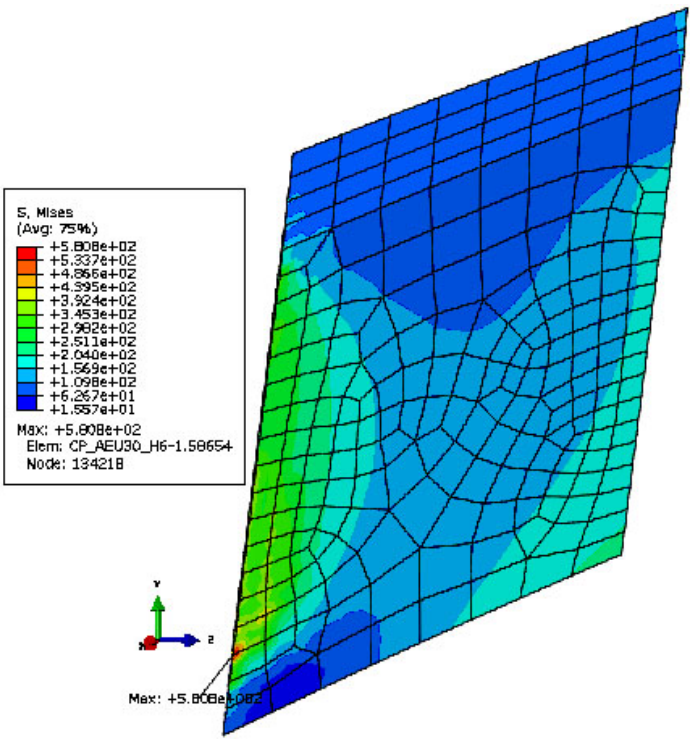

Figure 2.32
Stress distribution in PV cross section of maximal stress 580.8 MPa

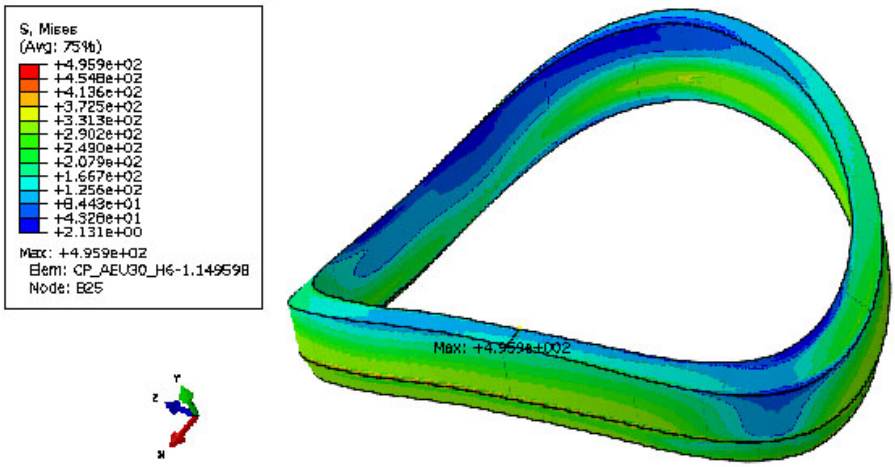

Figure 2.33
Stress distribution in a modelled solid port

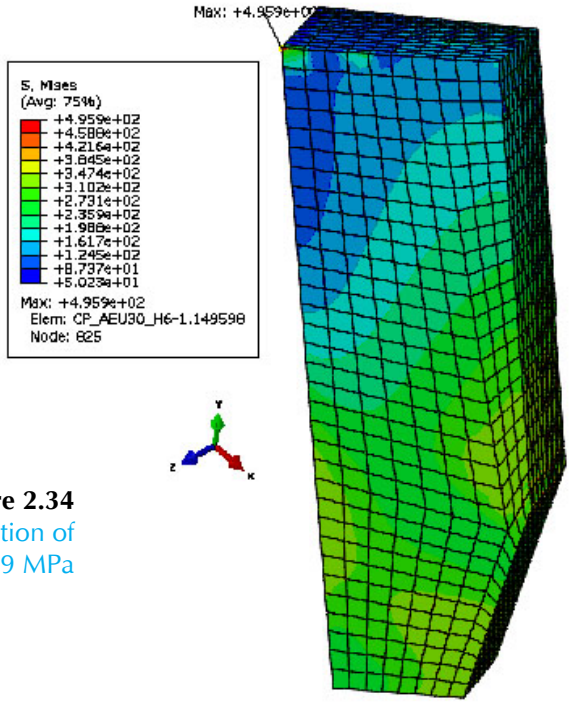

Figure 2.34
Stress distribution in port cross section of maximal stress 495.9 MPa

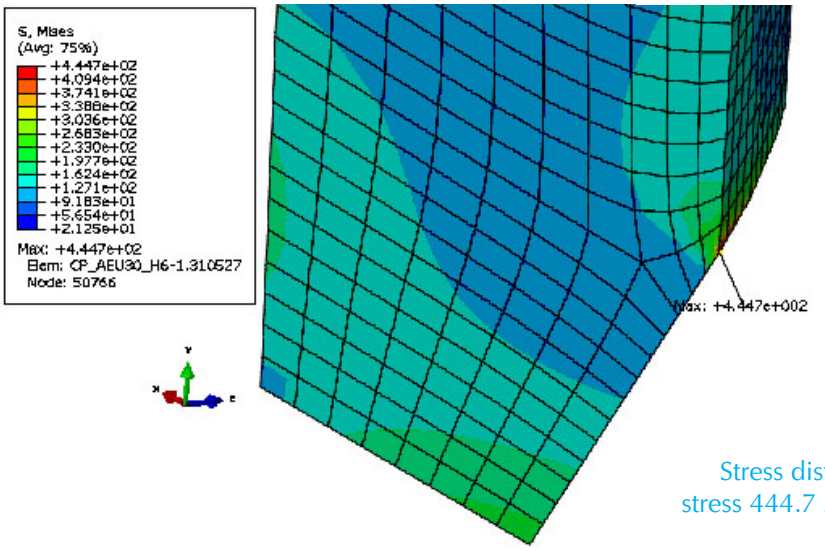

Figure 2.35
Stress distribution in a port cross section of stress 444.7 MPa at the port, close to the edge of weld tip

Main interest area of the welding connection between the port AEU30 and the PV shell is weld. In weld maximal stress is 279.8 MPa (Figure 2.36). The enlarged view of the stress distribution in weld is presented in Figure 2.37. Stress distribution in cross section of weld in area of maximal stress 279.8 MPa is presented in Figure 2.38, a. In this cross section along the surface of weld the line was drawn (Figure 2.38, b). The Von Mises stress history along path of this line of weld cross section is presented in Figure 2.39. The results show that the maximal value of stresses reaches 228.9 MPa. Mean value of stress along path of line of weld cross section is 188 MPa.

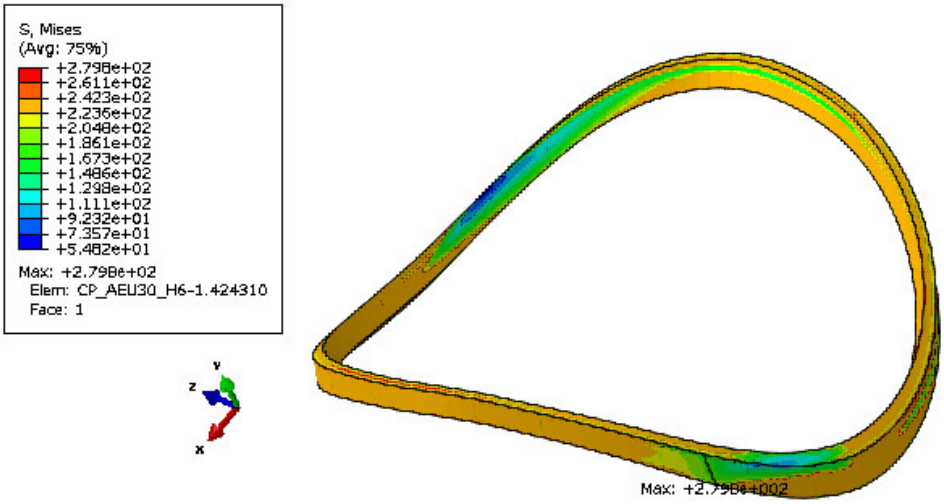

Figure 2.36
Stress distribution in modelled solid weld, maximal stresses 279 MPa

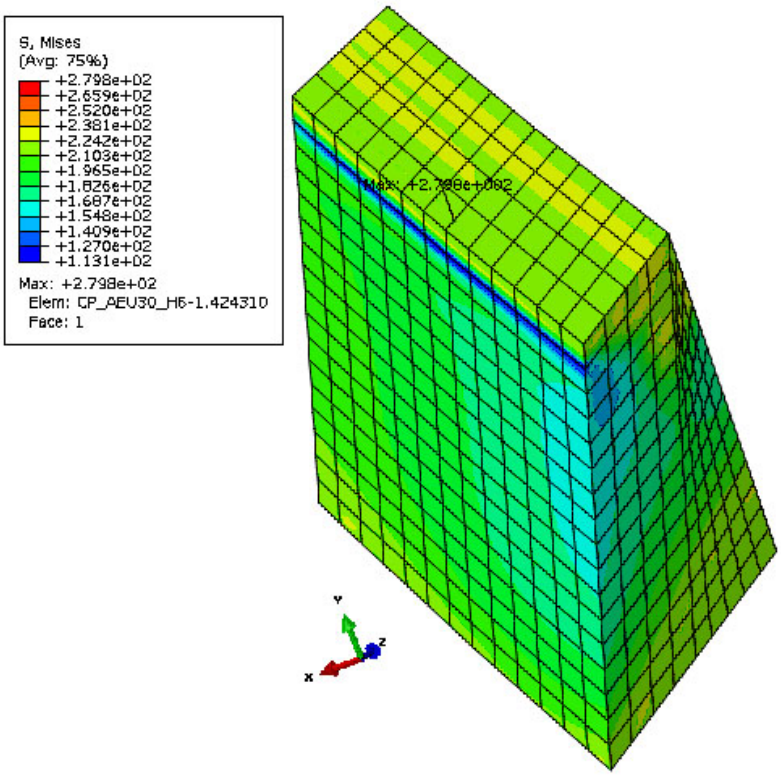

Figure 2.37
Close view of stress distribution in modelled solid weld, maximal stresses 279 MPa

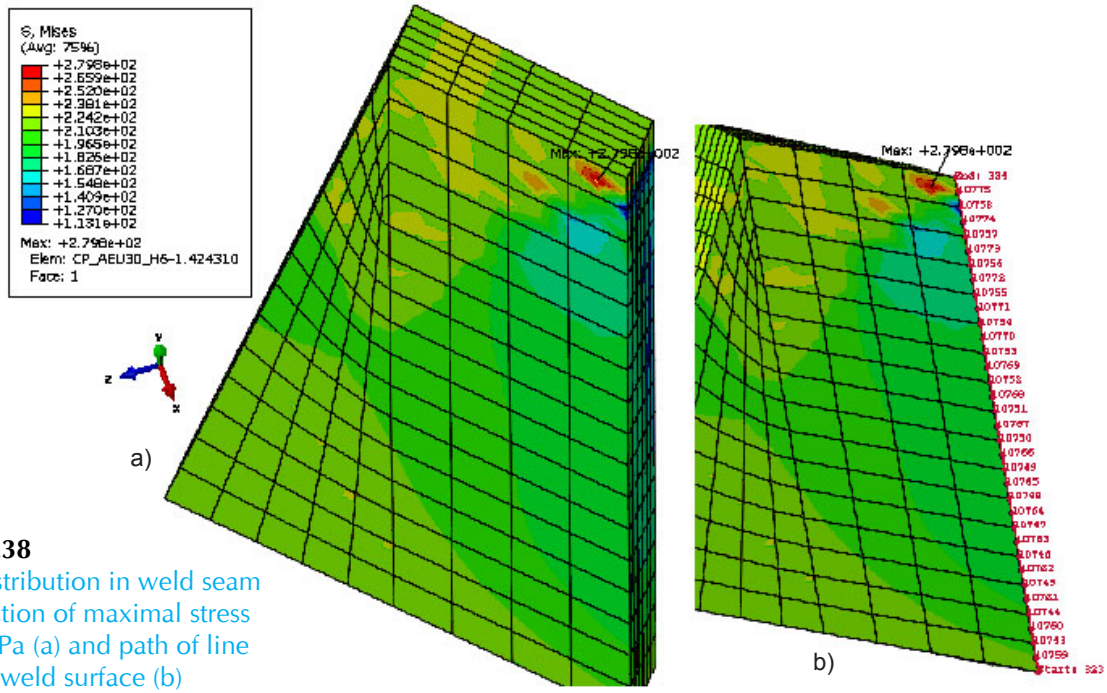

Figure 2.38
Stress distribution in weld seam cross section of maximal stress 279.8 MPa (a) and path of line along of weld surface (b)

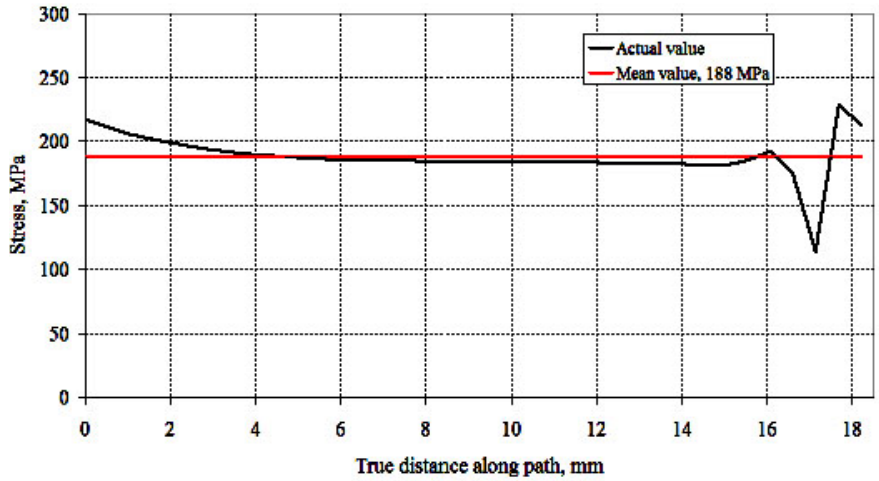

Figure 2.39
Total Misses stress history along path of line along of weld surface

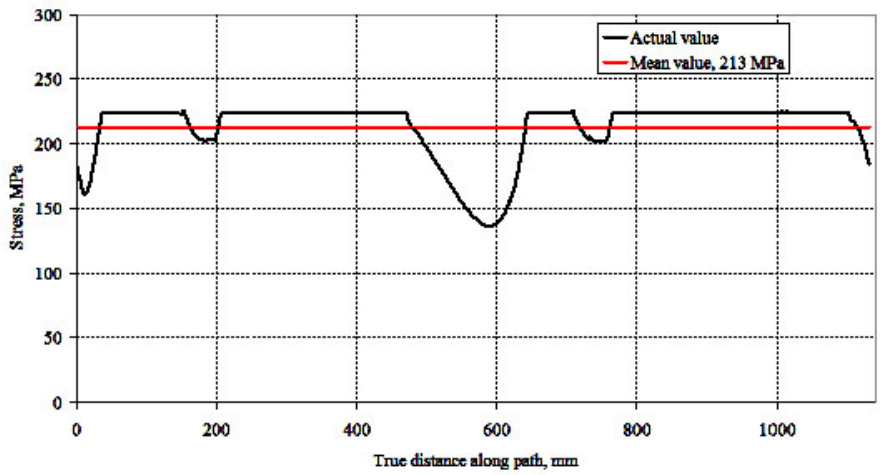

Figure 2.40
Von Misses stress histories along middle line of weld seam and PV

The Von Mises stress history along middle line of weld seam and PV (perimeter of the weld in outer surface) is presented in Figure 2.40. The results show that the mean value of stresses is 213 MPa. The results show that this mean value of stresses is exceed the primary general membrane stress (P_M = 149 MPa). The stress level 224 MPa was reached at long length of the weld (~800 mm). The Mises stress histories along middle line of weld seam and PV at different safety factors are presented in Figure 2.41. The Mises stress dependence from safety factor at peak value of stress is presented in Figure 2.42. The primary local membrane stress level was reached at safety factor 2.2. At this safety factor, the plastic deformation of weld will begin.

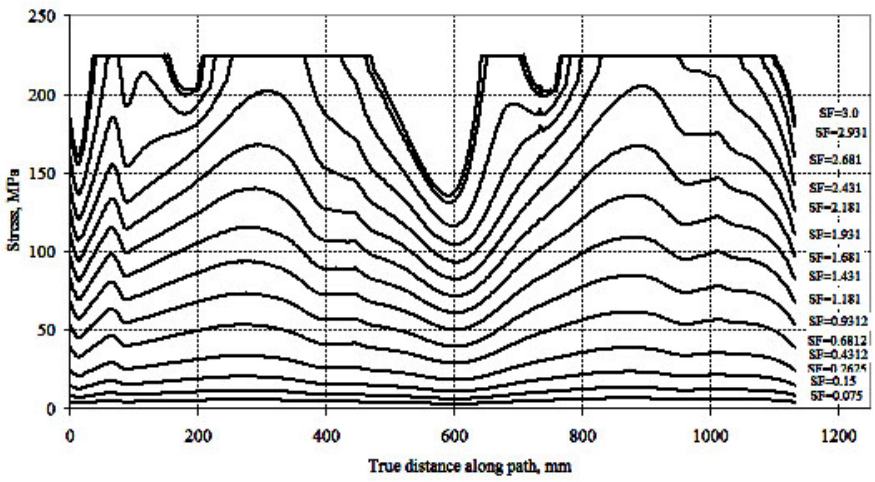

Figure 2.41
Von Misses stress histories along middle line of weld seam and PV at different safety factors

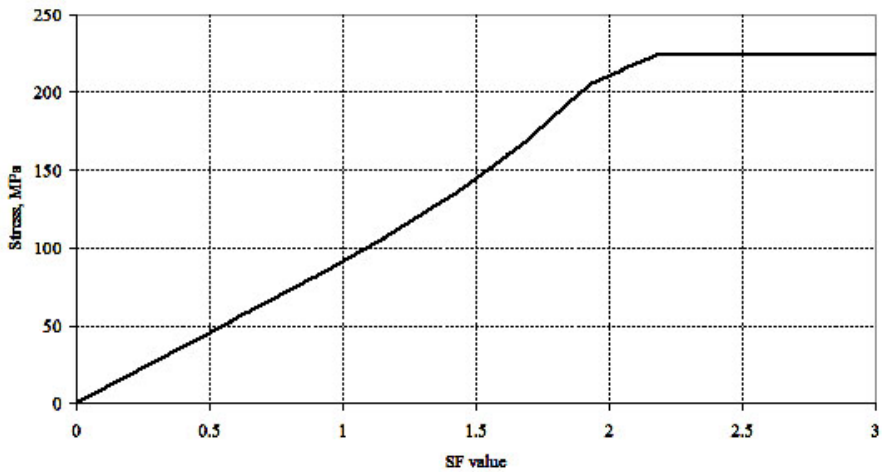

Figure 2.42
Von Misses stress dependence on the scale factor at peak value of stress in weld seam

The distribution of equivalent plastic strain at the port and PV around weld, and the weld are presented in Figure 2.43 – Figure 2.45. The plastic strain zones appeared in PV connected with the weld (Figure 2.43), in the port connected with weld (Figure 2.44) and at the top of the weld connected with the port and PV (Figure 2.45). The plastic strain zone areas in PV and the port are small, but in the weld this zone appeared through the cross section of the weld.

According to the stress and plastic strain results, it possible to maintain that plastic deformation will occur through cross section of weld.

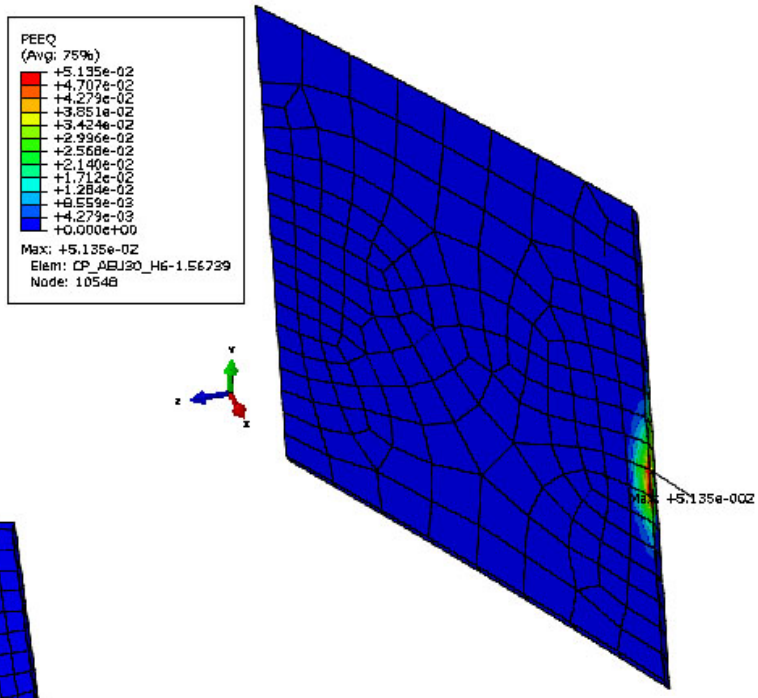

Figure 2.43
Close view of equivalent plastic strain at integration points of PV cross section at maximal value of equivalent plastic strain

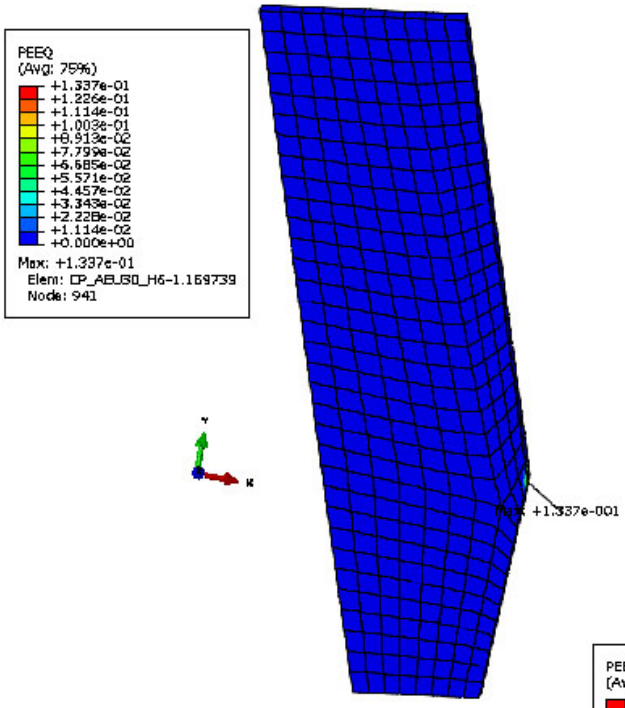

Figure 2.44
Close view of equivalent plastic strain at integration points of port cross section at maximal value of equivalent plastic strain

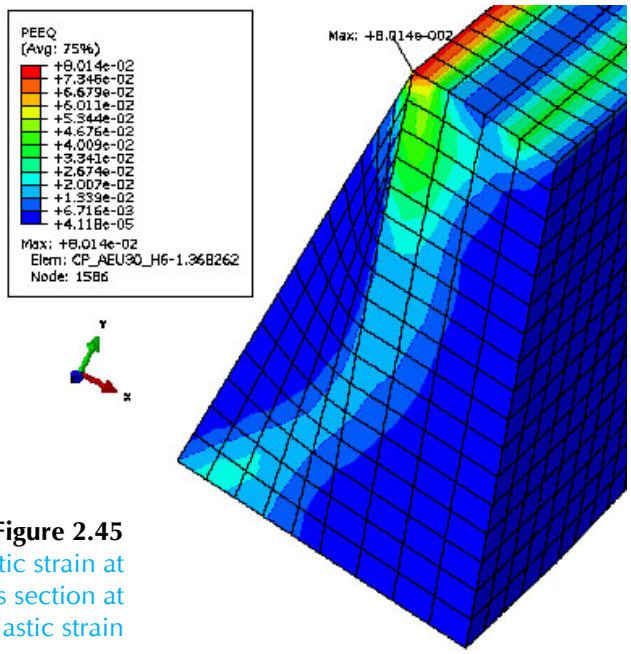

Figure 2.45
Close view of equivalent plastic strain at integration points of weld seam cross section at maximal value of equivalent plastic strain

2.8 Conclusions of structural integrity analysis

The structural integrity analysis of the welding connections was analysed of the following ports:

- Welding connection between the port AEQ20 and the PV shell with a 1 mm gap;
- Welding connection between the port AEU30 and the PV shell with 1 mm and 6 mm gaps;
- Welding connection between the port AEK20 and the PV shell with a 1 mm gap.

The geometrical 3D models of these port welds were prepared using the software SolidWorks. The finite element models of the welding connection between the port AEQ20, AEU30, AEK20 and the PV shell were prepared using computer code ABAQUS.

The stress and limit analysis of the welding connection between the port AEQ20, AEU30, AEK20 and the PV shell was performed for Load case 5. For these welds the weld efficiency factor values K_{weld} = 0.7 and K_{weld} = 0.85 were used.

According to stress analysis results, it was received that the stresses in port and vessel is below yield strength which is 320 MPa. The stresses in welded zone of port and PV in nodes of some elements exceed the yield strength (for weld material 272 MPa (K_{weld} = 0.85) and 224 MPa (K_{weld} = 0.7)), but mean value of stresses are below the yield strength. The influence of these elements to the stress condition of all structure is minor.

The limit analysis of the welding connection between the port AEQ20, AEU30, AEK20 and the PV shell was performed for Load case 5 applying scaling factor 3.

According to limit analysis results, the fact that displacement of the point where loads are applied starts to increase very rapidly was not detected. The convergence was never lost during the analysis and limit analysis safely reached the SF = 3.0. Therefore, it is possible to conclude that the limit analysis yielded positive results of the welding between Plasma Vessel and ports AEQ20 and AEK20 with a 1 mm gap, AEU30 with gaps 1 and 6 mm, at both cases of analysis, i.e. K_{weld} = 0.85 and K_{weld} = 0.7. Therefore, the stability of the welding between Plasma Vessel and ports AEQ20 and AEK20 with a 1 mm gap, AEU30 with 1 mm and 6 mm gaps will be sustained at used loading for analysis.

According to limit analysis results in port AEU30 with a 6 mm gap, the yielding of equivalent plastic strain appeared in case the weld efficiency factor values 0.85 and 0.7. The biggest displacement in port AEU30 appeared at AEU30 with a 6 mm gap in case the weld efficiency factor value 0.7.

3 W7-X PROBABILISTIC RISK ANALYSIS

In 2011 the risk analysis methods, usually applied for nuclear power plants, were applied to W7-X PSA. The methods are similar to ITER RAMI (Reliability, Availability, Maintainability, Inspectability) Analysis. The reliability model for one of the W7-X systems was developed for Divertor Target Cooling Circuit designated as ACK10. RiskSpectrum ® PSA Professional developed by Relcon Scandpower AB (Sweden) was used. The objectives of the performed analysis were to:

- Estimate reliability of ACK10 components;
- Identify the "weakest" components from reliability point of view;
- Provide recommendations for improving system reliability.

3.1 Estimation of Divertor cooling circuit ACK10 availability

The analysis is performed for the following ACK10 operation modes: 1) part load, 2) normal load, 3) full load, 4) standby and 5) vented Plasma Vessel. All events which make operation impossible or require stopping operation are identified and analyzed. Note that during the planned experiment time the availability should be close to 100 %.

The fault schedule was developed for ACK10 for identification of the system failure events (Table 3.1). This is a top-down approach starting from identification of the main system function failures and the faults causing these failures and further down to identification of the root causes. The analysis is performed for the shaded events.

Table 3.1. ACK10 Fault Schedule

System failure	Cause of the failure		
Insufficient cooling			
	low flow		
		pump failure	
			pump failure
			drive failure
			cooling
			power supply
			lubrication
		line blockage	
			valve closed
			filter plugged
			pipe/hose plugged
		flow in wrong direction	
			jumpers opened
			check valves opened
			drainage/probe lines open
		pipe break	
			LOCA
			interface LOCA

System failure	Cause of the failure		
Insufficient cooling			
	low pressure		
		see low flow	
		pressuriser LOP?	
	high temperature		
		insuff cooling from ECB10	
		BC operation	
Water ingress to target/vessel			
	Target LOCA		
		overpressure	
			exceeded pump work
			pressurizer overpressure
			return line blockage
		pipe/hose wear off	
	module LOCA		
		what happens in this case?	
Water electric conductance too high			
	Water quality decrease		
		Failure of water preparation	
		Failure of filtering	
		Impurity import from outside	
Earthing failure			

The next step is identification of the failure events and their qualitative analysis. For this purpose Fault Tree (FT) analysis and Failure Modes and Effect Analysis (FMEA) and methods were used together.

3.1.1 Fault Tree analysis

FT is a top-down approach, which allows identifying the very basic causes for the system failure. The lowest-level events identified are called basic events. The reasonable level of details of analysis is defined by the analyst. Basic events are marked by circles on the Fault Trees.

A scope of this analysis is limited to ACK10 equipment only, including hardware failures, spurious operation and human errors. No external supplies like electrical power, control, cooling water etc. are considered. Including such failures requires modelling of the corresponding power supply control, cooling etc. systems which could require sufficient time. Such modelling can be performed at the later stages.

The top-level Fault Tree is ACK10_EXP "ACK10 unavailable for experiment" (Figure 3.1). This FT consists of five failure modes connected by OR-gate which means that ANY of them may lead to the top event. Each of five failures is represented by its own Fault Tree:

- Loss of module cooling – FT ACK10_MOD_COOL;
- Direct flow of water from the cold to the hot pipeline. – FT DIR_FLOW;
- No cooling water in BR012 pipeline – FT BR012_NO_WATER;
- No water from Pumps AP002, AP003 – FT NO_PUMPS;
- No water from Heat Exchangers (HE) of ECB10 system – FT NO_HE.

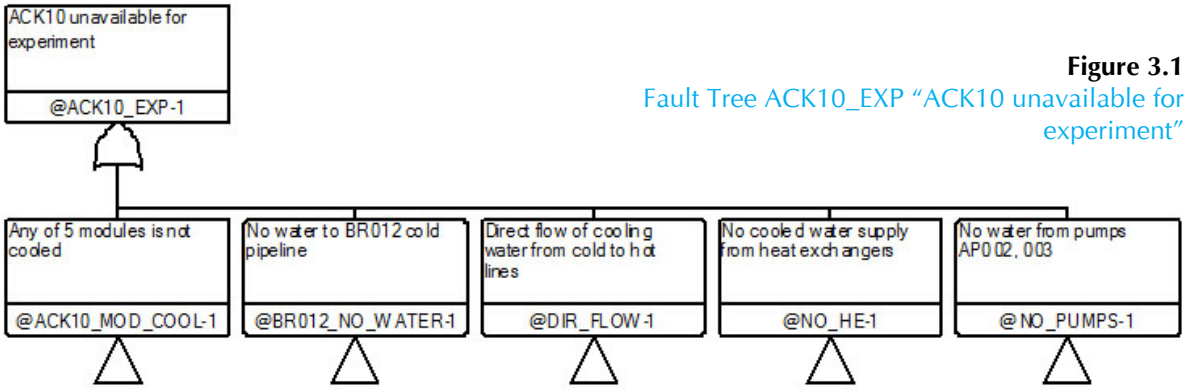

Figure 3.1
Fault Tree ACK10_EXP "ACK10 unavailable for experiment"

Loss of module cooling

ACK10 provides cooling of five target modules. Cooling water is supplied and heated water is discharged to the ring collectors located in the basement under the Torus Hall. Five pipelines provide cooling water from the cooling header provided to each module. Each supplying pipeline is equipped with pneumatic valve KA032,035,038,041,044. Heated water is discharged from the modules to five pipelines which are connected to the ring header. Each discharge pipeline is equipped with check valve KA033,036,039,042,045 and manual valve KA034,037,040,043,046. Failure of cooling of any of five modules requires stopping plasma operation (Figure 3.2).

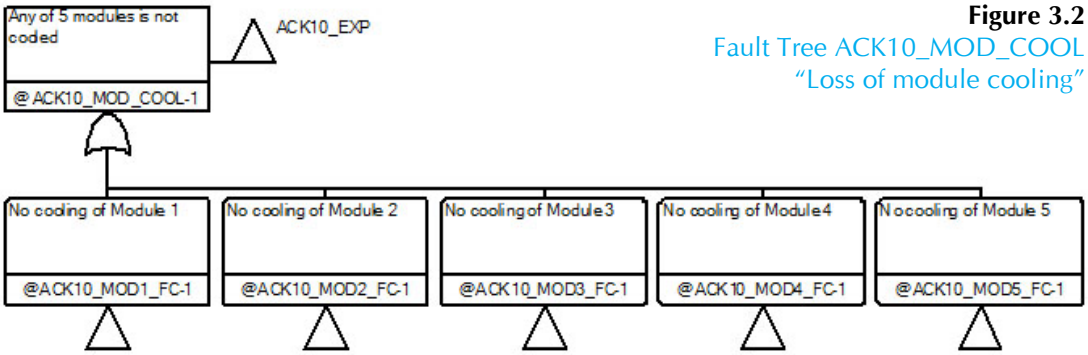

Figure 3.2
Fault Tree ACK10_MOD_COOL "Loss of module cooling"

Failure of module cooling may be caused by closure of any pneumatic valve. Valve closure, in turn, may be caused by valve closed position in the beginning of operation (e.g. forgot to open after maintenance) or spurious (unintended) closure caused by human error or by control mistake (for remotely operated pneumatic valves only). The modelling of such failures for Target Module 1 is shown in Figure 3.3. The Fault Trees for other modules are identical.

Direct connection between cold and hot water pipelines

This failure is represented by the developed Fault Tree shown in Figure 3.4. System ACK10 contains pipelines that connect cold water pipeline BR012 and the baking circuit. The pipelines are equipped with pneumatic valve KA103 and pneumatic regulating valves KA001,002,003. The purpose of these lines is to provide and regulate cold water flow to the baking circuit for "baking" mode operation. These valves are opened only for "baking" mode and are closed in all other operation modes. Opening of these valves during plasma operation would lead to loss of pressure difference between cold and hot pipelines and, as a consequence, to loss of module cooling. Valve opening may be either "left open" or "spurious opening".

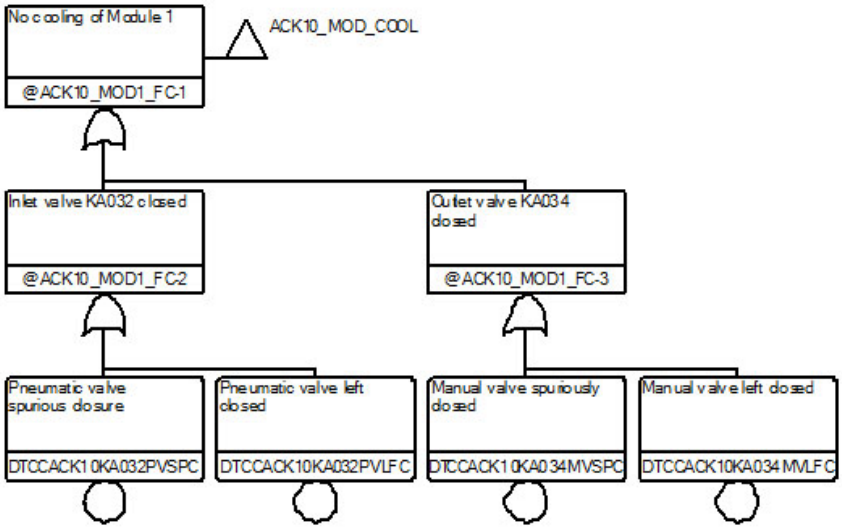

Figure 3.3
Fault Tree ACK10_MOD1_FC "Loss of Module 1 cooling"

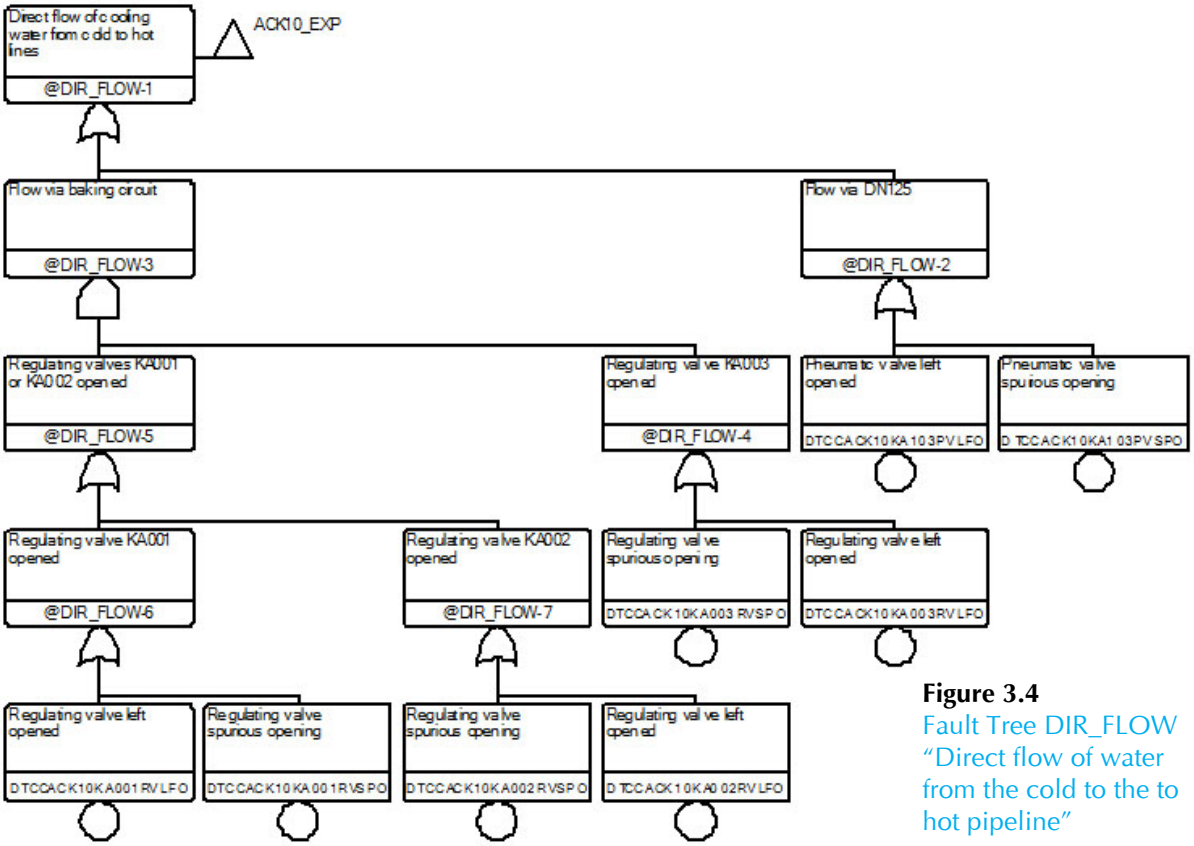

Figure 3.4
Fault Tree DIR_FLOW "Direct flow of water from the cold to the to hot pipeline"

No cooling water in cold pipeline BR012

This failure is represented by the developed Fault Tree shown in Figure 3.5. Pipeline BR012 (DN600) supplies cold water from pumps to target cooling ring header. Water from the pumps to BR012 is provided by DN600 pipeline BR011 which is equipped with (by flow direction) manual valve KA512, filter AT801 and manual valve KA513. The valves are normally opened and are closed only for maintenance and filter repair. This pipeline also has DN40 bypass cleaning circuit

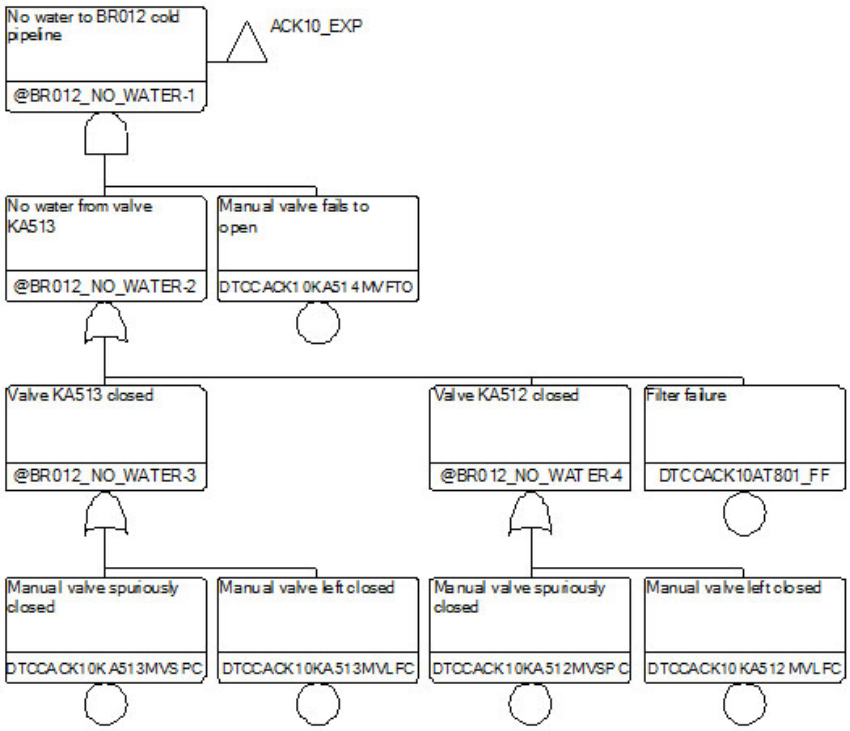

Figure 3.5
Fault Tree BR012_NO_WATER "No cooling water in BR012 pipeline"

equipped with ball valve KA515, Filter AT804, mesh filter AT802 and ball valve KA516. There is another DN600 pipeline parallel to BR011 with normally closed manual valve KA514.

Failure to provide water to BR012 may be caused by blockage of BR011 and failure to open valve KA514. Blockage of BR011 may be caused by closure of either KA512 or KA513 or by failure of filter AT801. Failure of the filter does not mean only complete plugging of the filter but any kind of filter failure, which would require its repair and closure of manual valves. Bypass filtering line cannot be considered as a reserve water supply line due to its small diameter.

No water from Pumps AP002, AP003

This failure is represented by the developed Fault Tree shown in Figure 3.6. Cooling water circulation in ACK10 system is ensured by pumps AP001, AP002, AP003. Two pumps are required to provide sufficient cooling for Normal Load and Full Load operation modes. Only one pump AP003 is installed now and AP002 is planned to be installed. Installation of AP001 is under consideration, and it is possible that this pump will not be installed and only two pumps will be in operation. Each pump line is equipped with:

- manual gate valve KA505(504) is normally open and is closed only for pump maintenance;
- pump AP003(002) may be in operation or in standby;
- check valve KA508(507) is opened when the pump is running and closes due to the pressure difference when the pump stops;
- pneumatic valve KA510(511) is opened when the pump is running and closes due to the automatic signal when the pump stops.

It is planned that most of the time, ACK10 system will be in Part Load and Standby modes, which correspond to pauses between W7-X experiments and non-working time correspondingly. Cooling water flow rates for these modes are 425 m^3/h and 177 m^3/h, respectively. Such flow rate may be ensured by one pump, which is assumed to be in operation all the time.

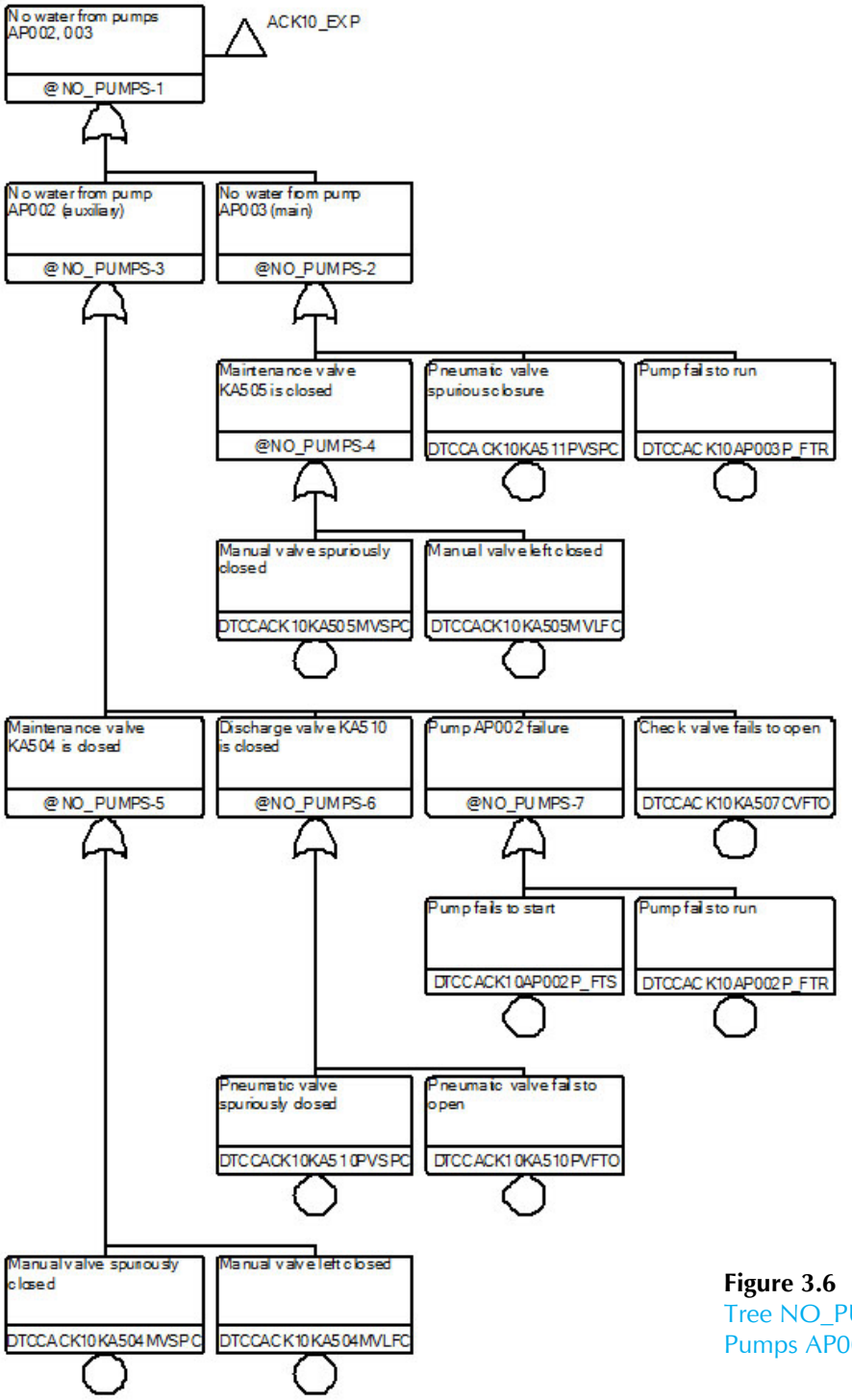

Figure 3.6
Tree NO_PUMPS "No water from Pumps AP002, AP003"

The second pump is started only when an additional flow up to 1382 m^3/h for Normal Load and 1602 m^3/h for Full Load is required. This determines the failure modes of the system. It is assumed that AP003 is the main running pump and AP002 is auxiliary. Therefore, the failure modes for AP003 are:

- Manual gate valve KA505 is erroneously closed or spuriously closes;
- Pump fails to run;
- Pneumatic valve KA511 is erroneously closed or spuriously closes.

The failure modes for AP002 are:

- Manual gate valve KA504 is erroneously closed or spuriously closes;
- Pump fails to start or fails to run;
- Check valve KA507 fails to open at pump startup;

Pneumatic valve KA510 fails to open at pump startup or is erroneously closed or spuriously closes.

No water from Heat Exchangers of ECB10 system

This failure is represented by the developed Fault Tree shown in Figure 3.7. ACK10 primary circuit water cooling is ensured by secondary circuit ECB10. The cooling is provided by two heat exchangers (HE) 1ECB10AD001 and AD002. The cooling requirements are 10 MW for Normal Load and Full Load, 2 MW for Part Load. Cooling capacity of each HE is 5MW, i.e. two HE are

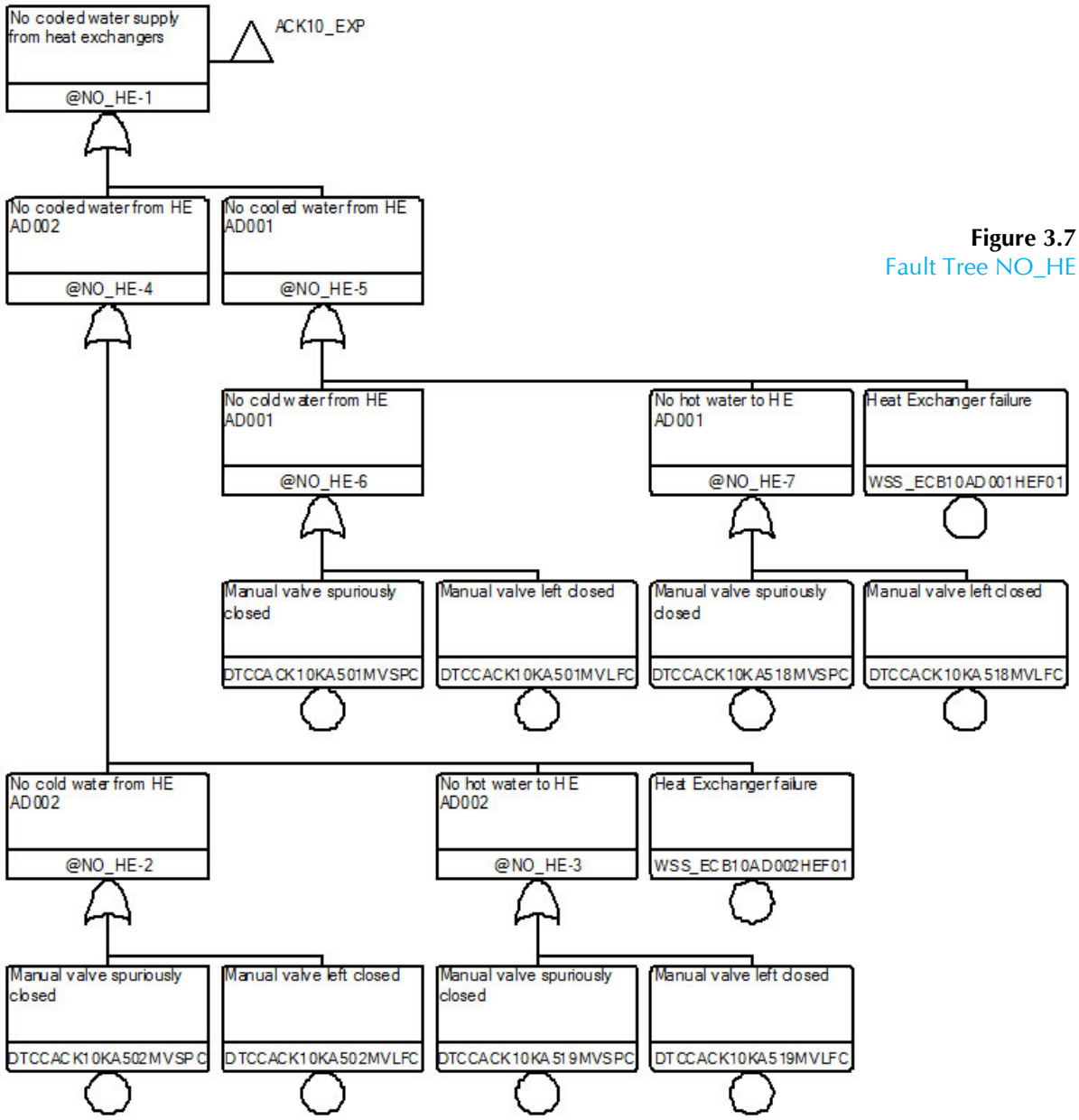

Figure 3.7
Fault Tree NO_HE

required for NL and FL. Each HE is equipped with manual gate valves KA518(519) on the heated water inlet and KA501(502) on the cooled water outlet lines.

The failure modes for loss of water cooling by each ECB10 HE are:

- Manual gate valve is closed (either inlet or outlet);
- Loss of HE cooling capacity.

This is a general failure mode without going into details. The reasons for such failure could be: HE plugging, leakage, loss of secondary cooling water etc. Loss of ECB10 cooling circuit was not modelled as such modelling is out of the scope at this analysis stage.

3.1.2 Failure Modes and Effects Analysis (FMEA)

FMEA is bottom-up approach identifying each possible failure mode for each component. It is used in the current analysis in addition to the FT analysis to identify the failure modes, their causes, repair actions and preventive measures for each basic event identified by FT analysis. In order to estimate unavailability for each basic event, several parameters should be identified:

- time when the failure may appear (normal operation, standby, maintenance etc.),
- possible causes (equipment failure, human error, etc.),
- signs that help detecting the failure,
- period and time when the failure may be identified,
- correction measures required (just opening the valve or complete replacement of the failed piece).

3.1.3 Development of unavailability models

RiskSpectrum® allows choosing among the several reliability models for each basic event. A "Monitored repairable component" unavailability model was used for all components and failure modes. This model allows accounting for both failure rate and repair rate. The long-term unavailability for such model is equal to:

$Q = \lambda/(\lambda + \mu)$, where λ – failure rate, μ – repair rate = 1/TR – repair time.

Generic failure rates were used at this stage. The failure rates are given in Table 3.2. Note that ACK10 is already in testing operation. Therefore, keeping records of equipment failure statistics would allow estimation of reliability parameters specific for ACK10. The same is true for other W7-X systems.

The failure rates provided are averaged values which for the purpose of ACK10 analysis were recalculated in accordance with equipment operation regimes as described below.

Failure rates for cooling pump

It was assumed that cooling pumps are operated asymmetrically, i.e. one pump AP003 is operating during all operating modes that require target cooling, namely WSB, WBL, PL, NL, FL, and the second pump AP002 is started up only for experiments (operation modes NL, FL). The main pump is started up only twice per year after W7-X outages and operates 6862 hours per year. Therefore, the main failure mode for this pump is failure to run. Failure rate for the main pump remains unchanged 3E-5 1/hour.

Table 3.2 Generic reliability data

Name	*Failure rate*	*Unit*	*Distribution*	*Error factor*
Pump fails to run	3.00E-05	1/hour	Lognormal	10
Pump fails to start	3.00E-03	1/demand	Lognormal	10
Check valve fails to open	1.00E-04	1/demand	Lognormal	3
Pneumatic valve fails to open	2.00E-03	1/demand	Lognormal	3
Pneumatic valve spurious closure	1.00E-07	1/hour	Lognormal	3
Filter failure	2.00E-06	1/hour	None	–
Regulating valve spurious opening	5.00E-07	1/hour	Lognormal	10
Pneumatic valve spurious opening	5.00E-07	1/hour	Lognormal	10
Manual valve fails to open	1.00E-04	1/demand	Lognormal	3
Heat Exchanger failure	9.00E-06	1/hour	Lognormal	10
Pneumatic valve left closed	3.00E-03	1/demand	Lognormal	10
Manual valve spuriously closed	3.00E-03	1/year	Lognormal	3
Regulating valve left opened	3.00E-03	1/demand	Lognormal	10

The auxiliary pump operates only 136 h/year and its average "failure to run" rate per operating year is, therefore:

*3e-5 failures/hour * 136 h/year / 6526 operating h/year = 6.25E-07*

But this pump has 320 startup demands per year:

*2 demands/day * 5 days/week * 16 weeks/campaign * 2 campaigns/year = 320 demands/year.*

A failure rate per demand is therefore recalculated to the "failure to start" rate per year:

*320 demands/year * 3.00E-03 failures/demand / 6526 hours/year = 1.47E-4 failure/per hour.*

This is rather high failure rate and it is due to a high number of start/stop cycles.

A repair time for failed pump was chosen 720 hours (1 month) as it was conservatively assumed that no repair is available on site and the failed pump shall be send to the manufacturer for repair

Failure rates for valve failure to open

There are the following "valve failure to open" basic events in the model.

Pneumatic valve KA510 and check valve KA507, both on the pressure line of the auxiliary pump AP002. These valves close every time when the pump stops. The pneumatic valve is closed automatically by control algorithm, the check valve closes due to pressure decrease. Similarly to the pump, these valves are under high cyclic loads – 320 open/close cycles per year. The failure rates for the valves were recalculated from "failure per demand" to "failure per hour" in the same way as for the pumps:

For the pneumatic valve:

*320 demands/year * 2.00E-03 failures/demand / 6526 hours/year = 9.81E-5 failure/per hour.*

For the check valve:

*320 demands/year * 1.00E-04 failures/demand / 6526 hours/year = 4.90E-6 failure/per hour.*

Manual valve KA514 needs to be open only when pipe BR011 is blocked due to valve closure or filter repair. For this valve failure rate per demand 1.E-4 remains unchanged.

Repair time for the valves is conservatively assumed 720 hours as it is assumed that no spares are available and the necessary spares should be procured and delivered on site.

Failure rates for filter and heat exchangers

Failure rates for filter and heat exchangers remain the same and cover all failure modes like plugging, leakage etc. The repair time is also assumed 720 hours.

Human induced failures

Human errors have a big influence on equipment unavailability. ACK10 model contains several events which are caused by human errors, namely valves left in wrong position after maintenance and repair. Detailed human reliability analysis (HRA) requires thorough review of repair and maintenance procedures, practice, equipment location and other factors which impact human performance and may increase or decrease error probability.

At the initial stages of analysis a simplified approach is used. The same human error probability of 3E-3 is applied for each event multiplied by a number of occurrence possibilities, which is assumed the same for all valves and is equal to 2 (after each outage twice per year).

Failure rate due to human error is estimated as:

*3E-3 failure/action * 2 actions/year / 6526 hours/year = 9.19E-7 failure/hour.*

The repair time is a time required for opening closed valves. The time was estimated conservatively to be 24 hours and include a time to diagnose the situation, identify and open the closed valve and restart both the ACK10 system and W7-X operation.

Valve failure during operation

Failures may be expected even for valves which stay open or close and do not change the position during all operation time. Such valve may open/close spuriously due to control logic failure or human error, they may lose operation control or power supply and therefore need to be repaired or replaced. Many such failure modes with very low and uncertain failure rates may be defined. E.g. spurious opening/closure of valves itself has rather low rate about 5E-7 1/h. In this analysis, it was assumed that the main reason for the valve failure is spurious operation caused by human error and the same failure rates and repair time as for human induced failures are used.

3.1.4 Model calculation

The model quantification includes generation of Minimal Cut Sets (MCS), uncertainty and sensitivity analysis. The calculation was performed for time period of 6526 hours, i.e. total time of operation campaigns per year.

The Minimal Cut Sets (MCS) are generated as a result of the Fault Tree analysis. MCS is a set of basic events which, if occurred, definitely lead to the top event, i.e. to unavailability of ACK10. The MCS are generated using PSA software.

Calculated total unavailability for ACK10 operation period in a year is 0.188. This means that the system could be unavailable for operation 18.8% of operation campaign. As a result of ACK10 model analysis 56 Minimal Cut Sets were generated and top 7 MCS are presented in Table 3.3. The remaining MCS bring only 0.01% to the total unavailability. The results show that due to low system redundancy, the failure of a single component could lead to complete system unavailability. More than 50 % influence to the system unavailability brings the failure of auxiliary (secondary) cooling pump AP002, which has a high number of cyclic loads. About 35 % brings pneumatic valve KA510 located at the pressure line of the same pump. This valve is also a subject to high cyclic loads.

Table 3.3 Operation time for each ACK10 operation modes

No	*Probability*	*%*	*Event Code*	*Event Name*
1	9.57E-02	51	DTCCACK10AP002P_FTS	Pump AP002 fails to start
2	6.60E-02	35.1	DTCCACK10KA510PVFTO	Pneumatic valve KA510 Fails to open
3	2.11E-02	11.3	DTCCACK10AP003P_FTR	Pump AP003 fails to run
4	6.44E-03	3.43	WSS_ECB10AD002HEF01	Heat Exchanger AD002 fails
5	6.44E-03	3.43	WSS_ECB10AD001HEF01	Heat Exchanger AD001 fails
6	3.52E-03	1.87	DTCCACK10KA507CVFTO	Check valve KA507 Fails to open
7	4.50E-04	0.24	DTCCACK10AP002P_FTR	Pump AP002 fails to run

In order to better understand the influence of each component and each parameter on the total unavailability the importance and sensitivity analyses were performed. The importance measures are:

The Fussell-Vesely (FV) importance for a basic event is the ratio between the unavailability based only on all MCSs where the basic event *i* is included and the nominal top event unavailability:

$$I^{FV}{}_i = \frac{Q_{TOP}(MCS_{including}i)}{Q_{TOP}},$$

where I^{FV}_i – FV importance; Q_{TOP} – nominal top event unavailability; $Q_{TOP}(MCS_{including}i)$ – unavailability based only on MCSs, where the basic event *i* is included.

The risk decrease factor (RDF) calculated as

$$I^{D}{}_i = \frac{Q_{TOP}}{Q_{TOP}(Q_i = 0)},$$

where I^{D}_i – RDF; $Q_{TOP}(Q_i = 0)$ – top event unavailability, where unavailability of the basic event *i* is set to zero.

The risk increase factor (RIF) calculated as

$$I^{I}{}_i = \frac{Q_{TOP}(Q_i = 1)}{Q_{TOP}},$$

where I^{I}_i – RIF; $Q_{TOP}(Q_i = 1)$ – top event unavailability, where unavailability of the basic event *i* is set to one.

The fractional contribution (FC) calculated as

$$I^{F}{}_i = 1 - \frac{1}{I^{D}{}_i}.$$

The sensitivity *S* is calculated as

$$S = \frac{Q_{TOP,U}}{Q_{TOP,L}},$$

where $Q_{TOP,U}$ – top event results, where unavailability of the basic event *i* is multiplied by a sensitivity factor (normally equal to 10); $Q_{TOP,L}$ – top event results where unavailability of the basic event *i* is divided by the sensitivity factor.

Top 7 Basic Events are presented in Table 3.4. It is obvious that the most important basic events

are the same as in the Minimal Cut Sets. The interesting outcome is that sensitivity measures show how total unavailability would change if reliability of each component changes. Such, Risk Decrease Factor (RDF) shows that assuming "perfect" pumps with failure probability equal to 0 would decrease ACK10 unavailability 1.84 times and Sens Low shows that increasing pump reliability 10 times, ACK10 unavailability would be 11% instead of current 18.4%.

Table 3.4 Basic Events Importance and sensitivity analysis results

No	*ID*	*Normal value*	*FV*	*FC*	*RDF*	*RIF*	*Sens*	*Sens high*	*Sens low*
1	DTCCACK10AP002P_FTS	9.57E-02	5.10E-01	4.58E-01	1.84E+00	5.33E+00	8.71E+00	9.61E-01	1.10E-01
2	DTCCACK10KA510PVFTO	6.60E-02	3.51E-01	3.06E-01	1.44E+00	5.33E+00	5.17E+00	7.04E-01	1.36E-01
3	DTCCACK10AP003P_FTR	2.11E-02	1.13E-01	9.35E-02	1.10E+00	5.33E+00	2.01E+00	3.46E-01	1.72E-01
4	WSS_ECB10AD001HEF01	6.44E-03	3.43E-02	2.80E-02	1.03E+00	5.33E+00	1.28E+00	2.35E-01	1.83E-01
5	WSS_ECB10AD002HEF01	6.44E-03	3.43E-02	2.80E-02	1.03E+00	5.33E+00	1.28E+00	2.35E-01	1.83E-01
6	DTCCACK10KA507CVFTO	3.52E-03	1.87E-02	1.53E-02	1.02E+00	5.33E+00	1.15E+00	2.14E-01	1.85E-01
7	DTCCACK10AP002P_FTR	4.50E-04	2.40E-03	1.95E-03	1.00E+00	5.33E+00	1.02E+00	1.91E-01	1.87E-01

The results of importance and sensitivity analyses for parameters are presented in Table 3.5. The results show that the most important parameter is not equipment reliability, but one month for hardware repair or replacement, which was assumed (parameter ONE_MONTH). Sens.Low shows that decreasing this time 10 times would result in ACK10 unavailability only 2.2%. The next important parameter is pump standby failure rate (parameter PUMP_STBY), which is used for pump AP002 and improvement 10 times of which would change ACK10 unavailability from 18.8% to 11.1%. Other parameters can be interpreted in the same way.

Table 3.5 Basic Events Importance and sensitivity analysis results

No	*ID*	*Type*	*Normal value*	*FC*	*RDF*	*RIF*	*Sens*	*Sens high*	*Sens low*
1	ONE MONTH	Tr	7.20E+02	9.96E-01	2.37E+02	5.33E+00	3.65E+01	8.02E-01	2.20E-02
2	PUMP_STB	r	1.47E-04	4.58E-01	1.84E+00	5.33E+00	5.07E+00	5.64E-01	1.11E-01
3	PV_FTO	r	9.81E-05	3.06E-01	1.44E+00	5.33E+00	3.59E+00	4.90E-01	1.36E-01
4	PUMP_FTR	r	3.00E-05	9.35E-02	1.10E+00	5.33E+00	1.85E+00	3.18E-01	1.72E-01
5	HE_FAIL	r	9.00E-06	5.63E-02	1.06E+00	5.33E+00	1.54E+00	2.74E-01	1.78E-01
6	CV_FTO	r	4.90E-06	1.53E-02	1.02E+00	5.33E+00	1.15E+00	2.13E-01	1.85E-01
7	ONE_DAY	Tr	2.40E+01	3.44E-03	1.00E+00	5.33E+00	1.03E+00	1.94E-01	1.87E-01
8	MV_SPC	r	9.19E-07	2.10E-03	1.00E+00	5.33E+00	1.02E+00	1.91E-01	1.87E-01
9	PUMP_A_FTR	r	6.25E-07	1.95E-03	1.00E+00	5.33E+00	1.02E+00	1.91E-01	1.87E-01
10	PV_SPC	r	9.19E-07	1.15E-03	1.00E+00	5.33E+00	1.01E+00	1.90E-01	1.88E-01
11	PV_SPO	r	9.19E-07	1.91E-04	1.00E+00	5.33E+00	1.00E+00	1.88E-01	1.88E-01
12	MV_FTO	q	1.00E-04	6.60E-07	1.00E+00	1.01E+00	1.00E+00	1.88E-01	1.88E-01
13	FILTER_FAIL	r	2.00E-06	6.22E-07	1.00E+00	1.00E+00	1.00E+00	1.88E-01	1.88E-01

Considering made assumptions the received results could be rather conservative. A more detailed analysis would provide a more realistic picture. The presented results are the first step for such work indicating the areas where such analysis should be concentrated.

3.1.5 Conclusions on ACK10 availability

1. Unavailability of the ACK10 is 18.8% of the operational campaign, i.e. about 1.5 month of 8 month operation in a year the system would be unavailable, thus experiments at W7-X could not be performed.
2. The main impact to unavailability is an operation regime of the cooling pumps where one pump is always running to provide cooling during all operation modes and the second one is started only to provide additional cooling for plasma operation. This causes high cyclic load and corresponding high failure probability to the secondary pump (unavailability 95.7% which is almost certainly once per year) and its regulating valve (unavailability 66%, i.e. twice in three years). These components bring correspondingly 51% and 35% to the total unavailability.
3. The second major reason for unavailability is long repair time which is assumed one month accounting for the time required to deliver and repair the equipment at the manufacturer's site or to procure the spares required for the repair.
4. Limited redundancy of the equipment does not allow continuing operation while the components are being repaired.

3.2 Evaluation of ACK10 availability increase measures

In previous section, it was identified that the main impact to unavailability of Divertor cooling circuit ACK10 is the operation mode of the cooling pumps, where the second pump is started only to provide additional cooling for plasma experiments. This causes high cyclic load and corresponding high failure probability to the secondary pump. This component brings 51 % to the total unavailability of ACK10. This section provides analysis of different options to increase availability of ACK10 pumps.

3.2.1 Evaluation method

The purpose of risk analysis is to provide support in making correct management decisions by evaluating the risk associated with a set of decision alternatives. Classical definition of the risk of failure is $K = p_f C$, where K is the risk of failure, p_f is the probability of failure, and C is the cost caused by the failure. The measure of the cost may be different. For production plants it is usually not only the cost of repair itself but also an amount of lost production and lost profit. The risk of failure can be represented by a diagram (Figure 3.8). The C-axis of the diagram represents the loss given failure while the p_f -axis represents the probability of failure. The solid lines represent risk levels K equal to 1, 10, 50, ... , 900 units.

The Risk could be reduced either by reducing the loss given failure or by reducing the probability of failure or by reducing both. The risk reduction could be expressed as

$$\Delta K = K - K' = p_f C - (p_f - \Delta p_f)(C - \Delta C) = \Delta p_f C + \Delta C p_f - \Delta p_f \Delta C.$$

From the other hand, such risk reduction measures require some investments and should be taken into account during the analysis. The values Δp_f and ΔC should be selected in such a way that the risk reduction ΔK is achieved at minimal cost.

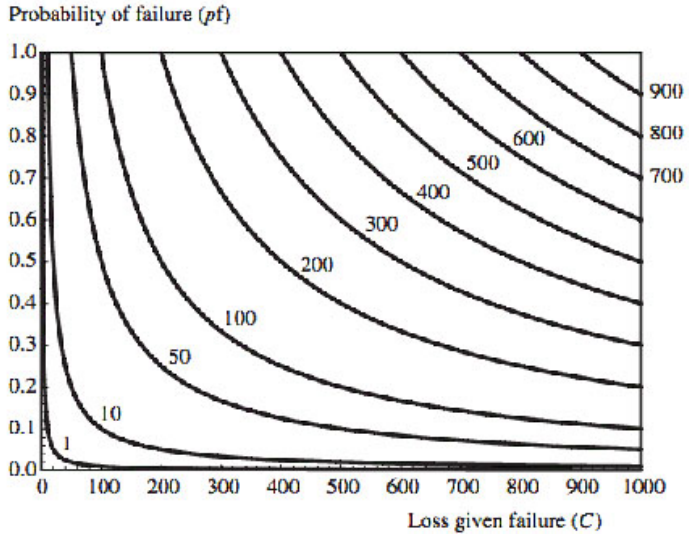

Figure 3.8
Representation of the 3D diagram related to the risk of failure

3.2.2 Evaluation of possible alternatives

In previous section, it was defined that one ACK10 pump is constantly operating and the second pump is auxiliary, which is started only during plasma operation when additional water flow is required for cooling. A high number of start/stop cycles of the pump and open/close cycles of pneumatic valve lead to high failure rate of the auxiliary pump line. Failure of auxiliary pump leads to inability to provide sufficient cooling of target modules and, as a result, inability to perform experiments. This means that until operation of the failed pump line is restored, the complete W7-X is inoperable and all related experiments and investigations are delayed to the corresponding amount of time.

Although W7-X is not for profit production, the cost of W7-X downtime can be estimated on a basis of a daily cost of W7-X operation. Indeed, when W7-X is inoperable, the entire facility and personnel cannot perform their main task (experiments, research) while the operational costs (personnel salary, infrastructure, resources etc.) remain the same.

The cost of W7-X downtime due to a failure may be interpreted as the inoperable time (or downtime) T_d caused by the failure multiplied by cost of time unit C_t (hour, day) and the risk may be rewritten as $K = p_f T_d C_t$. Reduction of the risk may be achieved by reduction of any of these three variables: probability of failure, downtime and cost of downtime. Further, several options to reduce the risk related to failure of the ACK10 pumps are considered.

Changing Pump operating modes

Currently, pump AP003 is assumed as the main one and AP002 as the auxiliary. Exchanging the operational role of the pumps periodically may reduce cyclic loads on auxiliary pump.

For both pumps two failure modes are modelled: "failure to start", which is dominating for the auxiliary pump, and "failure to run", which is dominating for the main pump. Probability of failure to start is expressed as $P_S = qn$, where q – failure probability per demand, n – number of demands per year. Probability of failure to run is expressed as $P_R = \lambda t$, where λ – failure rate per hour, t – number of operating hours per year. Considering that failure of the pump is either "failure to start" OR "failure to run", which are mutually exclusive events, the failure probability is $P_F = P_S + P_R$.

Assuming that for the main pump AP003 these parameters are q, n_1, λ, t_1 and for the auxiliary pump AP002 q, n_2, λ, t_2. Probability of ACK10 failure P_T due to failure of one of the pumps is:

$$P_T = P_{F1} + P_{F2} = qn_1 + \lambda t_1 + qn_2 + \lambda t_2 = q(n_1 + n_2) + \lambda(t_1 + t_2).$$

Assume that operational regime is changed and that after a certain period (weekly, monthly), AP002 is used as the main pump (M) and AP003 as an auxiliary (A), and each pump is used as the main or as the auxiliary during equal amount of time per year.

Current operational regime:

AP003	**M (Main)**
AP002	A (Aux)

Changed operational regime:

AP003	**M (Main**	A (Aux)	**M (Main)**	A (Aux)	**M (Main)**	A (Aux)
AP002	A (Aux)	**M (Main)**	A (Aux)	**M (Main)**	A (Aux)	**M (Main)**

Then both pumps operate as main pumps equal number of hours $t'_1 = t_1/2$ and as auxiliary pumps also equal amount of time $t'_2 = t_2/2$. This means that each pump operates total of $t'_1 + t'_2$ hours per year. The number of starts for each pump is also equal: $n'_1 = n_1/2$ as main pump and $n'_2 = n_2/2$ as auxiliary pump, and the total number of starts for each pump is $n'_1 + n'_2$.

Equation for P_T for the changed operation regime becomes:

$$P'_T = q(n'_1 + n'_2 + n'_1 + n'_2) + \lambda(t'_1 + t'_2 + t'_1 + t'_2) = q(2n'_1 + 2n'_2) + \lambda(2t'_1 + 2t'_2) =$$
$$= q(2n_1/2 + 2n_2/2) + \lambda(2t_1/2 + 2t_2/2) = q(n_1 + n_2) + \lambda(t_1 + t_2) = P_T,$$

which means that probability of ACK10 failure due to failure of one of the pumps remains unchanged.

It may be concluded that application of equal "roles" to the pumps does not improve reliability of the system and does not reduce the risk.

Installation of a redundant (third) pump

Installation of third pump AP001 could significantly reduce unavailability of ACK10 and downtime of W7-X. In case of AP002 failure, AP001 is started up and the capacity of two pumps would be enough to ensure ACK10 operation while the failed pump is removed for repair. Downtime in this case is negligible and consists only of time to start up the third pump. Such modification reduces the unavailability of ACK10 from 0.188 to 0.0439.

To estimate the risk reduction the losses from failure should be estimated for two options: A) no change B) install the third pump.

The losses for **Option A** for one year are $C_A = C_{rA} + C_{dA}$, where C_{rA} – cost of pump repair, $C_{dA} = T_{dA}C_{tA}$ – losses from downtime, where T_{dA} – downtime for option A and C_{tA} – cost of time unit or cost of W7-X operation.

The total cost of **option B** (installation of 3rd pump) for one year is $C_B = C_{rB} + C_{dB}$, where C_{rB} – cost of pump repair, $C_{dB} = T_{dB}C_{tB}$ – losses from downtime, where T_{dB} – downtime for option B and C_{tB} – cost of time unit.

The difference of the costs is $\Delta C = C_A - C_B = C_{rA} + T_{dA}C_{tA} - (C_{rB} + T_{dB}C_{tB})$. Assuming that the costs of repair $C_{rA} = C_{rB}$ and cost of time unit $C_{tA} = C_{tB}$ are the same for both options, and that in case of the 3rd pump installation the downtime $T_{dB} = 0$ includes only time to start the 3rd pump and is negligible gives the following expression $\Delta C = C_A - C_B = T_{dA}C_{tA}$. From here it follows that the risk reduction is:

$$\Delta K = \Delta p_f C + \Delta C p_f - \Delta p_f \Delta C = \Delta p_f (C_{rA} + T_{dA} C_{tA}) + (p_f - \Delta p_f)(T_{dA} C_{tA}).$$

As probability of failure is identical to unavailability of ACK10, $p_{fA} = 0.188$. Installation of the 3rd pump would decrease unavailability to 0.044, then $\Delta p = 0.144$. Assuming that $T_{dA} = 720$ hours, $C_{rA} = 10000$ EUR, $t_L = 20$ years, $C_k = 5000$ EUR, $C_p = 120000$ EUR and estimating operational cost of W7-X $C_{tA} = 2854$ EUR/hour, the risk reduction calculation is:

Parameter	*Unit*	*Value*
C_A	EUR	2 064 880
C_B	EUR	15 000
ΔC	EUR	2 049 880
p_{fA}	–	0.188

Parameter	*Unit*	*Value*
p_{fB}	–	0.044
Δp_f	–	0.144
ΔK	**EUR**	**387 538.9**

The total cost of the third pump installation is a sum of its actual price and the service costs of the third pump $C_T = C_P + C_k t_L$, where C_P – cost of pump procurement and installation; C_k – annual cost of pump service; t_L – lifetime.

Assuming that $C_k = 5\,000$ EUR/year; $t_L = 20$ years, $C_p = 120\,000$ EUR, the total value of investment is 220 000 EUR. Risk reduction ΔK clearly indicates that the gain (prevented loss) from **Option B** exceeds the expenditures for procurement and installation of the additional pump and installation of the third pump is feasible.

Reducing repair time by providing sufficient spare parts

In the analysis repair time 1 month was assumed including time needed to procure the spare parts for repair or new item for replacement and time for repair or replacement. This might be an optimistic estimation as in some cases a procurement process could take several months. Having a stock of spare parts could significantly reduce downtime due to repair and correspondingly the repair costs. From the other side:

- keeping the stock will require additional costs for storage;
- some of the spare parts might be not required during all lifetime;
- value of the capital spent to procure the stock will be decreasing due to inflation, bank interest etc.

In this section, two options are compared, option A) no stock is kept and the spares are procured only after the failure and option B) a stock of necessary spare parts is kept.

Assuming the same parameters as in previous section: $T_{dA} = 720$ hours, $C_{rA} = 10\,000$ EUR, $C_{tA} = 2854$ EUR/hour and assuming that availability of spare parts would decrease mean downtime from one month to one week, $T_{dB} = 168$ hours, unavailability of ACK10 decreases from $p_{fA} = 1.88\times10^{-1}$ to $p_{fB} = 5.86\times10^{-2}$ and $\Delta p_f = 1.29\times10^{-1}$. Taking into account these values the risk reduction calculation gives:

Parameter	*Unit*	*Value*
C_A	EUR	2 064 880
C_B	EUR	489 472
ΔC	EUR	1 575 408
p_{fA}	–	0.188

Parameter	*Unit*	*Value*
p_{fB}	–	0.059
Δp_f	–	0.129
ΔK	**EUR**	**359 504.6**

The total cost of keeping the spare parts is a sum of costs to procure the spare parts C_s and the costs C_k for keeping the stock during lifetime t_L could be expressed as $C_T = C_S + C_k t_L$. Assuming that C_s = 15000 EUR; C_k = 5000 EUR/year; t_L = 20 years, the total value of investment is 115 000 EUR.

Risk reduction ΔK clearly indicates that the gain (prevented loss) from **Option B** exceeds the expenditures for the procurement and storage of spare parts.

Preventive maintenance

Preventive maintenance (PM) is a planned maintenance performed when an item is functioning properly to prevent future failures. Preventive maintenance allows reducing a probability of failure and corresponding repair costs. On the other hand, a too frequent maintenance increases unavailability and cost due to maintenance. In order to find the optimal maintenance period which would minimize unavailability and cost, a special model was developed.

The system with homogenous failures of exponential distribution, with failure rate λ and corresponding mean time to failure $MTTF = 1/\lambda$ is assumed. The expected number of failures (or probability of failure) of such system increases with time T and could be expressed as $N(T) = \lambda T$. When the planned maintenance is performed, the system is assumed "as good as new" after the maintenance and the process starts again. The longer is the period between the planned maintenances, the higher average failure probability is, as illustrated on Figure 3.9.

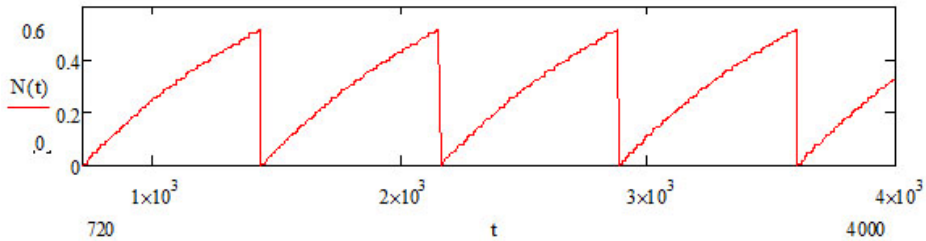

Figure 3.9
Failure probability of system with periodic repairs

Optimal period T_0 of maintenance should be chosen such that minimizes unavailability $U_t(T_0)$. Unavailability function for parameters: $\lambda = 1.47\times10^{-4}$ 1/hour; MTTR = 720 hours; MMT = 72 hours is shown in Figure 3.10. It is seen that unavailability due to failures $Uf(t)$ is linearly increasing when t increases. This is obvious that the longer the maintenance interval is, the higher is the probability of failure before the maintenance. Unavailability due to maintenance $Um(t)$ is high when the maintenance is very frequent (low t) and decreases with the increase of the maintenance interval. Total unavailability $Ut(t)$ which is a sum of these two decreases with $Um(t)$ when $Uf(t)$ is low, reaches the minimum and increases with $Ut(t)$. The optimal maintenance interval is such value of t where $Ut(t)$ is minimal.

The optimal maintenance period for unavailability minimization T_u = 2202 hours, which corresponds to approximately 3 maintenances per year. Unavailability of ACK10 auxiliary pump in this case decreases from the current value 0.096 to 0.052, i.e. by ~46%. Total unavailability of ACK10 system decreases from 0.188 to 0.148.

As the maintenance decreases only the unavailability and does not affect downtime due to repair T_{dA}; cost of time unit (operational cost of W7-X) C_{tA}; and cost of repair C_{rA}, the total cost of repair for option B does not change and therefore $\Delta C = 0$. The risk reduction is therefore:

$$\Delta K = \Delta p_f C + \Delta C p_f - \Delta p_f \Delta C = \Delta p_f C.$$

Assuming the same parameters as in previous section: T_{dA} = 720 hours, C_{rA} = 10 000 EUR, C_{tA} = 2854 EUR/hour, the risk reduction calculation is:

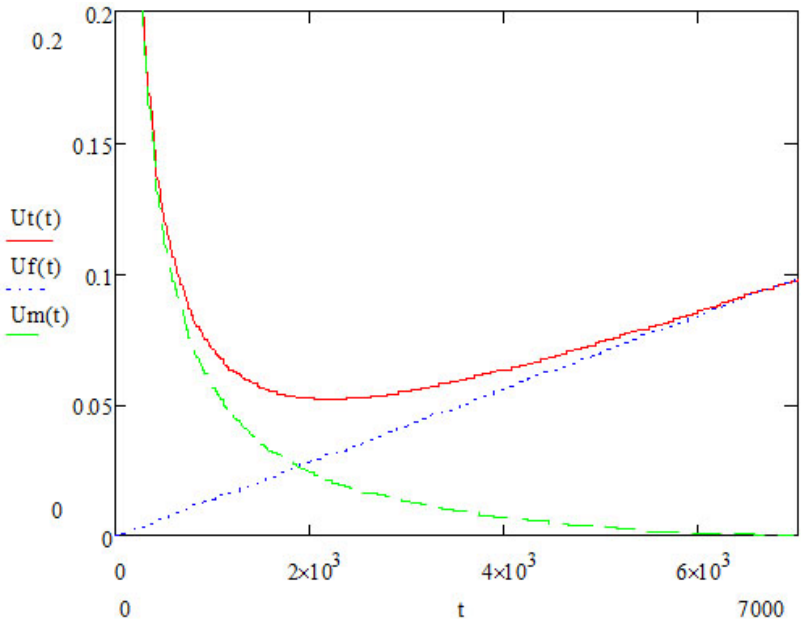

Figure 3.10
Unavailability dependence on maintenance interval

Parameter	*Unit*	*Value*
C_A	EUR	215 200
p_{fA}	–	0.188
p_{fB}	–	0.148
Δp_f	–	0.04
ΔK	**EUR**	**82 595**

The total expenditures for maintenance during the lifetime are calculated as $C_T = C_H\, MMT\, t_L/T_0$, where C_H – hourly rate (including labour cost and necessary spares). Assuming that C_H = 10 EUR/hour; MMT = 72 hours; t_L = 20 years, the total expenditures are is 42 677 EUR.

The risk reduction ΔK clearly indicates the gain (prevented loss) from the preventive maintenance exceeds the expenditures for it. Analysis result shows that this option is feasible.

Comparison of considered alternatives

A comparison of considered alternatives for risk reduction is presented in Table 3.6. The lowest risk corresponds to the installation of redundant 3rd pump. However, the cost of risk decrease should also be considered.

Table 3.6 Comparison of risk for risk decrease options

Option	*Failure probability (pf)*	*Loss given failure (C), kEUR*	*Risk (K), kEUR*
Current status	0.188	2064.88	388.20
Installation of 3rd pump	0.044	10.00	0.44
Spare parts	0.059	489.47	28.69
Maintenance	0.148	2064.88	305.60

The cost effectiveness of expenditures for risk reduction is calculated as ratio between risk reduction ΔK and total expenditures C_T for each option. The result is presented in Table 3.7. Cost effectiveness indicates risk reduction gained for each euro invested to reliability increase. From the cost effectiveness perspective, the option of keeping the necessary set of spare parts in order to decrease repair time is preferable.

Table 3.7 Comparison of cost effectiveness for risk decrease options

Option	*Risk reduction ΔK, kEUR*	*Expenditures C_T, kEUR*	*Cost effectiveness, $\Delta K/C_T$*
Installation of 3rd pump	387.8	220.0	1.8
Spare parts	359.5	115.0	3.1
Maintenance	82.6	42.7	1.9

3.2.3 Summary on ACK10 availability increase measures

Four options for increasing ACK10 availability were analyzed:

1. Changing pump operation mode;
2. Installation of third redundant pump;
3. Keeping a set of necessary spare parts;
4. Preventive maintenance of the pumps.

Option 1 has no effect on overall system reliability. Options 2, 3, 4 were compared using a risk decrease and cost effectiveness criteria. The risk was expressed in terms of losses from non-operating W7-X and a cost of W7-X operation. The cost effectiveness shows risk decrease in EUR for each EUR spent.

From the risk decrease perspective, Options 2 and 3 are similar. However, from the cost effectiveness perspective, Option 3 is preferable. Option 4 gives the least risk decrease.

Taking into account the performed analysis, it is recommended to keep a set of the necessary spare parts in order to reduce the repair time for ACK10 pumps. Such set may be recommended by the manufacturer. Keeping the records of the operating experience and statistics of failures and repairs will provide more objective information.

4 THEORETICAL STUDIES OF THE SPECTROSCOPIC CHARACTERISTICS OF HIGHLY CHARGED TUNGSTEN ATOMS HAVING OPEN D AND F-SHELLS ACCOUNTING FOR RELATIVISTIC AND CORRELATION EFFECTS

Tungsten is known as a heat-resistant matter. Usage of tungsten as a plasma-facing material resolves the tritium retention issue but it brings new challenges in implementation of high-performance long-lasting fusion devices needed for energy production. If tungsten or another high-Z element is detached from the wall and penetrates into the thermonuclear plasma, it irradiates strongly thus cooling the plasma. It is necessary to ensure that inner walls of the reactor last for a rather long period of time reasonable for industrial and not only experimental exploitation. Thus tungsten abundance inside the thermonuclear reactor must be carefully controlled. For this purpose, relevant spectroscopic data on characteristics of various tungsten ions are necessary. Unfortunately the spectra of majority of these ions are very complicated, and in many cases they form quasi-continuum or emission bands. So both the experimental and theoretical investigation of spectral properties of tungsten ions are a complex task still far from completion.

4.1 Developing of methods and packaging for including the QED effects in the quasi-relativistic energy spectra calculations

During 2010, according to a work plan, we performed theoretical studies of the spectroscopic parameters of multicharged tungsten ions having open 4d-shell. Calculations were performed in quasirelativistic approximation with extensive inclusion of correlation effects. It was demonstrated that this approach enables achieving accuracy not worse than the accuracy of the completely relativistic *ab initio* calculation results.

In 2011, the results obtained in 2010 were prepared for publication. Two research papers were submitted, and one of them was published. We have studied the influence of configuration basis size on the determined results in the first of these papers [4.1]. The second paper [4.2] deals with the ground $4p^6 4d$ configuration and excited $4p^6 4f$ and $4p^5 4d^2$ configurations of the W^{37+} ions. The energy levels, parameters of their wave function expansion, Lande-factors, radiative lifetimes have been presented coupled with data for the electric dipole, electric quadrupole and magnetic dipole transitions inside and between the investigated configurations. Another paper on the spectroscopic data for the W^{36+} ions was submitted for publishing.

The main task for 2011 was to perform a feasibility study of adopting quantum electrodynamics calibration (QED) corrections in the quasirelativistic approximation. It is an absolutely innovative and original idea, because such up-to-date kind of corrections was included only in a completely relativistic approach. Two completely different ways to evaluate QED corrections are used in this approach; both of them have been implemented in our quasirelativistic approximation.

The first method employs interpolation of hydrogen like ions Lamb-shift values for multi-electron atoms. We adopt data from [4.3], where various QED correction values are given for $1s_{1/2}$, $2s_{1/2}$, $2p_{1/2}$ ir $2p_{3/2}$ electrons for the hydrogen-like ions from Z = 1 to Z = 100. The tabulated data from this work are included in our computer software and are exploited to determine Lamb-shifts in multi-electron atomic systems. The calculation of corrections is based on assumption that their values are proportional to the electron densities determined close to the coordinates origin:

$$E_{QED\,QR}(n\ell) = E_{QED\,Hydr}\frac{\rho_{QR}(n\ell\,/\,r_0)}{\rho_{Hydr}(n_0\ell_0\,/\,r_0)}.$$

Here $E_{QED\ Hydr}$ is the correction utilized from [4.3], $\rho_{Hydr}(n_0\,\ell_0/r_0)$ is Dirac-function density for the $n_0\,\ell_0$ electron at the r_0 distance from nucleus and $\rho_{Hydr}(n_0\,\ell_0/r_0)$ is the density of the investigated electron quasirelativistic radial orbital at the same distance. It is a standard practice to use the distance $r_0 = \lambda_e$, which is equal to Compton wavelength of electron.

Some issues were dealt with during realization of this approximation. First of all, data for electrons with $n \leq 2$ only are present in [4.3]. Therefore, for the electrons having higher principal quantum numbers, some external QED correction values must be adopted. Secondly, the Dirac functions were determined for the point-like nucleus, whereas our quasirelativistic radial orbitals are calculated assuming a finite nucleus size. This causes some deviations to the ratio of densities which are difficult to assess. Additionally, it is complicated to get averaged over their total momentum corrections for the p-electrons, because quasirelativistic radial orbitals are *j*-independent. It is very likely that a regular averaging over *j* does not suite here. Therefore, it is necessary to create a method similar to that for the spin-orbit interaction averaging for *p*-electrons, as it was performed in [4.4].

The above-mentioned issues have pressured us into adoption of another way to calculate QED corrections, i.e. vacuum polarization method. This approximation is based on special potential, as it was described in [4.5]. For a spherically-symmetrical nuclear field, this potential is given by

$$V(r) = -\frac{2}{3}\frac{\alpha\lambda_e}{r}\int_0^\infty x\rho(x)\left[K_0\left(\frac{2}{\lambda_e}|r-x|\right)\right] - K_0\left(\frac{2}{\lambda_e}|r+x|\right)dx\,.$$

Here $4\pi\int_0^\infty \rho(x)dx = Z$ and K_0 are specifically constructed functions:

$$K_0(y) = \int_1^\infty \exp(-yt)\left(\frac{1}{t^3}+\frac{1}{2t^5}\right)\left(t^2-1\right)^{1/2}dt\,.$$

The ways to determine these functions are given in [4.5]. The potential *V(r)* is obtained employing these functions. Furthermore, one-electron vacuum polarization correction is determined by integrating this potential with quasirelativistic radial orbitals. This method has been implemented in computer codes and their test runs are performed. The aim is to achieve an accurate agreement of the results obtained by two completely different approximations. Only after accomplishing such an agreement, we can ensure that determined QED corrections are reliable and, consequently, can be adopted in calculations of atomic spectroscopic data.

4.2 Investigation of the configuration interaction regularities in the ground and excited configurations of tungsten ions using the average characteristics of CI

In **2010**, the calculation of fluorescence yields, Auger transition probabilities and natural level widths for the states of multiple ions of tungsten with vacancies in the 4ℓ (ℓ = 0–3) shells were performed. The Auger transitions in the low and middle charged tungsten ions from the initial states with vacancies in the 4s, $4p_{1/2}$, $4p_{3/2}$, $4d_{3/2}$, $4d_{5/2}$ subshells and 4f shell were considered. The calculations of radiative transition spectra in the regions of 4–7 nm and 12–14 nm for W^{40+} – W^{45+} and electron-impact excitation rates among the levels of $4d^N$ configurations for tungsten ions were also performed.

The energy level and emission spectra of tungsten have been calculated in various approximations, often using the efficient correlation method – configuration interaction (CI) ([4.6, 4.7, 4.8, 4.9] and other references therein). The main aim of most works is to obtain the reliable spectroscopic data, to interpret experimental spectra or to predict new levels or lines. On the other hand, the consideration of the average characteristics of CI and their influence on the transition arrays can reveal some regularities of CI manifestation in various ions of tungsten. This was **the aim** of the work in **2011**.

In the lowest order of perturbation theory the interaction of two levels is proportional to the matrix element of Hamiltonian between them and inversely proportional to the energetic distance between these levels. Thus, the following quantity and the configuration interaction strength can be used as a measure of CI between two configurations *K* and *K′* [4.10]:

$$T(K,K') = \frac{\sum_{\gamma\gamma'} <K\gamma|H|K'\gamma'>^2}{E_{av}(K,K')}, \tag{1}$$

where the quantity in the numerator is the interconfiguration matrix element of the Hamiltonian *H,* the summation is performed over all states γ and γ′ of both configurations *K* and *K′*, and $E_{av}(K,K')$ is the average energy distance between the interacting states of these configurations:

$$E_{av}(K,K') = \frac{\sum_{\gamma\gamma'} E(K\gamma)-E(K'\gamma') <K\gamma|H|K'\gamma'>^2}{\sum <K\gamma|H|K'\gamma'>^2}. \tag{2}$$

The neutral atom and first ions of tungsten contain 5d and 6s electrons of the same parity and they are localised approximately at the same average distance from the nucleus. Thus configurations $5d^N$, $5d^{N-1}6s$ and $5d^{N-2}6s^2$ strongly interact among themselves; their set even has the special notation $(5d+6s)^N$. The variation of these main average characteristics on increasing the ionization degree from W till W^{5+} is shown in Table 4.1. Here the configuration interaction strength *T(K,K′)* as well as its constituents, the average energy (2) and the sum contained in the denominator of the right side of Eq. (1), are presented.

The interaction between all three pairs of configurations is the strongest for single ion W^+. It is mainly determined by the average distance: this quantity changes its sign on going from neutral atom to single or double ion and obtains the minimal value namely for W^+. This is related with the change of the relative position of energy level spectra for these configurations. In neutral atoms the tendency of their location can be characterised by the sequence of their average energies:

$$E_{av}(5d^N\,6s^2) < E_{av}(5d^{N-1}6s) < E_{av}(5d^{N-2}). \tag{3}$$

Upon increasing the ionization degree, the configurations with a larger number of 5d electrons, orbitals of which are located within a narrower potential well, are shifted down faster, thus the inequality (3) is reversed. The largest overlap of energy level spectra takes place namely for W^+. Further in the isonuclear sequence the overlap of these spectra diminishes, and they are moved apart from each other.

On the other hand, the configurations with symmetric exchange of symmetry belonging to the same complex of configurations overlap strongly at various ionization degrees. The CI of such type dominates in the following intervals of tungsten ionization degrees *q*:

$$4p^5 4d^{N+1} + 4p^6 4d^{N-1}4f, \quad q = 29–37, \tag{4}$$

$$4s4p^{N+1} + 4s^2 4p^{N-1}4d, \quad q = 39–43, \tag{5}$$

Table 4.1

Transitions	*Quantity*	*Tungsten atom or ion*				
		W	W^{+}	W^{2+}	W^{3+}	W^{4+}
$5d^N \rightarrow 5d^{N-1}6s$	$S<\|H\|>^2$	0.218	0.259	0.169	0.059	0.009
	$E_{av}(K,K'')$	0.076	0.014	-0.067	-0.160	-0.261
	$T(K,K')$	37.5	1370	37.9	2.31	0.126
$5d^N \rightarrow 5d^{N-2}6s^2$	$\Sigma<\|H\|>^2$	0.128	0.120	0.065	0.019	0.002
	$E_{av}(K,K'')$	0.129	0.029	-0.099	-0.246	-0.404
	$T(K,K')$	7.71	144	6.59	0.319	0.015
$5d^{N-1}6s \rightarrow 5d^{N-2}6s^2$	$\Sigma<\|H\|>^2$	0.229	0.158	0.057	0.008	
	$E_{av}(K,K'')$	0.054	-0.016	-0.102	-0.198	
	$T(K,K')$	77.3	592	5.45	0.215	

$$3s3p^{N+1} + 3s^2 3p^{N-1}3d, \quad q = 57–61. \tag{6}$$

The strongest CI takes place between configurations (4) due to large values of interconfiguration matrix elements and small distances between interacting levels. Upon increasing the effective charge of nucleus, the binding energies of electrons with the same principal quantum number tend to get closer to the hydrogenic limit. Thus the interaction is stronger between configurations (6) corresponding to higher ions than between configurations (5). In all three cases *T(K,K′)* obtains its largest value for the half-filled shell.

Both excited configurations are related by the electric dipole transitions to the ground configuration, thus CI of such type strongly influences the corresponding emission spectra. The main effect is the concentration of lines in a narrow interval of wavelengths and quenching of many other energetically allowed lines [4.10, 4.11]. In the low density plasma, the ions of tungsten are mainly excited from their ground levels. The conditions for the formation of the narrow group of lines in the emission spectra generated in such a way were formulated in [4.12]. When such conditions are fulfilled the emission spectra contain one narrow group of intense lines, it takes place for transitions (4) at $4 \leq N \leq 9$ and for transitions (5) and (6) at $2 \leq N \leq 5$. On the other hand, according to our calculation results, the other group of intensive lines also remains for the total transition arrays of transitions (5) and (6).

These results are under preparation for publication. The other work was finished in which the calculated data for Auger yields, total radiative Auger and radiative widths of levels and fluorescense yields were presented and analysed for N_i subshells of tungsten ions [4.13].

4.3 Theoretical studies of electronic transitions of higher multipolarities in tungsten ions having open f-shell

In 2010 year, large-scale nonrelativistic and relativistic calculations of the lowest 997 energy levels of W^{24+} accounting for the correlation, relativistic, and QED effects were performed. They demonstrated the high efficacy of the methods used [4.14, 4.15]. All these levels correspond to $[Kr]4d^{10}4f^4$, $[Kr]4d^{10}4f^3 5s$, $[Kr]4d^{10}4f^3 5p$, and $[Kr]4d^9 4f^5$ configurations. The main peculiarity of the ground configuration consists in the fact that the electron transitions in the usual form of electric-dipole radiation from the closest excited configurations to the ground configuration are strictly forbidden.

In 2011, higher multipolarities were investigated. Usually, it is accepted that the probabilities of the electric-multipole electron transitions are rapidly decreasing functions of their multipolarity. Therefore, while calculating the probabilities of electronic transitions between the configurations of certain chosen parities, it seems sufficient to take into account the first nonzero term, i.e., to consider the electron transitions of lowest multipolarity permitted by the exact selection rules. This year work aims at verifying this assumption on the example of electric-octupole transitions in W^{24+} ion. For this purpose the large-scale multiconfiguration Hartree-Fock and Dirac-Fock calculations have been performed for the configurations $[Kr]4d^{10}4f^4$ and $[Kr]4d^{10}4f^35s$ energy levels of W^{24+} ion. The relativistic corrections were taken into account in the quasirelativistic Breit-Pauli and fully relativistic Breit (taking into account QED effects) approximations. The role of correlation, relativistic, and QED corrections is discussed. Line strengths, oscillator strengths, and transition probabilities in Coulomb and Babushkin gauges are presented for *E*1 and *E*3 transitions among these levels.

4.3.1 Large scale calculations

In the Figure 4.1 and Figure 4.3, we present the oscillator strengths nd transition probabilities of the most probable *E*1 transitions in the Babushkin gauge. As seen from it, within the W^{24+} theoretical emission spectra, there are some transitions with probabilities significantly higher than others. The *E*1 transition probabilities A_B are in the interval 10^2–10^6 s^{-1}. All values are located in the wavelength interval 100–190 Å.

The following *E*1 transition

$$\{[Kr]\ 4d^4\ 4d^64f^2\ (J = 2)\ 4f^2(J = 2)\ J = 2^+\} \rightarrow \{[Kr]\ 4d^4\ 4d^64f\ 4f^2(J = 0)\ 5s\ J = 3^-\}$$

has the highest probability, namely, $\lambda = 121.1$ Å, $A_C = 2.749\times10^7\ s^{-1}$, and $A_B = 2.238\times10^6\ s^{-1}$ from Table 4.2. Table 4.2 lists 15 *E*1 transitions having the largest probabilities exceeding $10^6\ s^{-1}$. The most remarkable is the transition $\lambda = 132.26$ Å, $A_C = 4.815\times10^7\ s^{-1}$ and $A_B = 2.063\times10^6\ s^{-1}$ (see Table 4.2):

$$\{[Kr]\ 4d^4\ 4d^64f^2\ (J = 2)\ 4f^2(J = 2)\ J = 0^+\} \rightarrow \{[Kr]\ 4d^4\ 4d^64f\ 4f^2\ (J_2 = 2,\ J_{12} = ½)\ 5s\ J = 1^-\},$$

which is a strictly forbidden *E*3 transition, because its $J = 0$ and $J' = 1$. The probability of this transition A_B is the second largest out of all transitions considered (see Fig. 4.3).

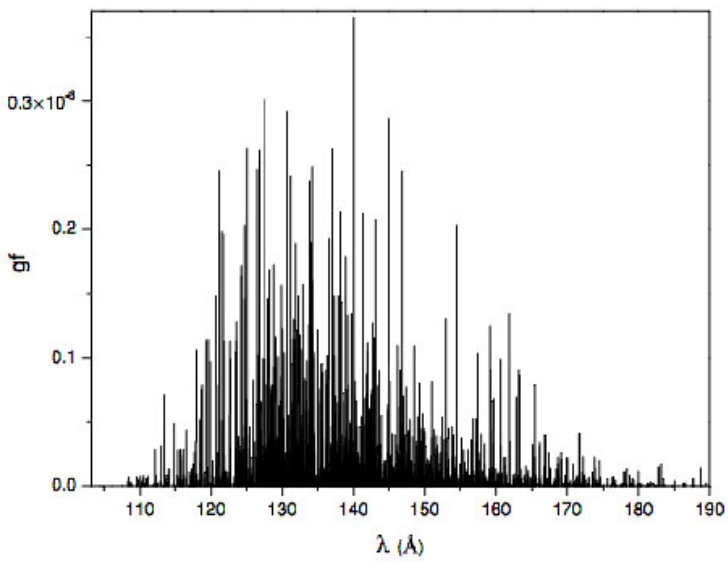

Figure 4.1
Theoretical *E*1 transition oscillator strengths forW^{24+} in the MCDF+Breit+QED approach with AS_7 atomic state function expansion (single excitation) between the levels of $4d^{10}4f^35s$ and $4d^{10}4f^4$

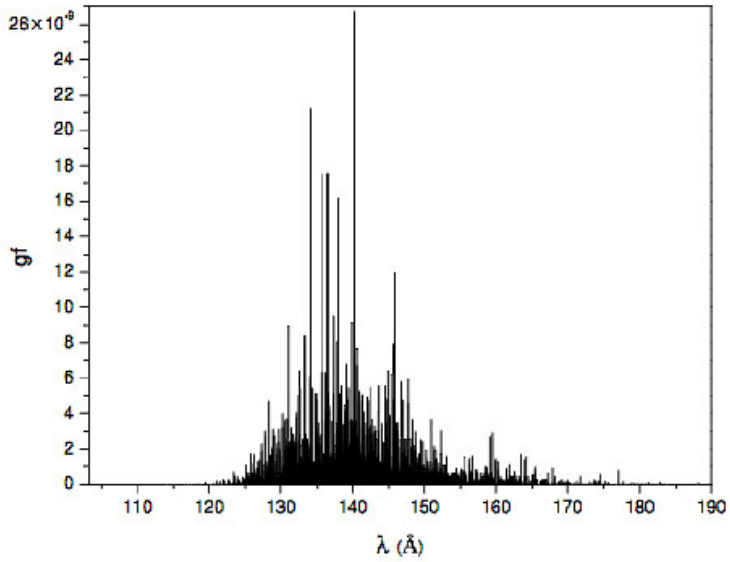

Figure4.2
Same as Figure 4.1, but for *E*3 transition oscillator strengths

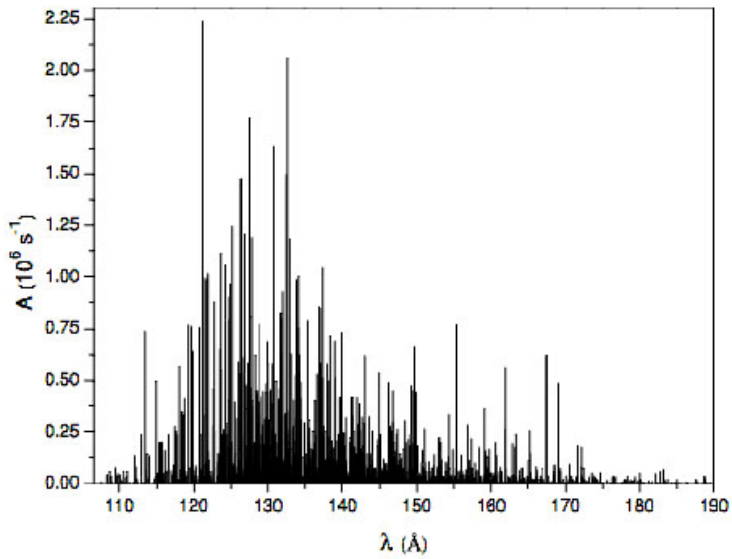

Figure 4.3
Theoretical *E*1 transition probabilities for W^{24+} in the MCDF+B+QED approach with AS_7 atomic state function expansion (single excitation) between the levels of $4d^{10}4f^{3}5s$ and $4d^{10}4f^{4}$

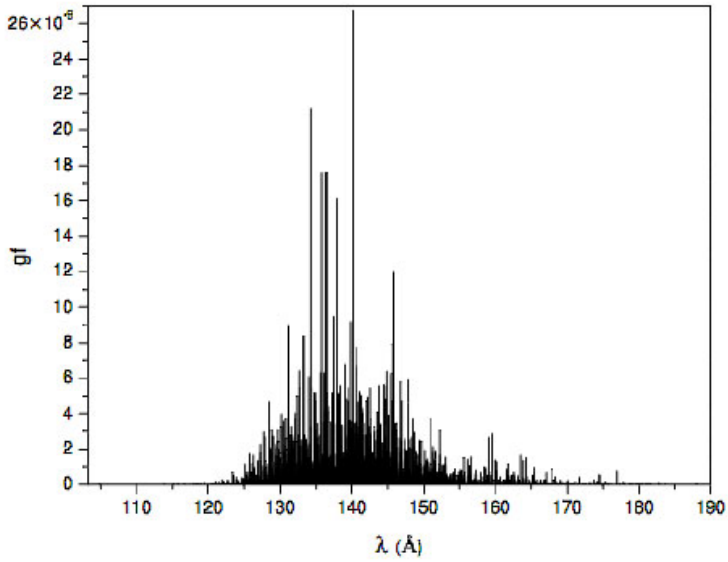

Figure 4.4
Same as Figure 4.3, but for *E*3 transition probabilities

Table 4.2 Calculated wavelengths λ (in) and transition probabilities A_B (in 10^6 s^{-1}) for W^{24+} (A_B exceeding or equal to 1 000 000 s^{-1}) of $E1$ transitions between the levels of configurations $[Kr]4d^{10}4f^3 5s$ and $[Kr]4d^{10}4f^4$

Upper		Lower			
w	*JP*	*w*	*JP*	λ(Å)	$A_B(10^6\ S^{-1})$
1	0+	6	1–	132.6	2.063
4	1+	11	2–	132.5	1.493
10	2+	13	2–	121.9	1.015
15	2+	13	2–	137.3	1.046
9	2+	11	3–	132.8	1.187
11	2+	13	3–	123.6	1.115
10	2+	14	3–	121.1	2.238
13	2+	14	3–	127.9	1.192
9	3+	13	3–	124.2	1.058
11	3+	14	3–	127.5	1.770
12	3+	14	3–	130.7	1.632
1	3+	4	4–	134.1	1.006
4	3+	11	4–	126.4	1.472
7	4+	13	4–	125.1	1.247
7	4+	12	5–	126.8	1.207

The rest of the $E1$ transitions presented in Table 4.2 are also allowed $E3$ transitions. In Figures 4.2 and 4.4, we present the oscillator strengths and transition probabilities of the most probable electric $E3$ transitions in the Babushkin gauge. There are 103 such transitions. The largest probability belongs to the transition $\lambda = 140.2$ Å, $A_C = 4.890$ and $A_B = 4.317\ s^{-1}$,

$$\{[Kr]4d^4\ 4d^6 4f\ 4f^3\ J = 15/2\ J = 10^+\} \rightarrow \{[Kr]4d^4\ 4d^6 4f\ 4f^2\ (J_2 = 6\ J_{12} = 17/2)\ 5s\ J = 8^-\}.$$

All A_B values are localized in the wavelength interval 100–190 Å. There are 55 common ($E1$ and $E3$) transitions, but in all cases, the contributions of $E1$ transition probabilities are six to seven orders of magnitude larger than those of the relevant $E3$ transitions.

4.3.2 Error estimates and conclusions

The problem of the accuracy of the energy levels of the electronic configurations of the W^{24+} considered was already discussed in [4.15]. It is expected that the accuracy of the theoretical values of the $E3$ transition probabilities will be slightly worse than those of the $E1$ permitted transitions in this ion [4.15]. The same conclusion is valid for the $E1$ transitions calculated here, which become allowed due to correlation effects. The latter are accounted for in the form of the wave function as the linear combination of principal configuration and a set of admixed configurations with the relevant weights. While calculating the matrix elements of the $E1$ electronic transition considered here, the term representing the product of principal configurations involved in the transition equals zero, but there are other terms containing one of the principal and one admixed configuration, as well as only admixed configurations, whose quantum numbers satisfy the selection rules for the $E1$ transition. Of course, due to cancellation effects, the accuracy of the results decreases, but in this paper we are mainly interested in qualitative effects, namely, in the studies of the role of the $E1$ transitions becoming permitted when accounting for correlation effects.

Thus, taking into account the correlation effects, the large part of *E*3 transitions may be described as *E*1 transitions, and their transition probabilities are approximately six or seven orders of magnitude larger than those of the relevant *E*3 transitions satisfying the same selection rules for *J* and *J′*. This means that a part of electric-octupole transitions may be interpreted as electric-dipole transitions. Their maximal probabilities are of the order 10^{+6} s^{-1} compared to 100 s^{-1} of the relevant *E*3 transitions (compare Figure 4.3 and Figure 4.4).

In conclusion, the results obtained reveal several qualitative effects. First, a large part of electronic transitions with $\Delta\ell = \pm 3$ may be interpreted as electric-dipole transitions $\Delta\ell = \pm 1$ if one is to account for correlation effects. Second, in this approach, the probabilities of the *E*1 transitions, allowed also in the case of the *E*3 transitions, exceed, as the rule, the latter by a factor of 10^6. Then *E*3 transitions become actually the very small corrections to *E*1 values. Among the *E*1 transitions, the transitions with $J \leq J'$ (*J* is the upper level) have larger probabilities than those with $J > J'$.

The third qualitative effect consists in the phenomena that the strictly forbidden by triangular condition $\{J,J',k\}$ *E*3 transitions between $J = 0$, $J' = 1$ or $J = 1$, $J' = 0$, and $J = J' = 1$ become also allowed and have large probabilities. Then we see from the selection rules for discrete transitions that only the transitions with $J = J' = 0$ and $J = 0$, $J' = 2$ or $J = 2$, $J' = 0$ still remain strictly forbidden [4.16].

It would be very promising to check experimentally the phenomenon described in the paper [4.16] by measuring the wavelengths and intensities of electronic transitions between the configurations in W^{24+}, considered here, in the wavelength regions 100–200 Å and by the identification and classification of these transitions, if necessary with the assistance of the relevant theoretical studies.

4.4 References

4.1. P. Bogdanovich, O. Rancova and A. Štikonas, Phys. Scr. 83 065302 (7pp) (2011).

4.2. P. Bogdanovich and R. Kisielius, Theoretical energy level spectra and transition data for 4p64d, 4p64f and 4p54d2 configurations of W37+ ion, Atomic Data and Nuclear Data Tables, 98, 580-594 (2012).

4.3. W. R. Johnson and G. Soff, Atomic Data and Nuclear Data Tables, 33, 405-446 (1985).

4.4. P. Bogdanovich and O. Rancova, Phys. Rev. A, 76, 012507 (6pp) (2007).

4.5. L. W. Fullerton and G. A. Rinker, Jr., Phys. Rev. A, 12, 1283-1287 (1976).

4.6. J. Reader. Phys. Scr. T134, 014023 (2009).

4.7. A. Kramida. T.Shirai. Atom. Data Nucl. Data Tables 95, 305 (2009).

4.8. A. Kramida. Canad. J. Phys. 89, 551 (2011).

4.9. R. Karazija. Sums of Atomic Quantities and Mean Characteristics of Spectra (Vilnius: Mokslas, 1991) [In Russian].

4.10. J. Bauche, C. Bauche-Arnoult, M. Klapisch, P. Mandelbaum and J-L. Schwob. J. Phys. B 20, 1443(1967).

4.11. S. Kučas, R. Karazija, V. Jonauskas and A. Momkauskaitė. J. Phys. B 42, 205001 (2009).

4.12. R. Karazija, S. Kučas, V. Jonauskas and A. Momkauskaitė. In: Atomic, Molecular Physics and its Applications to Astrophysics and Plasma. Proceedings of CDAMOP 2011 (Review paper accepted for publication).

4.13. S. Kučas and R. Karazija. Lithuan. J. Phys. 51, 198 (2011).

4.14. Z. Rudzikas, Theoretical Atomic Spectroscopy, 2nd ed. (Cambridge University, New York, 2007).

4.15. G. Gaigalas, Z. Rudzikas, E. Gaidamauskas, P. Rynkun, and A. Alkauskas, Phys. Rev. A 82, 014502 (2010).

4.16. G. Gaigalas, Z. Rudzikas, P. Rynkun, and A. Alkauskas, Phys. Rev. A 83, 032509 (2011).

5 MOBILITY PROGRAM 2011

During 2011 the following visits were implemented under the mobility plan:

4.7 Fusion safety issues

In 2011 it was planned to participate in missions and secondments to IPP-Griefswald, Germany. These actions were implemented by Tadas Kaliatka, Gintautas Dundulis, Renatas Karalevičius, Egidijus Urbonavičius, and Robertas Alzbutas, Roman Voronov, and Sigitas Rimkevičius.

During the year 2011, Mr. R. Voronov had three long-term secondments to IPP – 30 days duration each. During these visits, he collected data, developed models and performed the System Reliability Analysis. The methods similar to ITER RAMI (Reliability, Availability Maintainability Inspectability) were applied for this analysis. Divertor Target Cooling Circuit ACK10 was chosen for investigation.

During the visit of Mr. R. Karalevičius at IPP, the technical meeting with IPP experts (A. Tereshchenko, J. Fullinger, V. Bykov) was arranged. The results of the stress analysis of the ports AEU30, AEQ20 and AEK20 were presented. With IPP experts the future co-operation was discussed.

Mr. G. Dundulis with IPP representatives discussed and identified possible parts of piping system for the pipe whip analysis to be performed in the future. It was agreed that the finite elements models will be prepared for this analysis.

Mr. E. Urbonavičius discussed results of the plasma vessel pressurisation in case of LOCA and results of assessment of plasma vessel venting system capacity. Both analyses were performed using lumped parameter code COCOSYS. The results of PV venting system capacity were compared with RELAP5 code analysis. Mr. Naujoks made some comments how the performed analyses could be improved and what additional data could be presented in the technical report.

Mr. S. Rimkevičius together with Mr. Naujoks discussed the co-operation in 2011 and plans for 2012 and beyond. Detailed discussions were held on the topics of probabilistic system analysis, models of W7-X cooling circuit and plasma vessel for RELAP5, ASTEC and COCOSYS codes. The achievements of 2011 were discussed and co-operation activities for 2012 were agreed upon. Also a meeting with Mr. S. Bosch of IPP was held to discuss the activities in reliability, availability and maintainability analyses for W7-X that are carried out by LEI.

Meetings under EFDA:

Robertas Alzbutas participated in the EFDA Public Information Group Annual Meeting, which was held at EURATOM/IPP in Greifswald (Germany) on June 15-18, 2011. At EFDA Public Information Group (renamed to Public Information Network) annual meeting various public information and communication activities, including best practises, of EFDA member organisations were presented. Demonstration on 3D Stereoscopic Interactive Fusion Show was performed. The activities for Public Information at W7-X, ITER and "Fusion for Energy" were presented. Several workshops on public information and communication (e.g. Fusion after Fukushima Daiichi accident) issues were held. Guidelines for future activities were discussed.

6 OTHER ACTIVITIES IN MAGNETIC CONFINEMENT FUSION

In 2011 VU TFAI worked under subcontract agreement between University of Strathclyde and Vilnius University. The tasks were the following:

- A benchmark study for W I, W II, and W III using the Bogdanovich's quasi-relativisitic (QRHF) approach. The structure and transition probability studies will be extended to implement plane-wave Born cross sections so that delivery can be in the form of ADAS adf04 datasets. Professor N. R. Badnell from ADAS-EU will collaborate with Professor P. Bogdanovich and his co-workers and provide support procedures and sub-routines so that the link from the structure to the plane-wave Born can be made.
- A benchmark study in Dirac-Fock approximation of a selected lanthanide-like ion in a low charge state (~6-12). The study is designed to assess the possibility of more extensive use of such heavy elements as markers (observed in low ionisation stages in divertor regimes) and edge transport studies and cross-reference other approximate studies of low charge state tungsten ions. Suitable ions would be W^{+8} (Dy-like).
- Multiple electron ionisation rate coefficients, with special emphasis on 4d, 4f and 5d, 5f open-shell systems. The study should be based on contiguous sets of iso-nuclear ions of selected elements from which approximate general prescriptions can be inferred. This will include design of an extension of ADAS data formats adf23 and adf07.
- Exploitation of ITPA special studies of key complex ion configuration interactions (such as symmetric exchanger of symmetry) by inclusion in ADAS data format adf54, tuned to primary resonance line spectroscopy, with special emphasis on 4d, 4f and 5d, 5f open-shell systems.

All tasks were completed, and the computer codes were developed. They enabled us to calculate successfully the electron-impact excitation in plane-wave Born approximation for H, He, Li and Fe^{21+} by using the data of the energy level spectra obtained in the quasirelativistic approach. This approach was developed in the Department of Atomic Theory of Institute of Theoretical Physics and Astronomy, Vilnius University. Several exploratory calculations were performed for the tungsten W^{2+} ion. The peculiarities of W^{8+} were investigated taking into account both relativistic and correlation effects. Double ionisation rate coefficients for W^{3+}, W^{4+} and W^{5+} ions were calculated. The energy level spectra, cross sections of single ionization and excitation by electron impact as well as rates of Auger transitions have been obtained. They demonstrated that the direct double ionization may play the main role in producing doubly-ionized ions. The configuration interaction (CI) effects in the W^{+13} and W^{20+} ions by employing the extended basis of interacting configurations were studied. The data were used for the simulation of the spectra emitted from EBIT plasma. Their applicability for the simulation of JET plasma was also discussed.

7 PUBLIC INFORMATION

The information related to FUSION energy perspectives, last achievements in ITER development and other Fusion research fields is continuously distributed among universities, R&D institutions, schools:

- March 16, 2011. "Career days 2011" at Kaunas University of Technology, Kaunas Lithuania. Distribution of information and discussions on FUSION to students. (http://www.lei.lt/main.php?m=466&l=1412&k=1)
- March 19, 2011. Competition "EnIdėja – Green Energy Idea 2011" at Vytautas Magnus University, Kaunas Lithuania. Distribution of information on FUSION to graduating students of Secondary schools. (http://www.lei.lt/main.php?m=466&l=1414&k=1)
- May 05, 2011. Open days of Lithuanian Energy Institute. Distribution of information and discussions on FUSION to students. (http://www.lei.lt/main.php?m=466&l=1446&k=1)
- May 26-27, 2011. 8th Conference of Young Scientists on Energy Issues CYSENI 2011 (www.cyseni.com). In the conference "Fusion energy" topic is included (1 of 11). Three papers (University of Latvia and Lithuanian Energy Institute) presented. (http://www.lei.lt/main.php?m=466&l=1448&k=1)
- September 23, 2011. FP7 project "Researchers' night 2011" LT-2011 (call FP7-PEOPLE-2011-NIGHT). Consortium of Lithuanian Society of Young Researchers, five Lithuanian universities and two research institutes won the project. Lecture and discussions on FUSION to students held. (http://www.lei.lt/main.php?m=466&l=1570&k=1)
- Fusion activities are indicated in "Annual report 2010" of Lithuanian Energy Institute (in Lithuanian and English). Reports are distributed to energy-related companies in Lithuania and abroad, associations, ministries, Lithuanian and foreign embassies, various entities. Reports are distributed at conferences, trade shows, during the visits to the Lithuanian Energy Institute.

The information related with FUSION energy perspectives, last achievements in ITER development and other Fusion research fields is continuously distributed among universities, R&D institutions, schools:

- Occasionally, school teachers (physics, chemistry …) from various regions of Lithuania visits Institute. In addition, they receive information and brochures on fusion. Information is spread via personal contacts as well.
- Agency of Science, Innovation and Technology (http://www.mita.lt), which is responsible for co-ordination of FP7, Eureka and other international programmes activities in Lithuania is provided with the material. During other events at the Agency, participants can familiarise with the material.

All activities which were organised in Lithuanian Energy Institute are mentioned (with photos, presentations) on the web-site of Lithuanian Energy Institute http://www.lei.lt in section "News" -> "News archive" (both in English and Lithuanian versions).

Information on FUSION and EURATOM-LEI activities is placed on the web-site of Lithuanian Energy Institute http://www.lei.lt in section "International projects" -> "EURATOM-LEI".

8 PUBLICATIONS

8.1. Kačegavičius T., Kaliatka T. Integral analysis of the W7-X fusion experiment with ASTEC and RELAP5 codes // 8th international conference of young scientists on energy issues CYSENI 2011, Kaunas, Lithuania, May 26-27, 2011. Kaunas: LEI, 2011. ISSN 1822-7554, p. 449-457.

8.2. Kaliatka A., Ušpuras E., Kaliatka T. Pressure surge in Wendelstein 7-X experimental stellarator facility // 14th international topical meeting on nuclear reactor thermalhydraulics (NURETH-14), Toronto, Ontario, Canada, September 25-30, 2011. Canada, 2011, p. 1-14.

8.3. Kaliatka A., Ušpuras E., Kaliatka T. Analysis of thermal hydraulic processes in Wendelstein 7-X experimental nuclear fusion facility // Proceedings of international congress on advances in nuclear power plants (ICAPP 2011), Nice, France, May 2-5, 2011. France, 2011, p. 1996-2004.

8.4. Kaliatka T., Ušpuras E. Application of best estimate methodology for Wendelstein 7-X experimental nuclear fusion device // 3rd international youth conference on energetics 2011 (IYCE,11), Leiria, Portugal, July 7-9, 2011. Portugal, 2011. ISBN 978-989-95055-6-8, p. 1-6.

8.5. Kaliatka T., Povilaitis M. Termohidraulinė analizė W7-X vamzdžio trūkio atveju // Šilumos energetika ir technologijos-2011: konferencijos pranešimų medžiaga, Kauno technologijos universitetas, 2011 vasario 3,4. Kaunas: Technologija, 2011. ISBN 978-609-02-0179-4, p. 89-94.

8.6. Gaigalas G., Rudzikas Z., Rynkun P., Alkauskas A. Dependence of the probabilities of the electric-multipole electron transitions in W24+on multipolarity, Phys. Rev. A, 83, 032509(13) (2011).

8.7. Bogdanovich P., Rancova O., Stikonas A. Quasirelativistic treatment of spectral characteristics of W^{37+}. Physica Scripta, 83, 065302(pp) (2011).

8.8. Kučas S., Karazija R. Closing of Coster-Kroning transitions and variation of fluorescence and Auger yields in isonuclear sequence of tungsten, Lith. J. Phys., 51, 198-204 (2011).

9 IMPLEMENTATION OF QA SYSTEM

The quality assurance system, according to standard LST EN ISO 9001:1995 requirements in Lithuanian Energy Institute, has been developed in 1999.

In 2001 the updating of quality assurance system of institute on the basis of requirements of standard LST EN ISO 9001:2001 was initiated. According to these requirements, the quality package of quality assurance documents in LEI was developed.

On February 17, 2004 the quality system of institute was certified by the Lithuanian Standards Board under the Ministry of Environment of the Republic of Lithuania and the certificate of quality management system conformity to standard LST EN ISO 9001:2001 was received. On February 15, 2007 duration of the certificate was extended for three following years.

On February 15, 2010 the quality system of institute was certified by the Lithuanian Standards Board under the Ministry of Environment of the Republic of Lithuania, and the certificate of quality management system conformity to standard LST EN ISO 9001:2008 was received.

On 15 February, 2010 the environmental management system of institute was certified by the Lithuanian Standards Board under the Ministry of Environment of the Republic of Lithuania, and the certificate of environmental management system conformity to standard LST EN ISO 14001:2005 was received.

The safety analysis of FUSION facilities is included in the procedure "PA/17-02, Control of nuclear installation safety research process", which is prepared in accordance with LST EN ISO 9001:2001 standards and operates together with other LEI quality management system procedures.

ISSN 2029-1612